# INFORMATION TO USERS

This manuscript has been reproduced from the microfilm master. UMI films the text directly from the original or copy submitted. Thus, some thesis and dissertation copies are in typewriter face, while others may be from any type of computer printer.

**The quality of this reproduction is dependent upon the quality of the copy submitted.** Broken or indistinct print, colored or poor quality illustrations and photographs, print bleedthrough, substandard margins, and improper alignment can adversely affect reproduction.

In the unlikely event that the author did not send UMI a complete manuscript and there are missing pages, these will be noted. Also, if unauthorized copyright material had to be removed, a note will indicate the deletion.

Oversize materials (e.g., maps, drawings, charts) are reproduced by sectioning the original, beginning at the upper left-hand corner and continuing from left to right in equal sections with small overlaps.

Photographs included in the original manuscript have been reproduced xerographically in this copy. Higher quality 6" x 9" black and white photographic prints are available for any photographs or illustrations appearing in this copy for an additional charge. Contact UMI directly to order.

ProQuest Information and Learning
300 North Zeeb Road, Ann Arbor, MI 48106-1346 USA
800-521-0600

# OPTICALLY PUMPED NMR IN THE QUANTUM HALL REGIMES

A Dissertation
Presented to the Faculty of the Graduate School
of
Yale University
in Candidacy for the Degree of
Doctor of Philosophy

by
Pankaj Khandelwal

Dissertation Director: Sean Barrett

May 2001

UMI Number: 3007371

UMI Microform 3007371



Bell & Howell Information and Learning Company
300 North Zeeb Road
P.O. Box 1346
Ann Arbor, MI 48106-1346

ABSTRACT

OPTICALLY PUMPED NMR IN
THE QUANTUM HALL REGIMES

Pankaj Khandelwal
Yale University
May 2001

We have built a new laboratory at Yale in order to study the spin polarization of electrons in the integer and fractional quantum Hall regimes using optically pumped nuclear magnetic resonance (OPNMR). This is the first demonstration of OPNMR below $T = 1.5$K. In order to extract quantitative values of the spin polarization from our measurements, we propose a model for the density distribution of electrons inside a quantum well. Using our data, we can deduce that the quasiparticles (excitations of the 2 dimensional electron gas) of the filling factor $\nu$=1/3 ground state have a tiny spin (on average, about one-tenth of an ordinary electron spin). Furthermore, we find that the assumption of homogeneous polarization along the plane of the quantum well due to fast quasiparticle motion is not always true. From comparisons of the data to our computer simulations, we can show that these quasiparticles slow down as the temperature is lowered. At $T < 0.5$K, we also find that the electron spin temperature can be driven out of equilibrium by applying a large amplitude radio frequency pulse. This procedure allows us to place a lower limit on the electron spin-lattice relaxation time in these materials at $\nu$=1/3.

Our recent measurements of the electron spin polarization at filling factors $\nu$=1/2 and $\nu$=1 are presented. These data also indicate the presence of interesting new physics. For example, our measurements at $\nu$=1/2 indicate that the ground state cannot be a "Fermi Sea" of non-interacting composite fermions. Our low temperature measurements at $\nu$=1 indicate that the skyrmion liquid freezes and gets pinned to the

lattice. We have also pursued the possibility of using OPNMR to study the structural properties of epitaxial GaN films. Our preliminary measurements of the NMR signal in these materials using conventional detection are presented.

To my Parents

...

# Acknowledgements

I would like to thank Professor Sean Barrett for his guidance and support throughout my graduate career. The strong sense of teamwork in our lab created by Sean was instrumental in obtaining much of the data shown in this thesis. Sean was also responsible for promoting the long and lively discussions that often took place in the lab regarding the physics behind the data. These repeated discussions with several kind and patient collegues often led to new considerations and enabled us to be thoroughly confident of our data and its interpretation. I would like to thank Subir Sachdev, Ramamurty Shankar and Nick Read for taking the time out to help our efforts to interpret our data.

The work described in this thesis was done in collaboration with Nicholas Kuzma and Anatoly Dementyev. I would like to thank Nick for taking the time out to teach me some of the things he knew so well (not among the least were electronics and machining). I also owe a great deal of thanks to Anatoly.

I would like to thank my wife Swati for her support during my graduate career and my teachers and friends with whom I have discussed physics on several occasions.

# Contents

**Acknowledgements** ii

**List of Tables** v

**List of Figures** vi

**1 Introduction** 1

1.0.1 The Integer Quantum Hall Effect . . . . . 2

1.0.2 The Fractional Quantum Hall Effect . . . . . 8

1.0.3 One Half Filling . . . . . 11

1.0.4 Spin, OPNMR and the Quantum Hall Effect . . . . . 11

**2 Optically Pumped NMR: Background and Previous Results** 17

2.0.5 Sample Description . . . . . 17

2.0.6 The Overhauser Effect . . . . . 21

2.0.7 The OPNMR Experiment . . . . . 22

2.0.8 Description of Intrinsic Line Shape . . . . . 27

2.0.9 Determining the Density . . . . . 32

2.0.10 More Experimental Details . . . . . 33

**3 $\nu$=1/3: Tiny Spin Flips and Ultraslow Motion!** 42

3.0.11 Temperature Dependence at 1/3 . . . . . 43
3.0.12 Wide Linewidth Spectra . . . . . 47
3.0.13 Ultraslow Motion . . . . . 50
3.0.14 Tiny Spin Flips . . . . . 54
3.0.15 RF Heating . . . . . 58
3.0.16 Electron Spin-Lattice Relaxation Time . . . . . 59

**4 $\nu$=1: Freezing out the skyrmion liquid** **65**
4.0.17 The Tilted Plateau . . . . . 65
4.0.18 Localization of Quasiparticles . . . . . 67
4.0.19 Two Different Scenarios . . . . . 71

**5 $\nu$=1/2: Landau Levels vs. Fermi Circles** **78**
5.0.20 Three Different Cases with Half Filling . . . . . 78
5.0.21 Partially and Fully Polarized Ground States . . . . . 82
5.0.22 WICFM . . . . . 82
5.0.23 If it doesn't fit, You must acquit . . . . . 87

**6 GaN: GaN't See the Satellites?** **92**
6.0.24 Introduction . . . . . 92
6.0.25 GaN Samples . . . . . 95
6.0.26 NMR of GaN Thin Films . . . . . 95
6.0.27 Nuclear Spin-Lattice Relaxation Time . . . . . 102

**7 Conclusions** **106**

**Bibliography** **108**

# List of Tables

2.1 Dimensions and other parameters of the GaAs samples . . . . . 21

2.2 NMR parameters for nuclei of interest in GaAs . . . . . 38

6.1 Dimensions and composition data for the GaN samples . . . . . 95

# List of Figures


1.1 The integer quantum Hall effect: $\rho_{xy}(B)$ and $\rho_{xx}(B)$ data . . . . . 3

1.2 The Hall bar and other possible quantum Hall geometries . . . . . 6

1.3 Effect of disorder on the one-body density of states. . . . . 8

1.4 The fractional quantum Hall effect: $\rho_{xy}(B)$ and $\rho_{xx}(B)$ data . . . . . 9

1.5 OPNMR measurements of electron spin polarization by Barrett et al. 13

1.6 Spin waves and skyrmions, schematic diagram . . . . . 15

2.1 Schematic diagram of a quantum well sample . . . . . 20

2.2 Demonstration of the Overhauser effect . . . . . 23

2.3 Schematic of the OPNMR timing sequence . . . . . 25

2.4 Examples of NMR spectra acquired **without** optical pumping . . . . 26

2.5 Examples of OPNMR spectra acquired **with** optical pumping . . . . 28

2.6 Comparison of the actual three dimensional density, $n_{3D}$, to $\frac{2n}{w}Cos^2((z'-w/2)/w)$ and $\frac{2n}{w_{eff}}Cos^2((z'-w/2)/w_{eff})$ . . . . . 30

2.7 A $^{71}$Ga emission spectrum along with the intrinsic line shape . . . . . 31

2.8 $K_S(\nu)$ near $\nu$=1 at $T$=1.5 K . . . . . 33

2.9 Schematic of a LCR circuit . . . . . 40

2.10 Resonant tank circuits used in the NMR probe . . . . . 41

3.1 Opnmr Spectra of sample 10W at $\nu$=1/3 . . . . . 44

3.2 Temperature dependence at $\nu$=1/3 . . . . . 46

3.3 Opnmr spectra at $\nu$=0.267 as a function of temperature . . . . . 48
3.4 OPNMR spectra of sample 10W at $T$=0.46 K, for 0.267$\leq\nu$<1/3 . . . 49
3.5 Linewidth and $K_S$ as functions of temperature for 0.267$\leq\nu$<1/3 . . . 51
3.6 Simulated OPNMR spectra for the breakdown of motional narrowing 53
3.7 Dependence of $K_S$ on filling factor at fixed temperature . . . . . 55
3.8 Dependence of $\mathcal{P}$ on filling factor at fixed temperature . . . . . 56
3.9 OPNMR spectra showing the effects of rf heating at $T = 0.45$ K . . . 60
3.10 The dependence of the effective spin temperature on the rf pulse length 61
3.11 Spectra which show the evolution of the line shape as a function of dark time . . . . . 62

4.1 $K_S$ and linewidth data near $\nu$=1 for three different temperatures . . . 66
4.2 The temperature dependence of the Knight shift and the linewidth for several filling factors near $\nu$=1 . . . . . 68
4.3 Expected radial dependence of the local electron spin magnetization density . . . . . 69
4.4 $K_S$ and the linewidth extracted from simulations performed near $\nu$=1 73
4.5 Knight shift and well width for $K3a$, $K3b$, $K3c$ and $K3*$ at $\nu$=0.95 . 74
4.6 Knight shift and well width for K3* at $\nu$=0.95 and $\nu$=0.97 . . . . . 76

5.1 OPNMR spectra near $\nu$=1/2 . . . . . 80
5.2 Temperature dependence of $K_S$ and $\mathcal{P}$ at $\nu=\frac{1}{2}$ . . . . . 83
5.3 Schematic of the NICFM model for $\nu$=1/2 . . . . . 84
5.4 Temperature dependence of the $^{71}$Ga spin-lattice relaxation rate $1/T_1$ at $\nu=\frac{1}{2}$ . . . . . 86
5.5 Values of $J$ and $m^*$ extracted by fitting the data at $\nu$=1/2 . . . . . 88
5.6 Comparison of $\nu$=1/2 data to a recent theoretical prediction . . . . . 90

5.7 Dispersion relations for Composite Fermions at $\nu$=1/2 with $T$=0.01K in $B_{tot}$=$B_{\perp}$=5.52T . . . . . 91

6.1 Schematic diagram of the GaN thin film samples . . . . . 96

6.2 NMR spectra of GaN thin films at room and cryogenic temperatures 98

6.3 The upper $^{69}$Ga satellite ( $m = -\frac{3}{2} \rightarrow -\frac{1}{2}$ ) transition . . . . . 99

6.4 Linewidth of the $^{69}$Ga central transition . . . . . 101

6.5 Frequency of the $^{71}$Ga and $^{69}$Ga central transition . . . . . 103

6.6 Nuclear spin-lattice relaxation time for $^{69}$Ga and $^{71}$Ga . . . . . 105

# Chapter 1

# Introduction

Discovered by Edwin Hall in 1879, then a graduate student at John Hopkins University in Baltimore, the (classical) Hall effect may be used to reveal the sign and density of the dominant charge carriers in a metalic or semiconducting system. Applying a magnetic field $B(||\vec{z})$ perpendicular to a sheet of gold leaf, he drove a current $I$ through the sheet $(I||\vec{x})$ and measured the transverse voltage $V_{Hall}$ that results $(V_{Hall}||\vec{y})$ (where $B \perp I \perp V_{Hall}$). Hall found found that this voltage was proportional to both the current and the magnetic field. The sign of the voltage determines the sign of the dominant charge carriers in the system. The effect can be understood using classical electrodynamics. The Lorentz force exerts a force on the electrons that pulls them sideways. This pull is proportional to the magnetic field and the current that passes through the leaf. The Hall resistance, $R_H$, defined as the ratio of the tranverse voltage to the longitudinal current can be worked out to be

$$R_H = B/ne, \tag{1.1}$$

where $n$ is the 2 dimensional density of the electrons passing through the leaf. This quantity is quite independent of sample characteristics, and so is a very useful

measure of the electron (majority carrier) density in various materials, i.e. metals, semimetals and semiconductors.

### 1.0.1 The Integer Quantum Hall Effect

The quantum version of the above effect, originally discovered by Klaus Von Klitzing[1] in 1980, occurs with electrons which are very tightly confined in one dimension, much more so than the thin leaf that was studied by Edwin Hall. Typical widths of 2 dimensional electron gases (2DEG) are about 100-300Å. These widths are so tiny that the energy of the next excited state for the electron confined in the $z$ direction can be much larger than the temperature scale. In such a system, when the magnetic field is changed, we no longer observe the linear dependence of the Hall resistance on the magnetic field, but plateaus (Fig. 1.1a) which are very accurately quantized (to better than $10^{-8}$) at:

$$R_H\left(i^{\text{th}}\text{ plateau}\right) = \frac{1}{i}\frac{h}{e^2}\,, \tag{1.2}$$

where $i$ is an integer.

We can characterize the 2DEG by its two-dimensional conductivity and resistivity tensors $\sigma$ and $\rho = \sigma^{-1}$, which are expressed in terms of the sheet current density $\mathbf{j}$ and electric field $\mathbf{E}$ as:

$$\mathbf{j} = \begin{pmatrix} \sigma_{xx} & \sigma_{xy} \\ \sigma_{yx} & \sigma_{yy} \end{pmatrix} \mathbf{E}\,, \qquad \text{and} \qquad \mathbf{E} = \begin{pmatrix} \rho_{xx} & \rho_{xy} \\ \rho_{yx} & \rho_{yy} \end{pmatrix} \mathbf{j}\,, \tag{1.3}$$

such that Equation 1.1 becomes:

$$\rho_{xy}(B) = \frac{1}{e\,n}B, \;\; (\text{In 2D},\; \rho_{xy} = R_H). \tag{1.4}$$

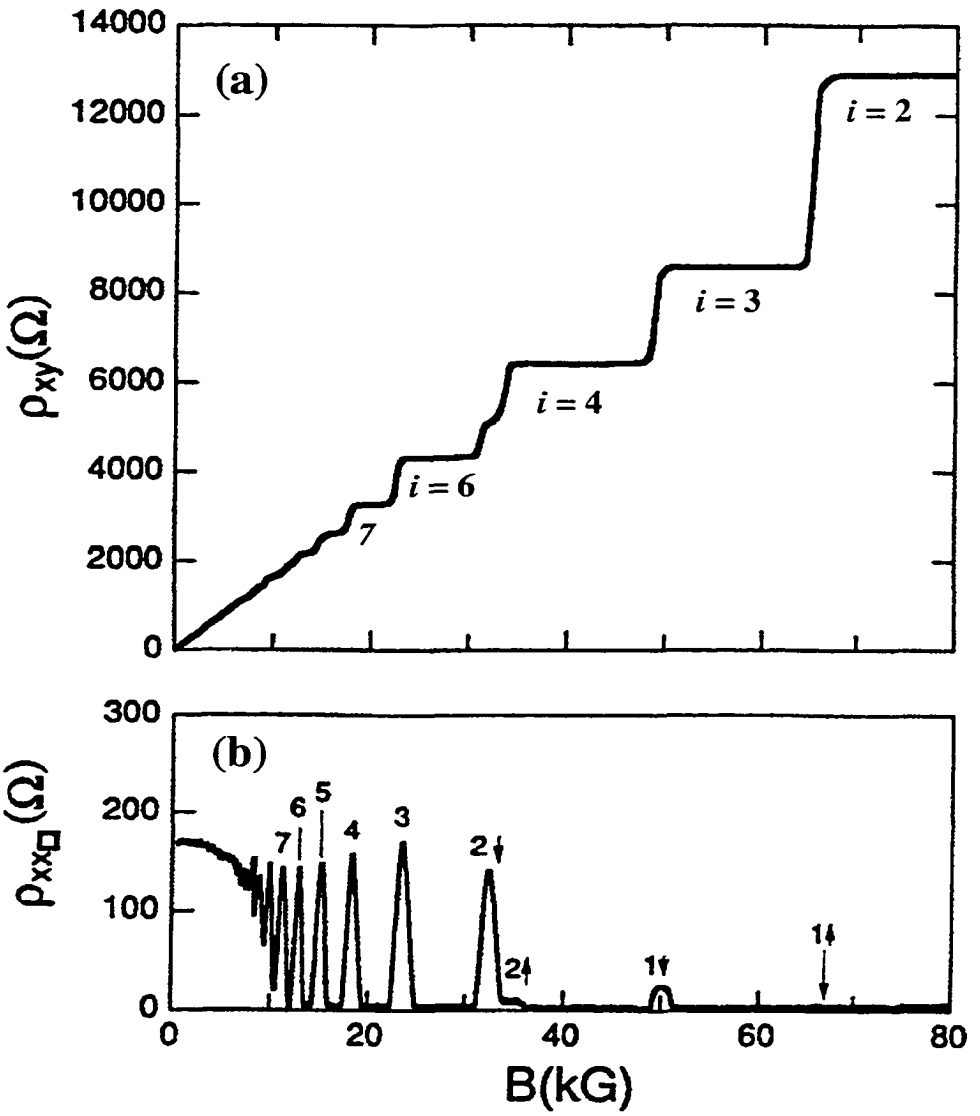


Figure 1.1: (a) – Field dependence of the Hall resistivity $\rho_{xy}$, exhibiting plateaus at $h/e^2 = 25.812805\,\mathrm{k}\Omega$ divided by an integer $i$. Plateaus for $i = 2$, 3, 4, 6, and 7 can be clearly seen. (b) – The corresponding $\rho_{xx}$ trace. Adapted from [2].

The *integer* quantum Hall effect (IQHE) can then also be expressed as step-like deviations in $\rho_{xy}$ from this linear law. Simultaneously, the diagonal components of resistivity vanish ($\rho_{xx} = \rho_{yy} = 0$) near the center of each plateau in $\rho_{xy}$, as Figure 1.1(b) demonstrates. At the center of each plateau, $\rho_{xy} = h/ine^2$.

In what follows, we will attempt to understand the IQHE with a few simple arguments, leaving the details for much more comprehensive reviews of the quantum Hall effect[3, 4, 5, 6, 7]. Lets first consider the problem of an electron with a spin in a magnetic field B$||\vec{z}$:

$$\mathcal{H} = \frac{1}{2m^*}\left(\hat{\mathbf{p}} - \frac{e}{c}\mathbf{A}\right)^2 - \mathrm{g}^*\mu_B\,\mathbf{S}\cdot\mathbf{B}\,. \tag{1.5}$$

The magnetic vector potential $\mathbf{A}$ can be chosen using the Landau gauge ($A_y = Bx$, $A_x = A_z = 0$), which leads to the solution:

$$\psi(x,y) = \exp\left(\frac{i}{\hbar}p_y\,y\right)\chi(x)\,\phi_{\mathrm{spin}}\,, \tag{1.6}$$

where $\chi(x)$ satisfies the linear oscillator equation:

$$\chi''(x) + \frac{2m^*}{\hbar^2}\left[(E + \mathrm{g}^*\mu_B s B) - \frac{m^*}{2}\omega_c^2(x - x_0)^2\right]\chi(x) = 0 \tag{1.7}$$

with

$$\omega_c = \frac{eB}{m^*c} \quad \text{and} \quad x_0 = -\frac{c\,p_y}{eB}\,. \tag{1.8}$$

Thus, the solutions $\psi(x,y)$ to Equation 1.5 are localized in $x$, but extended (as plane waves) along $y$, with the energy levels given by:

$$E_n = \hbar\omega_c\left(n + \frac{1}{2}\right) \pm \frac{1}{2}\mathrm{g}^*\mu_B B\,. \tag{1.9}$$

In GaAs the term $\hbar\omega_c$ is much larger than $E_Z = \mathrm{g}^*\mu_B B$, so that the Landau levels (Fig. 1.3) are actually arranged in pairs ($E_{2n+1} - E_{2n} = E_Z$) which are widely separated from each other. These Landau levels, in the absence of disorder and in an infinite geometry, are highly degenerate since $p_y$ can assume any values in the continuum.

However, if the geometry is finite, the momentum $p_y$ can only take on a finite number of values. First, because of periodic boundary conditions, $p_y = 2\pi N_y/L_y$, and second, because $x_0$ $(= -cp_y/eB)$ can only take values from 0 to $L_x$. Hence, the number of states per level, $N_y$, can be counted to be $L_xL_yeB/hc$. The Landau level filling factor is defined as the fraction of these degenerate Landau levels occupied by the electrons:

$$\nu = \frac{nhc}{eB} . \tag{1.10}$$

where $n$ is the two-dimensional electron density and $n_\Phi = N_y/L_xL_y = eB/hc$ turns out to be just equal to the density of magnetic flux quanta penetrating the sample plane. However, unlike in superconductors, here the magnetic field penetrates the 2DEG sample homogeneously.

The IQHE is remarkably independent of the particulars of the sample, which can contain many defects. This surprising insensitivity to the nature of the sample pointed to a "fundamental" origin for the IQHE. However, in the explanation of the quantum Hall effect proposed by Laughlin, the defects found in real samples play a crucial role. The existence of the $\rho_{xy}$ plateau reveals the subtle role played by "localized" and "extended" states. In order for us to observe the plateau, we need to have localized states present at the Fermi energy that can trap the electrons that get pushed out of the lower Landau levels as we change the magnetic field. Disorder tends to broaden the electronic spectrum, until the Landau levels are no longer separated, and causes the states in the tails of the Landau level to become localized (Fig. 1.3). If it weren't for these localized states, the quantum Hall effect would occur over a very small region, and the plateaus would not be visible. The trapped electrons no longer contribute to the current, hence we also require that all the other electrons speed up, in order to make up for the lost current of these localized electrons.

Laughlin proposed an elegant explanation containing all the above ingredients. To

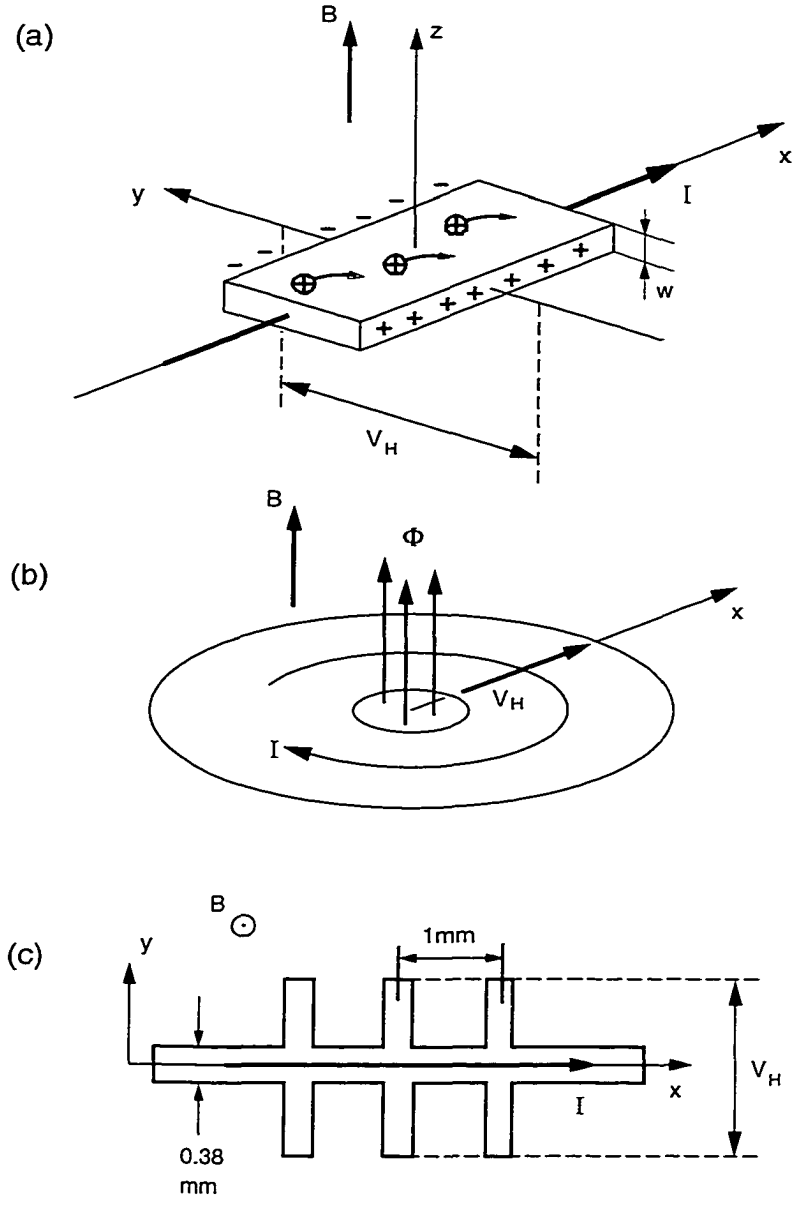


Figure 1.2: Sample geometries used in the quantum Hall effect: (a) the classic "Hall bar", (b) a theorist's concept of the "Corbino disk", where the Hall voltage is applied azimuthally via $V_H = \frac{d}{dt}\Phi$ (as in Laughlin's *Gedankenexperiment*), and (c) the top view of a typical sample used in magneto-transport measurements.

understand his explanation, let us consider the "Corbino" geometry, shown in Figure 1.2(b). He proposed the following form for the Faraday law of induction to be used with the 2DEG,

$$I = c\Delta E/\phi, \tag{1.11}$$

i.e., the total current at a given value of $\phi$ is the adiabatic derivative of the total energy with respect to $\phi$, where $\phi$ is the flux that passes through the annulus, $I$ is the current and $V_H$ is the Hall voltage (Fig.1.2). We can choose electronic states (Eq. 1.6) such that they are localized in the radial dimension and extended around the annulus azimuthally. Extended states that enclose the varying magnetic flux will gain a phase factor around the loop as the magnetic flux through the annulus is varied, and thus their azimuthal momentum will change, resulting in the displacement of the wave function radially (since the radial coordinate and the azimuthal momentum correlate as $x_0$ and $p_y$ in Eq. 1.8). Since they gain a phase factor of $2\pi$ when a unit of flux quantum is pushed through the annulus, the wavefunctions must be unchanged after each unit of flux that is added through the annulus. In each Landau level, the wave functions will shift into each other's steps radially, transferring a unit of charge per Landau level, per flux quantum added, from one edge of the sample to the other. If the voltage across the radial dimension is $V_H$, the energy gained by the electrons is $eV_H$, hence the current is $I = ne^2/hV_H$, giving us the right Hall conductance. This argument holds in the presence of disorder[9], which tends to localize states present at the tails of the Landau level. It is important that the argument remains valid in the presence of disorder, since it is the disorder that is responsible for generating the plateaus seen in the IQHE.

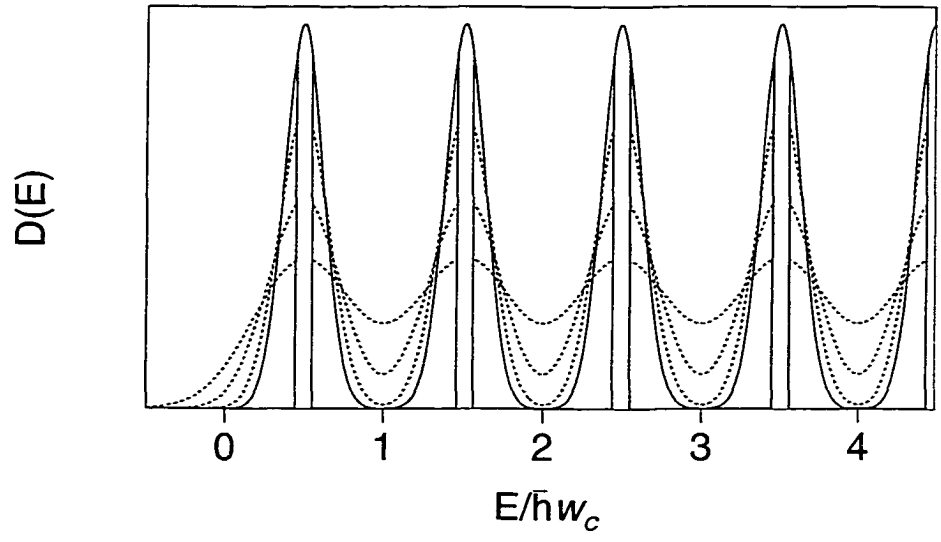


Figure 1.3: Effect of disorder on the one-body density of states. Only the states near the center of each Landau level (shaded region) are delocalized. Adapted from Laughlin[6].

### 1.0.2 The Fractional Quantum Hall Effect

Figure 1.4 illustrates the *fractional* quantum Hall effect (FQHE), where by going to stronger magnetic fields and using samples with higher mobilities it is possible to observe plateaus similar to those in the integer effect, but occurring at the values of:

$$\rho_{xy}\ (\text{plateau}) = \nu^{-1}\,\frac{h}{e^2}\ , \tag{1.12}$$

where $\nu = \frac{m}{n}$ is a simple fraction rather than an integer. The strongest effect takes place at $\nu = \frac{1}{3}$, with distinct plateaus in $\rho_{xy}$ and minima in $\rho_{xx}$ also observable at many other fractions, e.g. $\nu = \frac{1}{5},\ \frac{2}{3},\ \frac{2}{5},\ \frac{3}{5},\ \frac{2}{7}$, and so on.

Although similar in appearance to the IQHE, the FQHE **cannot** be explained without considering electron-electron interactions. Indeed, the independent electron

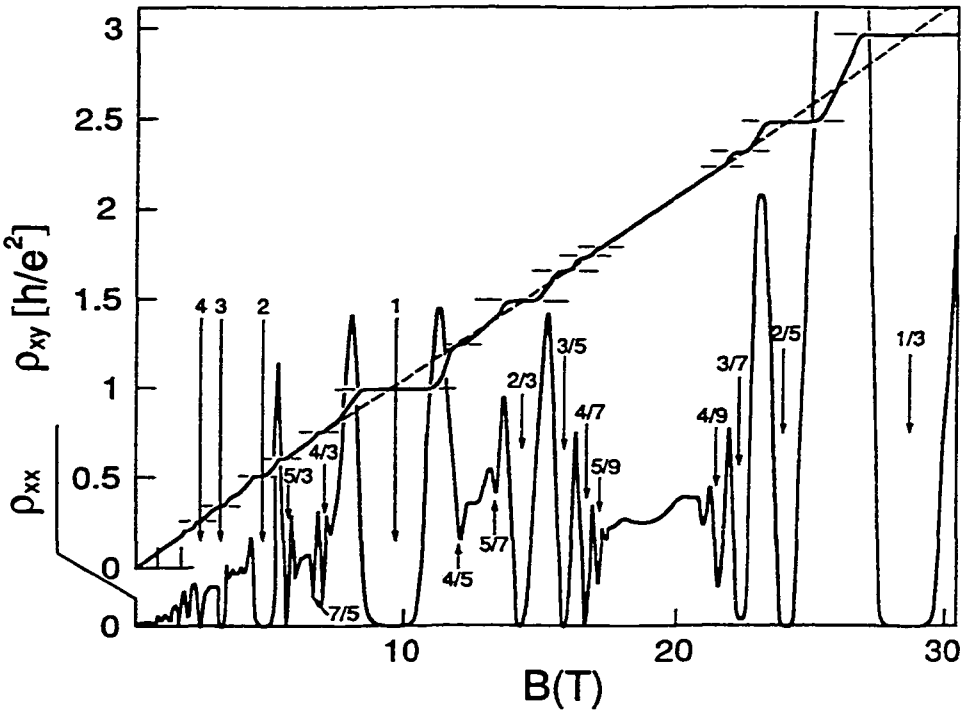


Figure 1.4: Overview of the observed fractions in the FQHE measurements. The dashed diagonal line represents the classical Hall resistivity (Eq. 1.4) and the solid curve with step-like structure (plateaus) — the experimental results. Diagonal resistivity $\rho_{xx}(B)$ is drawn on a separate scale, with regions of $\rho_{xx}=0$ (corresponding to the plateaus in $\rho_{xy}(B)$) and sharp spikes between some of them. The filling factors corresponding to each fraction are marked with arrows. Adapted from [8].

picture discussed above does not predict that any energy gaps should be found at the fractional filling of $\nu = \frac{1}{3}$ as opposed to, for example, $\nu = \frac{1}{2}$.

By assuming that the electron spins are fully polarized by the strong magnetic fields at low temperatures, and keeping in mind the need to minimize Coulomb repulsion between electrons, Laughlin proposed the following form for the many-body electron wave function for a $\nu = \frac{1}{m}$ ground state [9]:

$$\psi_m(z_1, \ldots, z_N) = \exp\left[-\frac{1}{4l_o^2}\sum_l^N |z_l|^2\right] \prod_{j<k}^N (z_j - z_k)^m \ , \tag{1.13}$$

where the complex variables $z_j = x + iy$ are functions of the $j^{\text{th}}$ electron coordinates, $l_o = (\hbar c / eB)^{1/2}$ is the magnetic length and $m$ is an odd integer.

The "zeroes" of this wavefunction minimize the Coulomb electron-electron interaction energy, which may be seen by the following. If we fix the position of the first N-1 electrons, then the probability of finding the $N^{th}$ electron goes to zero as its position approaches any of the other fixed electrons (because of the $(z_N\text{-}z_k)^m$ factor in eqn. 1.13). These $m$ zeroes are also called "vortices", since moving an electron in a closed loop around any one of them leads to an additional phase shift of $2\pi$ in the wavefunction. Placing $m$ vortices on each electron leads to the filling factor $\nu = n/n_\Phi = 1/\text{m}$. The form of the wavefunction in eqn. 1.13 suggests that an energy gap will exist at $\nu = 1/m$: adding or removing magnetic flux will create either free vortices or electrons having fewer than $m$ flux quanta associated with them, at an extra energy cost.

Laughlin's "Corbino disk" argument can also be directly applied to his wave function $\psi_m$ (Eq. 1.13), with a remarkable result: excitations associated with the free flux quanta or with the electrons lacking a vortex can be described as fractionally charged (e.g. $q = \frac{1}{3}e$) quasiparticles and quasiholes [5, 10]. Indeed, such objects have been recently observed in the magnetic focusing [11], resonant tunneling[12] and shot-noise

[13] experiments.

### 1.0.3 One Half Filling

Significant progress in describing a strongly interacting 2-dimensional electron gas in a large magnetic field in terms of composite fermions (CF) in a reduced field has stimulated a large body of theoretical and experimental work [5, 10]. One of the most suprising implementations of this idea was put forth in the seminal work of Halperin, Lee, and Read [14], who argued that the ground state of the 2DEG at Landau level filling factor $\nu=\frac{1}{2}$ is well-described by CF in zero net magnetic field, which therefore exhibit a well-defined Fermi surface. Experiments carried out near $\nu=\frac{1}{2}$ have provided convincing evidence of the existence of the CF Fermi surface [15, 16, 17, 11, 18]. We will describe our measurements on the $\nu=1/3$ and $\nu=1/2$ states in chapters 3 and 5 respectively.

### 1.0.4 Spin, OPNMR and the Quantum Hall Effect

Soon after the discovery of the QHE's, Halperin[19] pointed out that it was not proper to neglect the presence of the electronic spin when one considers the size of the effective Landé $g$ factor in GaAs. The coulomb interaction between the electrons takes the form $V(\mathbf{r}-\mathbf{r}') = e^2/(\,\epsilon\,|\mathbf{r}-\mathbf{r}'|\,)$. For GaAs quantum wells, the dielectric constant is $\epsilon \approx 13$, and the effective electron mass and the effective g-factor are $m^* = 0.07\,m_e$, and $g^* = -0.44$, where $m_e$ is the bare electron mass in vacuum. The energy needed to generate a quasihole (quasielectron) is estimated to be [20, 21] about $0.026\ e^2/l_o$ and $0.073\ e^2/l_o$. Using the expression for the magnetic length used before, $l_o = (\,\hbar c\,/\,eB\,)^{1/2}$ and using the numbers above, we find that even in a 10 T field, the Zeeman energy to

flip a spin ($\sim$ 3 K) is smaller than the energy to excite a quasiparticle ($\sim$ 60 K). Hence, it might be possible that some of the originally detected FQHE states were not fully spin polarized, but partially or completely unpolarized[5]. Some of the early transport experiments gave hints about the nature of the spin configuration of the quantum Hall states. QHE states which are fully polarized tend to get stronger, i.e. develop a deeper $\rho_{xx}$ minimum as one increases the Zeeman energy. However, this was not the case with certain filling factors, such as $\nu$=8/3 that actually became worse upto a certain Zeeman energy and then started to strengthen again. This was interpreted as evidence for a transition from a state that was partially polarized to one that was fully polarized (one way to increase the Zeeman energy without changing $\nu$ is to tilt the sample and increase the magnetic field till $B_\perp$ is the same, since the electronic spin couples to the total magnetic field and $\nu$ only depends on $B_\perp$ in a 2D sample). However, none of the above experiments can measure the spin of the electrons directly, which is the motivation for this thesis. Information about the electronic spin will prove to be very useful as we will show that it is very hard to explain all the features of our experiments using the conventional QHE theory.

The reason why most of the early QHE experiments were transport measurements was because the low density of electrons buried deep inside the sample typically make negligible contributions to "classic" thermodynamic measurements. As a result, very little is known about certain features of the 2DEG, the spin in particular. In order to perform regular NMR on the 2DEG, one would like to have $\sim 10^{19}$ nuclear spins present in the sample. This is about 20-40 times more spins than are present in the quantum well. The original NMR experiments in the quantum Hall regime relied on a technique originally predicted by Overhauser (to be described in the next chapter) to increase the thermal polarization of the nuclei. Shown in Fig. 1.5 are Knight shift data[22] plotted as function of filling factor near $\nu$=1. The Knight shift (which will be

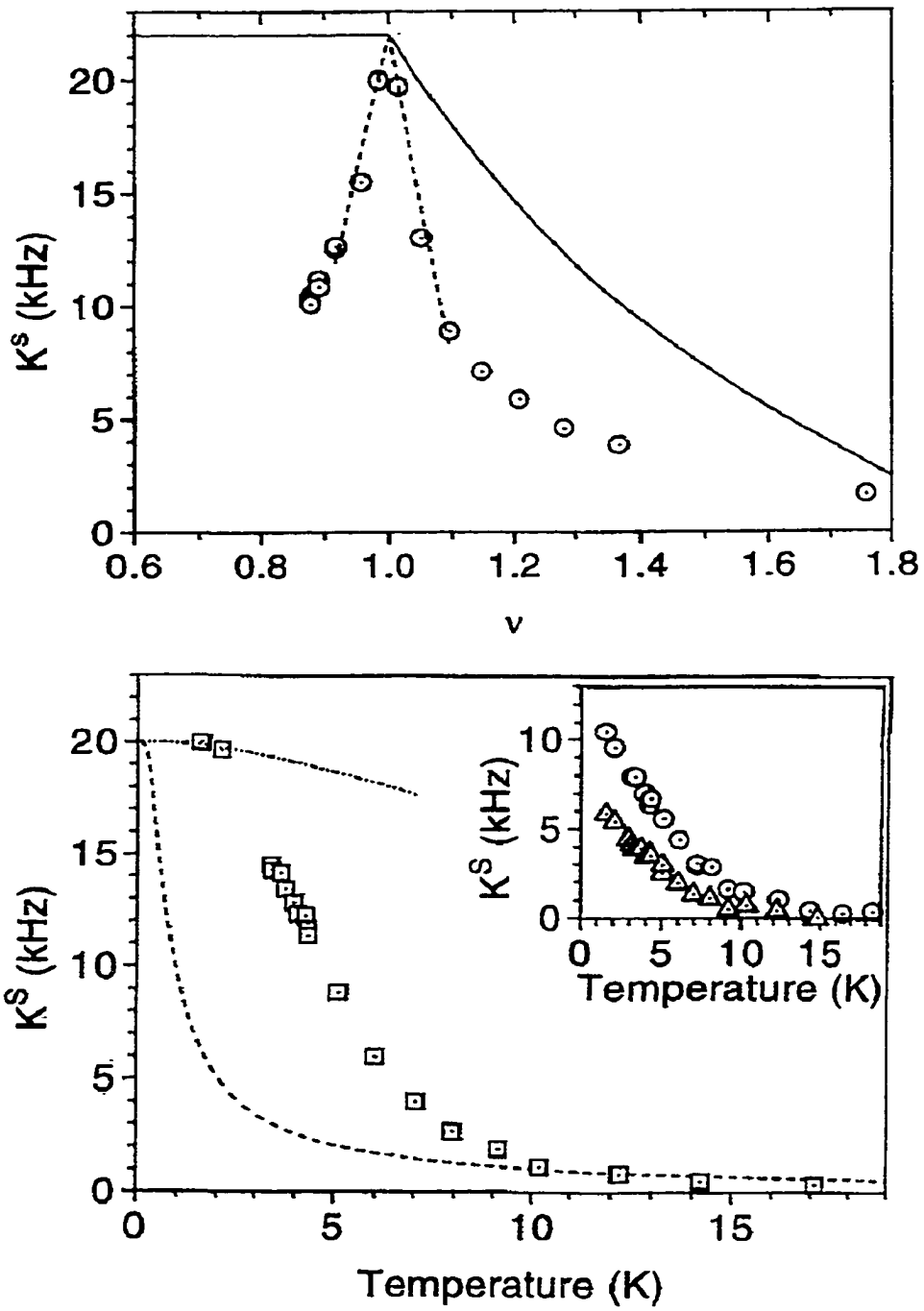


Figure 1.5: Top panel: Spin polarization plotted vs. filling factor $\nu$ and compared with both a single particle and Skyrmion-based model. The single-particle polarization is based on a simple counting argument, one spin flip per unpaired flux quantum for $\nu < 1$, and $S_z = 1$, for $\nu > 1$. Bottom panel: Electron spin polarization as a function of temperature at a filling factor close to $\nu = 1$. Reprinted from Barrett et al. [22].

explained later) is a measure of the electron spin polarization. Something very unexpected happens in Fig.1.5. For independent electrons, we expect the Knight shift to remain constant (fully polarized) for filling factors below 1, and drop at a certain rate (solid line) for filling factors above 1. This is not what happens in a real QHE system. The Knight shift falls drastically on either side of $\nu$=1, revealing the importance of electron-electron interactions even at $\nu$=1. Early transport measurements[23] also noted anomalies in the activation gap energy at $\nu$=1, 2, and 3. These anomalies indicated the presence of a "exchange enhancement" of the Zeeman energy. We will describe some of our recent measurements at $\nu$=1 in chapter 4 that shed more light on this and other aspects of the $\nu$=1 QHE state.

At about the very same time as the original Knight shift measurements were being performed, S. L. Sondhi and H. A. Fertig independently developed a picture of the quantum Hall effect at $\nu$=1, that would explain just these very features. In a theory developed by S. L. Sondhi *et al.* [24] and applied to $\nu = 1$ by H. A. Fertig *et al.* [25], skyrmions are charged spin textures, described in terms of a smoothly varying unit vector field, with an effective number of spin reversals $K$ and "size" that are determined by the competition between the Coulomb energy (which increases both) and the Zeeman energy (which reduces both). Qualitatively, the skyrmion spin texture is cylindrically symmetric with a down spin at $r$=0, and a smooth radial transition to up spins at $r$=$\infty$. In between, the non-zero XY spin components have a vortex-like configuration[24, 26, 27, 28]. The addition of skyrmions to the $\nu$=1 ground state was predicted to result in a rapid depolarization of the lowest Landau level, as $|\delta\nu|$ is increased[25, 29]. Several experiments are consistent with this[22, 30, 31] and other predictions[32, 33, 34, 35, 36] of the skyrmion model.

Shown schematically in Fig. 1.6 are two types of excitations, neutral (caused, say by increasing the temperature, e.g., spin waves) and charged (by varying the filling

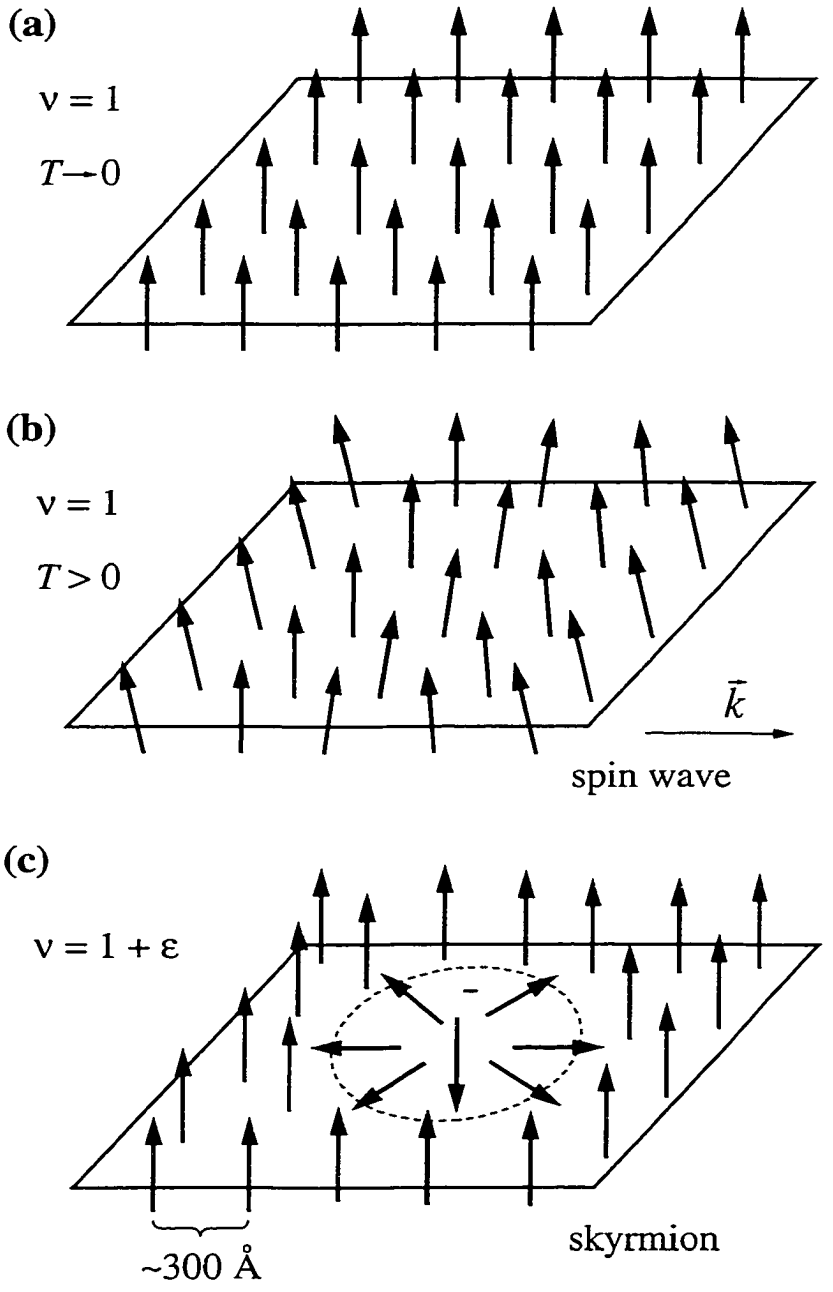


Figure 1.6: Schematic representations of a fully spin-polarized ground state (a), along with its neutral and charged excitations: (b) spin wave, and (c) spin texture called "skyrmion".

factor, e.g., skyrmions). The neutral excitations of a quantum Hall ferromagnet were considered by Y. A. Bychkov *et al.* [37] and C. Kallin and B. I. Halperin [38], who computed the dispersion relation for spin waves. As Figure 1.6 shows, both the spin waves and the skyrmions cause a reduction in the total spin of the 2DEG.

# Chapter 2

# Optically Pumped NMR: Background and Previous Results

There are several experimental conditions that one needs to satisfy in order to perform optically pumped NMR measurements on GaAs quantum wells. This chapter will deal with these experimental concerns. A description of the multiple quantum well samples that were used to study the Hall effect is provided in section 2.0.5. In order to detect the small NMR signal from these samples, we used optical pumping to enhance the nuclear spin polarization in the multiple quantum wells. This procedure and the Overhauser effect (dynamical nuclear polarization) are explained in detail in sections 2.0.7 and 2.0.6. The expected NMR spectrum from nuclei inside the quantum wells is discussed (section 2.0.8) along with the procedure that we used to determine the electron density in these samples (section 2.0.9). Finally, some additional experimental details are given in section 2.0.10.

### 2.0.5 Sample Description

The quantum Hall effect was originally discovered in a Metal Oxide Silicon Field Effect Transistor (MOSFET)[1]. In a FET, the electrons reside at the intersection of a crystalline semiconductor and a random glass. This surface is very rough and acts as a strong scattering potential for the electrons. It is desirable to reduce this strong scattering potential in order to study effects which are unrelated to the impurity scattering. We can increase the mobility of the electrons (or decrease the impurity scattering potential) by a factor of a 1000 over those in a silicon FET by using a quantum well (or a single interface) of GaAs/AlGaAs grown by molecular beam epitaxy (MBE). MBE is a high-vacuum evaporation technique that one can use to grow high-quality, atomically precise thin layers of semiconductor. In these high mobility heterostructures, the dopant atoms which are the strongest impurity scatterers are physically separated from the electrons in these structures, in a method now commonly refered to as as modulation doping. This approach was first used by Tsui et al. [39] in their search for exotic phenomena at high magnetic fields, which led to the discovery of the fractional quantum Hall effect. The distance that the silicon dopant atoms are placed away from the quantum well determines the 2D electron density in the quantum well. AlAs and GaAs have very similar lattice spacings. It is for this reason that quantum wells made out of a combination of these two have very smooth interfaces and correspondingly high mobilities. Recent optical measurements on high quality samples have determined that the interface is on average atomically sharp with well separated steps (about 1 every 500nm) where the layer could fluctuate by an atom.

All of the multiple quantum well samples in this study were grown by molecular beam epitaxy (MBE) on semi-insulating GaAs(001) substrates by Loren N. Pfeiffer and Kenneth W. West. Figure 2.1 shows a slice of the sample along the $x' - z'$ plane. Here, $z'$ is the growth direction and $x', y'$ lie in the plane of the quantum well. Sample

parameters for the three samples used for the work in this thesis are shown in Table 2.1. For example, sample 40W contains forty 300 Å wide GaAs wells separated by 3600 Å wide $Al_{0.1}Ga_{0.9}As$ barriers. The GaAs substrate is 0.5 mm thick for all three samples. Silicon delta-doping spikes located in the center of each barrier provide the electrons that are confined in each GaAs well at low temperatures, producing 2DES with very high mobility ($\mu > 1.4 \times 10^6$ cm$^2$/Vs). This MQW structure also results in a 2D electron density that is extremely uniform from well to well and is unusually insensitive to light[40]. The two usual mechanisms for changing the carrier density with ambient light are supressed in these samples because of the low Al concentration in the barriers (which tends to supress the ionization of $DX^0$ and $DX^-$ centers) and the symmetric pinning of the conduction band edge near the position of the ionized $Si^+$ dopants (which tends to confine the optically created electron hole pairs in the quantum well till they recombine). Having a carrier density that is insensitive to light is very important for our experiments since we use optical pumping to enhance the polarization of the nuclei inside the quantum well. The amount of Al in the $Al_{0.1}Ga_{0.9}As$ barrier controls the height of the barrier potential and is usually kept between 0.03 and 0.30. A low Al concentration also results in higher mobility of the electrons in the quantum wells. The value of the electron $g$ factor inside our quantum wells is close to its value in the bulk (-0.44). The $g$ factor in AlGaAs depends on the Al concentration, so it is possible to make a quantum well with $g$=0, although the electrons inside such a quantum well have a very poor mobility. Finally, it is also possible to change the electron $g$ factor inside a quantum well by changing the ambient pressure[41].

Also shown in Fig. 2.1 is the minimum of the conduction and the maximum of the valence band as a function of $z'$ for the electrons. The height of the barrier potential is determined by the conduction band offset. At room temperature, the electrons have

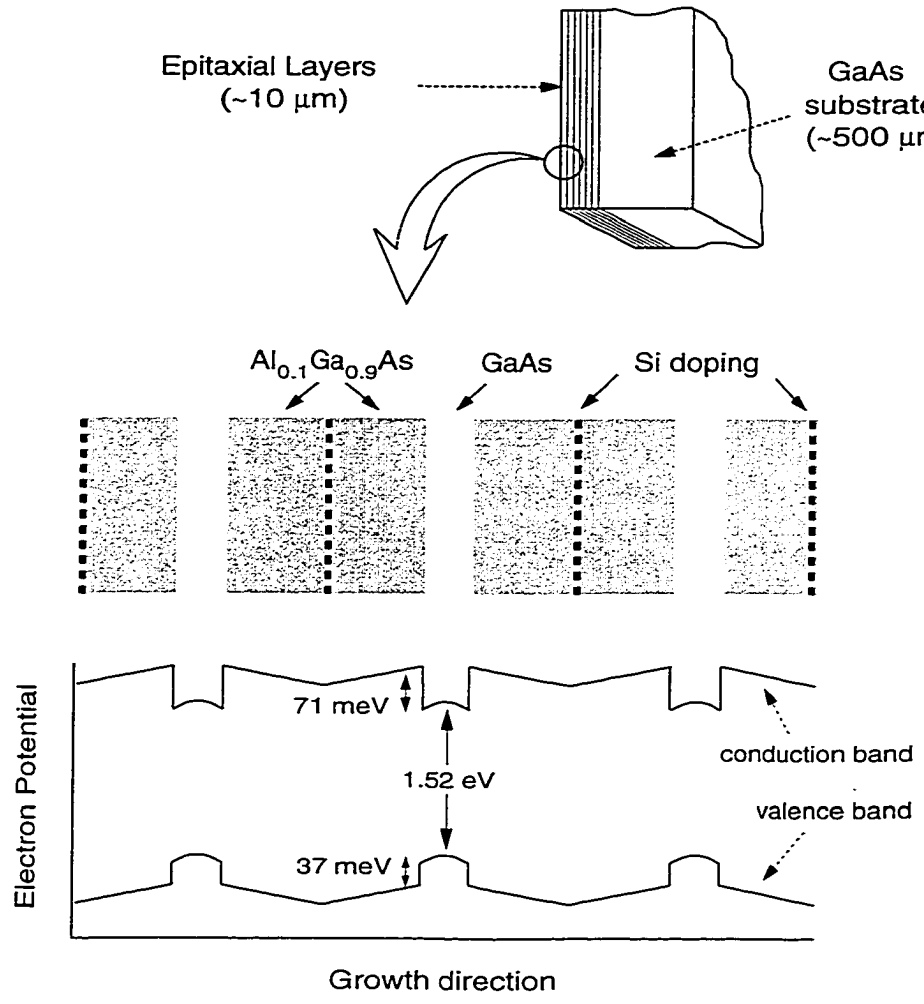


Figure 2.1: Schematic diagram of a quantum well sample, with the epitaxial layer structure and the corresponding electron energy bands shown as a function of the spatial coordinate $z'$ along the growth direction.

enough thermal energy to move freely thoughout the sample. At low temperatures, their small thermal energies do not allow them to tunnel outside the quantum wells. The electrons thus trapped in the quantum well form the two dimensional electron system (2DES).

Table 2.1: Dimensions and other parameters of the GaAs samples. The numerical value for the well and barrier width of Sample 10W was scaled down from their nominal as-grown value by 13.3% in order to make the Knight shift and the electron density self-consistent. Sample 10W was grown without wafer rotation, which could have led to a uniform gradient in the Ga flux, and thus the width of all the layers across a 2-inch substrate [42].

| | Sample 40W | Sample 10W | Sample P95 |
|---|---|---|---|
| Grower's ID | 3–5–93.4 | 10–10–91.1 | Sample P95 |
| $n$ ($\times 10^{10}$cm$^{-2}$) | 6.69 | 7.75 | 15.2 |
| Maximum $K_S$ | 9.0 Khz | 11.8 Khz | 22.0 Khz |
| Field at $\nu$=1 | 2.76 T | 3.2 T | 6.27 T |
| 2D Area (cm$^2$) | 6 × 5 | 6 × 4 | 6 × 5 |
| Well width (Å) | 300 | 260 | 300 |
| Barrier width (Å) | 3600 | 3120 | 1800 |

### 2.0.6 The Overhauser Effect

A.W. Overhauser [43, 44] first realized that it was possible to enhance the nuclear spin polarization of a coupled electron-nuclear system by saturating the electron spin resonance. This enhancement is roughly equal to the ratio of the mass of the electron and the nucleus, or about a 1000 under perfect conditions. His proposal was treated with skepticism at first, until the effect was measured experimentally by T. R. Carver and C. P. Slichter [45] in Li metal. We can try to understand the concept behind the Overhauser effect using the following example. Shown in Fig. 2.2 are the four energy levels of a coupled electron nuclear spin system. For example, the conduction electrons in GaAs quantum wells are coupled to the nuclei via the Fermi contact hyperfine interaction, ($\mathcal{H}$=$A\vec{I}.\vec{S}$). Optical pumping (e.g., illumination with circularly polarized light just above the band-gap energy will drive the system from equilibrium. In GaAs quantum wells, the matrix elements are such that optical pumping with $\sigma$+ light should lead to an excess of electrons in the $m_z$=-1/2 level, resulting in a non-equilibrium spin polarization for the 2D electron system, as long as the electron spin-

lattice relaxation time is comparable to or greater than the lifetime of the optically excited electronic state. The nuclear-electron hyperfine coupling acts to bring the states 2 and 3 in thermal equilibrium, leading to a large difference in the population of the states 1 and 2, and states 3 and 4, resulting in a large nuclear spin polarization. This optical pumping effect was first discovered in semiconductors by G. Lampel, in 1968. Lampel was able to increase the nuclear polarization of $^{29}$Si in bulk silicon by a factor of 100[46]. His seminal work led to the development of optically detected NMR techniques in GaAs[47]. More information about optical pumping in semiconductors and noble gases can be found in a recent review paper[48]. The optically pumped NMR (OPNMR) experiments carried out in this thesis are direct descendants of Lampel's discovery.

### 2.0.7 The OPNMR Experiment

In our experiments described below, data were acquired using the following OP-NMR timing sequence: SAT–$\tau_L$–$\tau_D$–DET, modified for use below 1 Kelvin (e.g., $\tau_D \sim 40$ s, laser power $\sim 10$ mW/cm$^2$, low rf voltage levels).

Light from a Ti:Sapphire laser (which was pumped by an argon ion laser) was used to pump the electrons from the valence to the conduction band. The wavelength of the light ($\sim$812 nm) is chosen to be just above the bandgap in GaAs[22, 49]. There are a few sharp peaks in the strength of the NMR signal as we tune the light above the bandgap. Typically, we set the frequency to the first of these peaks, which is usually also the highest. The cooling power of the $^3$He cryostat limits us to about a half hour at 400mK with $\sim$10mW of laser power incident on the sample. After this half hour, all the liquid has been vaporized, and we have to start over by warming up the charcoal sorb and re-condensing a 1.5K puddle of liquid $^3$He, a process that

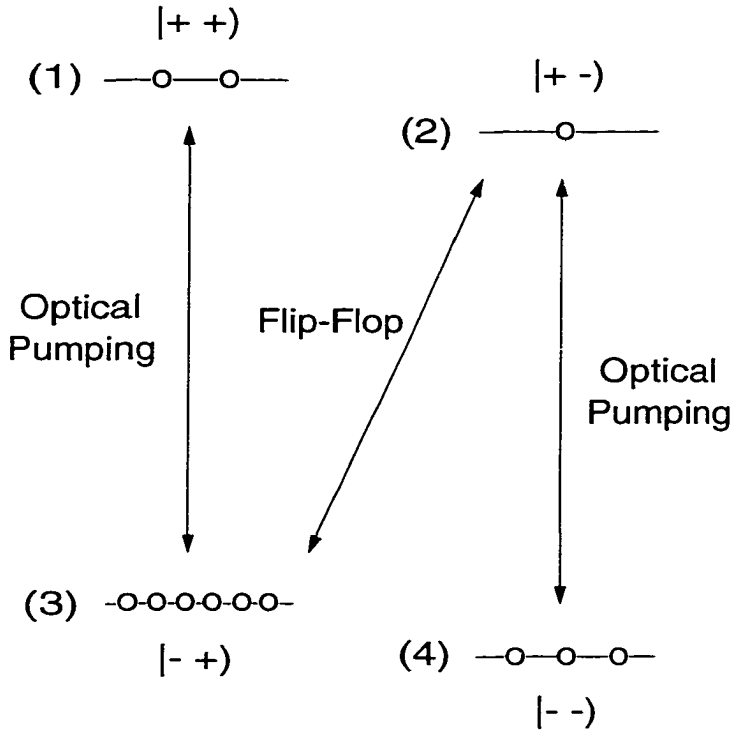


Figure 2.2: Shown are the four levels of a coupled electron- nuclear system. The polarization of the electron system ($n_3$-$n_1$, $n_4$-$n_2$) is usually driven out of equilibrium. The nuclear-electron hyperfine coupling then acts to bring the states 2 and 3 in thermal equilibrium, leading to a large difference in the population of the states 1 and 2, and states 3 and 4, resulting in a large nuclear spin polarization.

usually takes about another half hour. Because of this limitation, we typically use light powers of ~15mW or less.

Shown in Fig. 2.3, the sequence used to perform the NMR experiment consisted of the following four parts: **SAT**–$\tau_L$–$\tau_D$–**DET**.

**SAT** — Radiate the sample with quick bursts of RF power to destroy any residual nuclear magnetization. We test this part by detecting the nuclear magnetic resonance

with a very short delay after the saturation pulse and verifying that there is no residual thermal nuclear polarization.

$\tau_L$ — Shine laser light for a time $\tau_L$. The final polarization of the nuclei is proportional to the incident light power and approaches this value with a time constant which is comparable to the spin-lattice relaxation time for the nuclei $T_1$[22]. The diffusion of the nuclear polarization from the quantum well to the surrounding barriers during $\tau_L$ also enhances the signal from nuclei in the barrier. Hence, in order to measure very small shifts, we found it necessary to suppress the barrier signal by reducing $\tau_L$ to only a few seconds.

$\tau_D$ — Stop shining the light, and wait for a time $\tau_D$ so that the system temperature can reach equilibrium. The lattice temperature would be in equilibrium with the bath temperature within 0.7 secs after the light was turned off. We usually waited for 20-40 seconds since the nuclear relaxation rates were even much longer.

**DET** — Irradiate with nuclei with a radio frequency pulse with which we acquired the NMR signal. At low temperatures, the peak to peak voltage of this pulse is reduced in order not to overheat the electron spins. This effect will be explained in more detail in chapter 3.

Shown in Fig.2.4 are some NMR spectra acquired **without** optical pumping taken at room and low temperature. In these spectra, the NMR signal is dominated by the substrate and the barrier, due to the much larger number of nuclei present there compared to the quantum well. The signal from nuclei inside the quantum well is shifted to lower frequencies (due to a negative effective $g^*$ and a positive $g = 2$) and can barely be seen in Fig.2.4c. Due to paramagnetic impurities in the rotation stage, the barrier signal is shifted by 3.5 kHz on cooldown from room temperature.

Shown in Fig.2.5 are some OPNMR spectra acquired with optical pumping taken at room and low temperature. Note that the OPNMR signal is inverted with respect

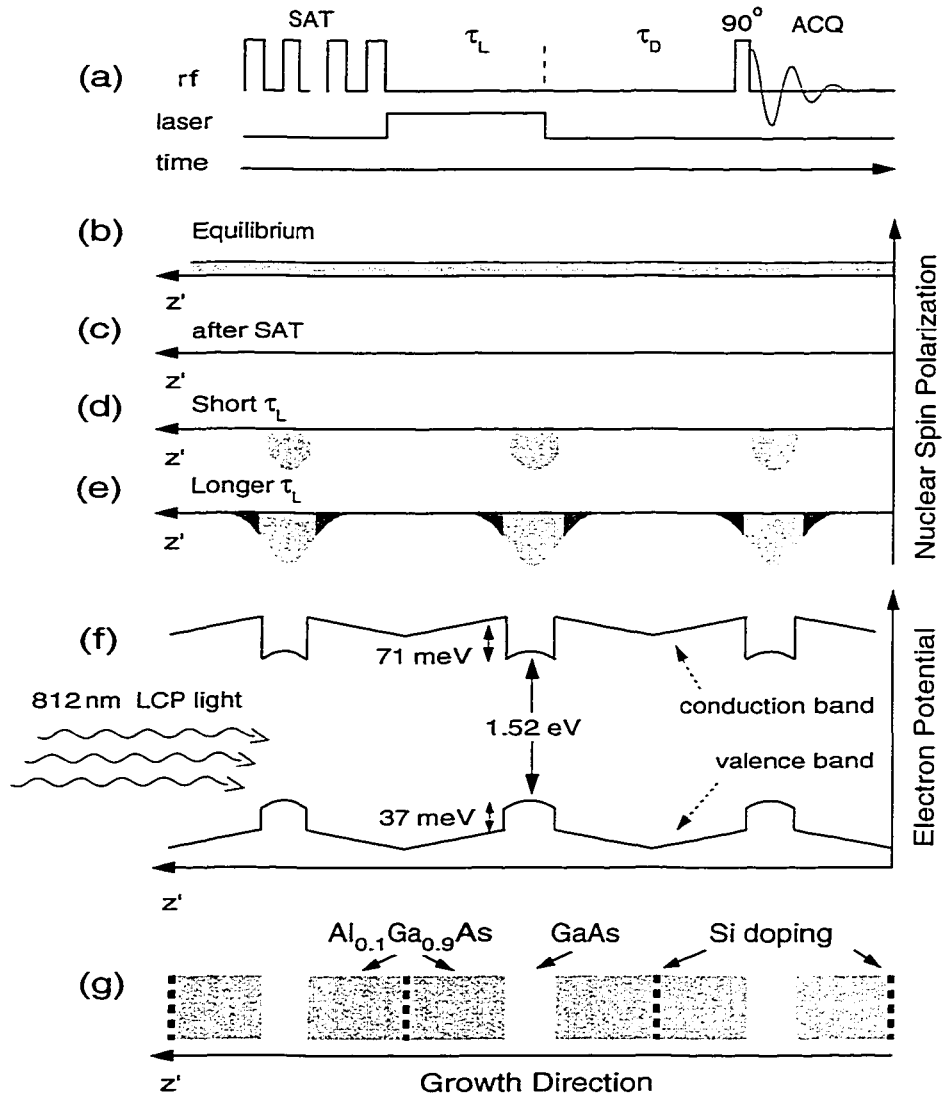


Figure 2.3: (a) – OPNMR timing sequence, which includes a saturating train of rf pulses (SAT), a "Light on" period $\tau_L$ followed by a "Dark time" $\tau_D$; a single 90° tipping pulse, and NMR acquisition (ACQ). (b–e) – the nuclear polarization in the spatial dimension $z'$, along with (f) the band diagram and (g) the schematic of the sample, same as in Fig. 2.1.

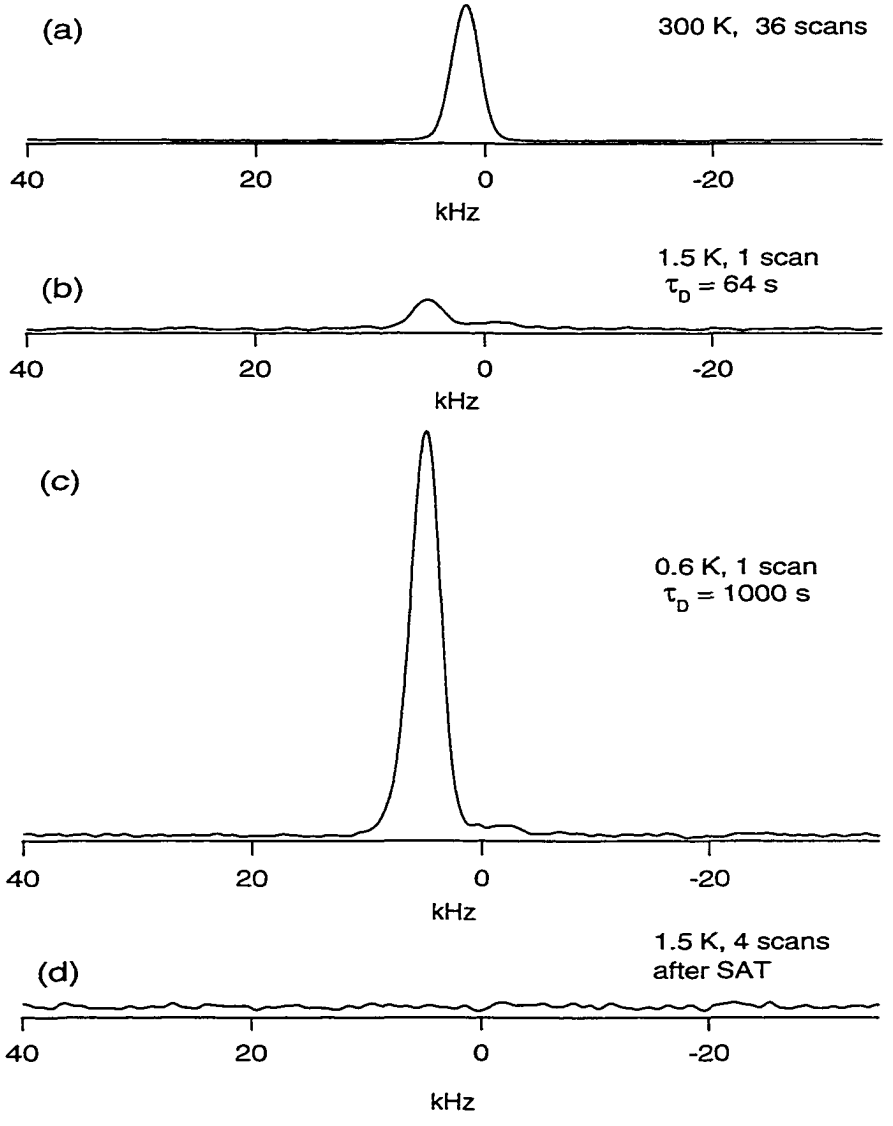


Figure 2.4: $^{71}$Ga NMR spectra of sample 40W, acquired **without** optical pumping at $B_{\text{tot}} = 12\,\text{T}$ ($f_o = 155.93\,\text{MHz}$). All these spectra are acquired using the sequence described in text with $\tau_L$=0. (a) An average of 32 scans at room temperature with the dark time $\tau_D$=2s, (b) a single scan at 1.5K taken with $\tau_D$=64s, (c) a single scan at 0.6K with $\tau_D$=1000s, and (d) an average of 4 scans, each taken immediately after the saturation pulse train, i.e., with $\tau_D$=0s. The quantum well signal to the right of the barrier can barely be seen in (c).

to the NMR signal. This happens because we can optically pump nuclear spins into the less enegertically favorable spin state. Since the nuclear spins have a much shorter spin-spin relaxation time compared to the spin-lattice relaxation time, they achieve a uniform spin temperature that is negative, which slowly changes to a positive quantity as the nuclear spins relax. Here, the NMR signal from nuclei can be clearly distinguished from the barrier NMR signal. In Fig.2.5, increasing the optical pumping time from (a) $\tau_L$=90s to (b) $\tau_L$=680s not only increases the strength of the NMR signal, but also increases the strength of the barrier signal relative to the signal in the well, due to the diffusion of spin polarization from the well into the barriers. Let us consider the expected shape of the spectra in more detail.

### 2.0.8 Description of Intrinsic Line Shape

As we have seen before, a $^{71}$Ga OPNMR emission spectrum at $\nu=\frac{1}{3}$ (Fig.2.7, solid line) exhibits a peak labeled "w" that arises from nuclei in the GaAs quantum well and a peak labeled "b" that is due to nuclei in the $Al_{0.1}Ga_{0.9}As$ barriers. The Fermi contact hyperfine coupling between the spins of the 2DES and nuclei in the well shifts the "w" peak below "b" by a frequency $K_S$, which we define to be the Knight shift[43, 50, 51]. Although the samples are characterized by "simple" NMR parameters (i.e., isotropic hyperfine coupling in an oriented single crystal), the OPNMR spectra are complex in that they can simultaneously exhibit inhomogeneous broadening due to the quantum confinement of electrons within a well and *motional narrowing* due to delocalization of electrons along the well.

The inhomogeneous broadening of the well line shape has two origins: (i) the quantum confinement within the well that causes the electron density to vary across its width and (ii) the optical pumping preferentially polarizes nuclei in the center of

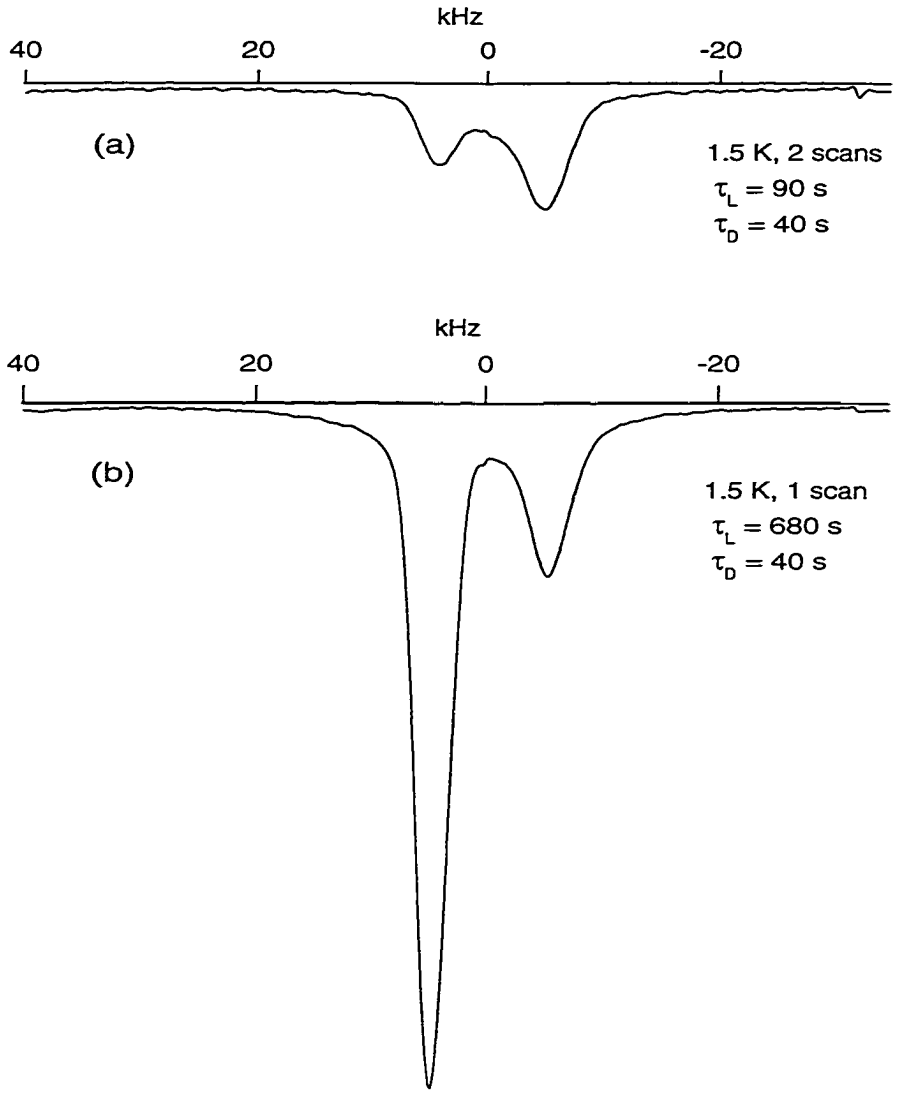


Figure 2.5: $^{71}$Ga NMR spectra of sample 10W, acquired **with** optical pumping at $B_{\text{tot}} = 12\,\text{T}$ (tilted by $\theta$=36.8°). Increasing the optical pumping time from (a) $\tau_L$=90s to (b) $\tau_L$=680s not only increases the strength of the NMR signal, but also increases the strength of the barrier signal relative to the signal in the well. The dark time for both spectra is $\tau_D$=40s. The signals appear inverted because of the negative nuclear spin temperature achieved after optical pumping.

the well. The three dimensional density $n_{3D}(z')$ shown in Fig.2.6 is a calculation by T. Jungwirth using density functional theory for sample 10W for $\nu$=1/3 in $B_{tot}$=12T. Also shown in the same figure are $n_{3D}(z') = \frac{2n}{w}Cos^2[(z'-w/2)/w]$ for $|z'| \leq w/2$[52, 53], and $n_{3D}(z')=\frac{2n}{w_{eff}}Cos^2[(z'-w/2)/w_{eff}]$ for $|z'| \leq w_{eff}/2$. Note that the latter is a very good approximation to the exact three dimensional electron density.

With either form for $n_{3D}(z')$, the intrinsic line shape (Fig. 1A, shaded region) may be written as the sum of $I_{\rm w}^{\rm int}(K_{S\rm int}, f) = [f/(K_{S\rm int}-f)]^{1/2}$ (derived below) and $a_b\delta(0)$ for the unbroadened barrier signal. Using a 3.5 kHz full-width at half-maximum (FWHM) Gaussian $g(f)$ for the nuclear dipolar broadening [43], we arrive at a two-parameter fit (dashed line) to the spectrum:

$$I(f) = a_{\rm b}\, g(f) + \int_0^{K_{S\rm int}} df' g(f-f')\, I_{\rm w}^{\rm int}(K_{S\rm int}, f') \tag{2.1}$$

The first parameter $a_{\rm b}$ is the amplitude of the barrier signal, which grows during $\tau_L$ as the optically pumped nuclear magnetization diffuses out of the quantum well. The second parameter extracted from the fit is the hyperfine shift for nuclei in the center of the well, $K_{S\rm int}(\nu,T) = A_c\mathcal{P}(\nu,T)n_{\rm 3D}(z{=}0)$. A comparison of $K_{S\rm int}(T\to 0)$ in three different samples yields $A_c = (2.8\pm 0.2)\times 10^{-13}\,{\rm cm}^3/{\rm s}$, which makes $K_{S\rm int}$ an *absolute* measure of the electron spin polarization.

Thus, fits to OPNMR spectra at various $\nu$ and $T$ provide a direct measure of the electron spin polarization $\mathcal{P}(\nu,T) \equiv \frac{\langle S_z(\nu,T)\rangle}{\max\langle S_z\rangle}$ in the quantum well.

Note that even though NMR is a local probe, the fitting function has no explicit dependence on the (x,y) position of nuclei along the quantum well. This is because the fit is generated under the assumption that all electron spins are *delocalized*, so that $\langle S_z(\nu,T)\rangle$, averaged over the NMR time scale ($\sim 20\,\mu$sec), appears spatially homogeneous along the plane of the wells, and thus the resulting lineshape is "motionally-narrowed" [43]. In this limit, measurement of $K_S$ reveals the "global",

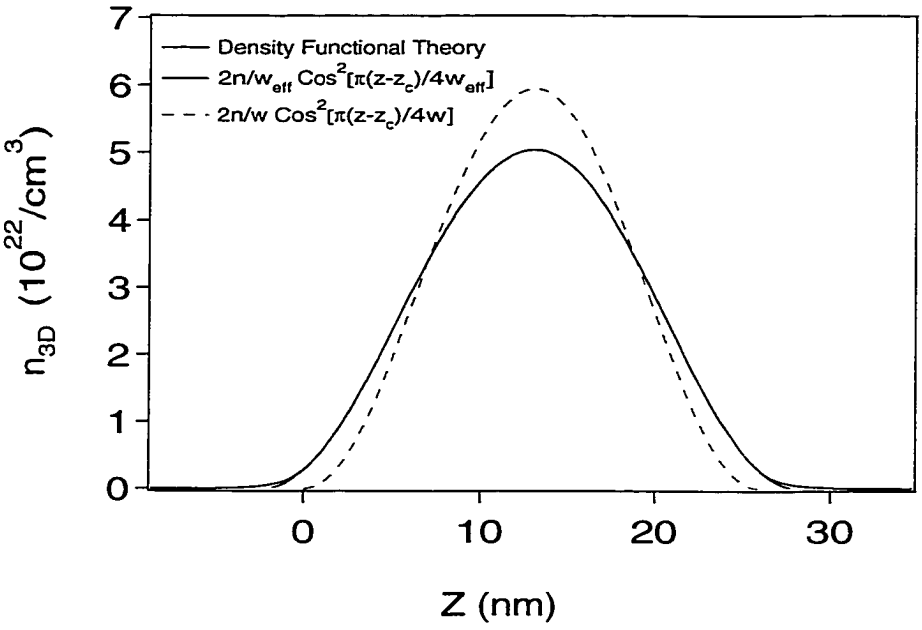


Figure 2.6: For Sample 10W at $\nu$=1/3 in $B_{tot}$=12T, the three dimensional density, $n_{3D}$, calculated using density functional theory(solid line)[54], the cosine squared wavefunction for a particle in an infinite well $\frac{2n}{w}Cos^2[(z'-w/2)/w]$ (dashed line), and $\frac{2n}{w_{eff}}Cos^2[(z'-w/2)/w_{eff}]$ (solid line). The latter almost completely overlaps with the density functional solution over a wide range of z. For sample 10W, $w_{eff}$ = 307Å and $w$ = 260Å under these conditions.

time-averaged value of the electron spin polarization $\mathcal{P}$.

For a quantitative understanding of the intrinsic spectrum, we must consider the specific assumptions that lead to $I_w^{int}(K_{Sint}, f)$=$[f/(K_{Sint}-f)]^{1/2}$. Nuclei within the well couple to the spins of the 2DES through the isotropic Fermi contact interaction[22, 33, 55, 56, 43], thus a nucleus at site $\vec{R}'$ experiences a hyperfine magnetic field

$$\vec{B}^e(\vec{R}') = (-16\pi\mu_B/3)\sum_j \vec{S}_j\delta(\vec{r}_j - \vec{R}'), \tag{2.2}$$

where $\mu_B$ is the Bohr magneton, $\vec{S}_j$ is the spin of electron j, the summation is over all of the conduction electrons within the well, and the delta function picks out those electrons that overlap with the nucleus at $\vec{R}'$. The average projection of $\vec{B}^e$ along the

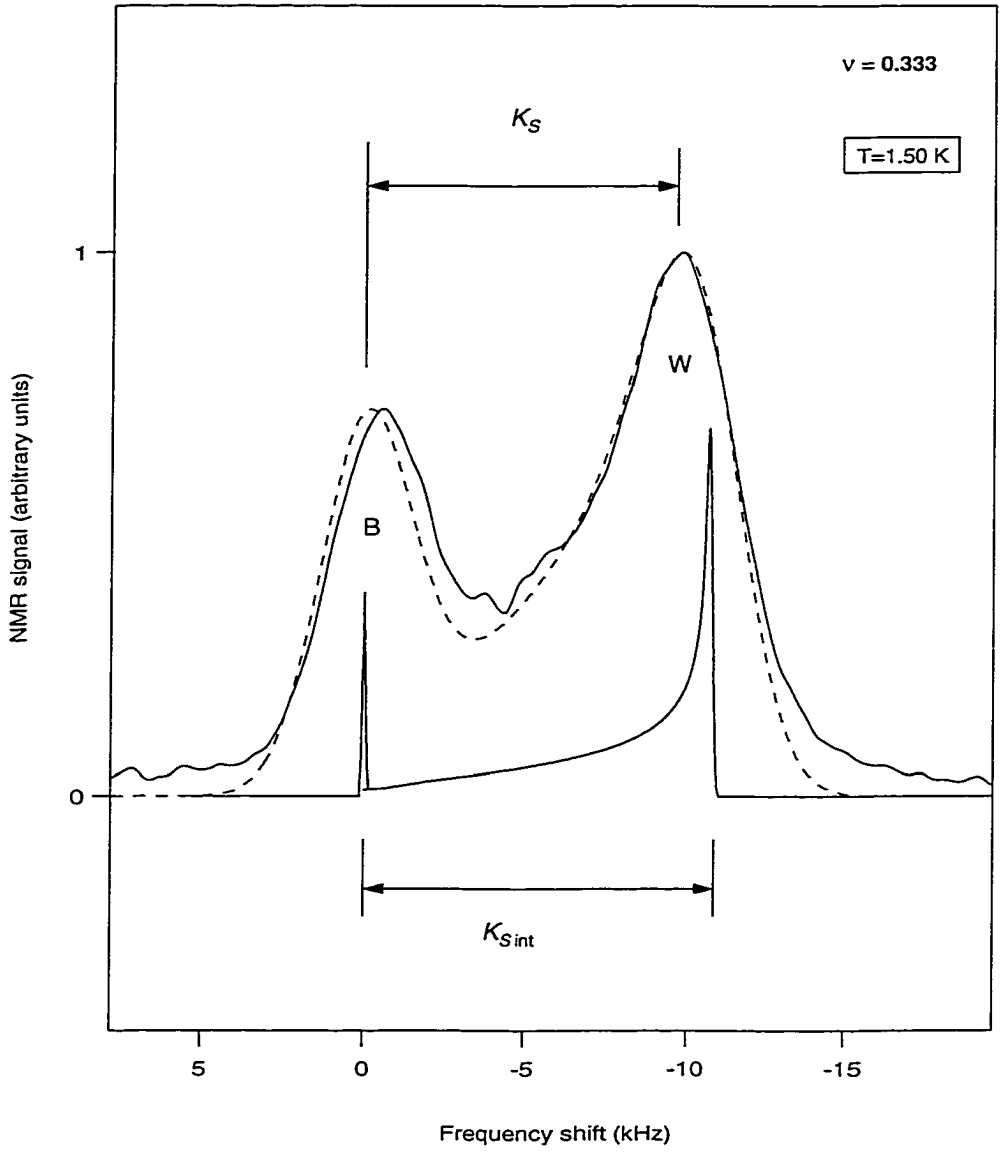


Figure 2.7: A $^{71}$Ga emission spectrum (solid line) of sample 10W, taken at $\theta$=36.8° and $T = 1.5\,\mathrm{K}$, in $B_{\mathrm{tot}} = 12\,\mathrm{T}$ (155.93MHz); the fit (dashed line, see Equation 2.1) is obtained by broadening the intrinsic line shape (shaded region) with a 3.5 kHz FWHM Gaussian. Empirically, $K_{S\mathrm{int}} = K_S + 1.1 \times [\,1 - \exp(-K_S/2.0)\,]$ (all in kHz).

applied field $\vec{B}_{\rm tot}$ may be written quite generally as:

$$\langle B_z^e(\vec{\mathrm{R}}',\nu,T)\rangle = (|^{71}u(0)|^2|\chi(Z')|^2|\phi(X',Y')|^2) \times(\frac{-8\pi\mu_B}{3})\mathcal{P}(\vec{\mathrm{R}}',\nu,T)(\frac{n}{w}). \quad (2.3)$$

Here, the probability density of finding electrons at a $^{71}$Ga site has been factored into a term with the periodicity of the lattice $|^{71}\mathrm{u}(0)|^2$ and terms which vary slowly within a unit cell $|\chi(\mathrm{Z}')|^2|\phi(\mathrm{X}',\mathrm{Y}')|^2$[50]. $\mathcal{P}(\vec{\mathrm{R}}',\nu,\mathrm{T})$ is the local spin-polarization ($-1<\mathcal{P}<1$) of the electrons at $\vec{\mathrm{R}}'$. If we assume that electrons are delocalized along the well, then the time-averaged values of $|\phi|^2$ and $\mathcal{P}$ are spatially homogeneous. In this limit, the local hyperfine frequency shift (taken to have the sign of $\mathcal{P}$) is a function of z' only: $\mathrm{f(z')}=-^{71}\gamma\langle B_z^e(\mathrm{z}',\nu,\mathrm{T})\rangle/2\pi\approx\cos^2(\pi\mathrm{z}'/\mathrm{w})K_{S\mathrm{int}}$, so the general expression for the well line shape is $I_{\mathrm{W}}^{\mathrm{int}}(\mathrm{f}')=\sum_{\mathrm{N-wells}}\int\mathrm{d}^3r'\langle^{71}\mathrm{I}_z(\mathrm{z}')\rangle\rho_{\mathrm{nuclear}}\delta(\mathrm{f}'-\mathrm{f}(\mathrm{z}'))$. We further assume identical wells, and that the optical pumping gives rise to a nuclear polarization that varies across each well as $\langle^{71}\mathrm{I}_z(\mathrm{z}')\rangle \sim \mathrm{f(z')}$, which leads to the form $I_{\mathrm{W}}^{\mathrm{int}}(\mathrm{f}') = [f'/(K_{S\mathrm{int}}-f')]^{1/2}$ shown in Fig.2.7.

### 2.0.9 Determining the Density

Fig. 2.8 shows $K_S$ measurements in the two samples near $\nu$=1. The excellent agreement between positive $\theta$ (squares) and negative $\theta$ (circles) data is consistent with the rotator accuracy of $\pm 0.1°$. We infer the densities $n$ from these measurements assuming that $K_S(\theta)$ peaks at $\nu$=1, hence determining $n_{40\mathrm{W}} = 6.69\times10^{10}\,\mathrm{cm}^{-2}$ and $n_{10\mathrm{W}} = 7.75\times10^{10}\,\mathrm{cm}^{-2}$, consistent with low-field magnetotransport characterization of the wafers. These values are very robust, as the four independent runs shown in Fig. 2.8 for sample 40W reproduce $n$ to within $\pm 0.5\%$.

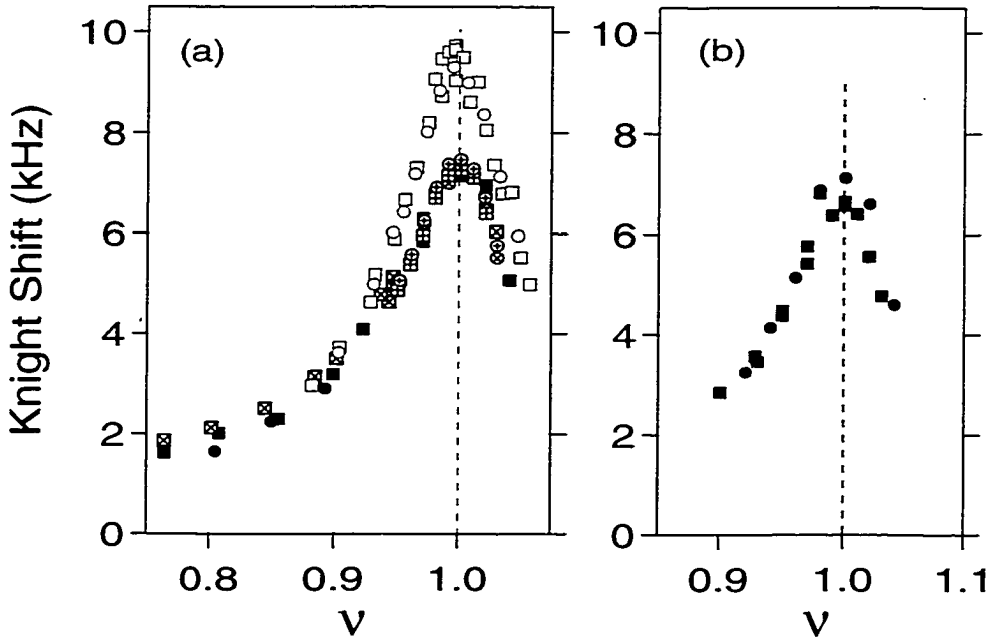


Figure 2.8: $K_S(\nu)$ near $\nu$=1 at $T$=1.5 K. (a) Samples 40W (filled symbols, three separate runs) and 10W (open symbols) at $B_{\rm tot}$=3.6263 T. (b) 40W at $B_{\rm tot}$=3.2589 T. The densities are $n_{40\rm W} = 6.69 \times 10^{10}\,{\rm cm}^{-2}$ and $n_{10\rm W} = 7.75 \times 10^{10}\,{\rm cm}^{-2}$.

Note that the sharp peak in $K_S$ at $\nu$=1 is quite similar to the "skyrmion feature" previously observed in a higher density sample at stronger $B_{\rm tot}$ [22]. The number of spin-flips of the skyrmion inferred from Fig. 2.8 ($\tilde{\mathcal{S}}$=$\tilde{\mathcal{A}}$=3.1 for $B_{\rm tot} \sim 3.5$ T) is slightly larger than before ($\tilde{\mathcal{S}}$=$\tilde{\mathcal{A}}$=2.6 for $B_{\rm tot} \sim 7$ T), in qualitative agreement with the change in $E_Z/E_C$[24, 25]. Here, we use the convention that $\tilde{\mathcal{S}}$=$\tilde{\mathcal{A}}$=0 in the non-interacting limit, instead of the original definition [22], $\mathcal{S}$=$\mathcal{A}$=1, in the same limit. However, a quantitative comparison to the skyrmion model will require data below 1.5 Kelvin, since $\mathcal{P}(\nu$=1) is only $\sim$80% in Fig. 2.8.

### 2.0.10 More Experimental Details

**Low Temperature: Probe and Cryostat Design**

The low-temperature (0.29 K$<T<$1.5 K), high-field ($B_{\text{tot}}$=12 T) OPNMR measurements described below were performed using an Oxford Instruments sorption-pumped $^3$He cryostat mounted in a Teslatron$^H$ superconducting magnet. The samples, about 4 mm by 6 mm by 0.5 mm, were in direct contact with helium, mounted on the platform of a rotator assembly in the NMR probe. A calibrated $RuO_2$ thermometer, in good thermal contact with the sample, was used to record the temperature during signal acquisition. In order to improve the signal to noise in our experiments, we put the NMR tank circuit inside the probe, as close to the sample as we could. This meant however, that we needed to provide a external means to vary the two capacitors that would be at the low temperature end of the probe. This was accomplished by two stainless steel rods that went down the length of the probe from the room temperature top to the low temperature bottom. Turning a rod from above changes the distance between the two plates of a capacitor, and hence its capacitance.

In order to vary $\nu$=$nhc/eB_{tot}cos\theta$ precisely, the sample has to be inclined to a known angle to better than 0.1°. This was achieved by having a third stainless steel rod inside the probe that let us to turn the sample to any desired angle from outside.

The rods were chosen to be thick enough to be able to turn the capacitances and the sample stage, and yet not be large sources of heat leaks from the outside world. The optical assembly was also a potentially lethal heat source, since it dissipated half of the incoming optical energy right at the polarizer. For this reason, it was necessary to have it close to the 1K pot, about 22 cms away from the sample. The $^3$He cryostat was designed to supply about 10mW of cooling power for half an hour at 400mK before one needed to recharge the $^3$He. Recharging was done by heating the charcoal sorb to expel the $^3$He gas and then recondensing the $^3$He liquid at 1.5K, a process

that usually took about a half hour before we could return to the base temperature.

Turning the sample to the required angle within 0.1° turned out to be quite an endeavor. The orginal sample rotating mechanism provided with the probe from the manufacturer turned out to be only accurate to about 2°. The fault lay with the "swedish rotater" design that required a very precise spiral grooved onto the flat end of a cylinder. By remachining this spiral and making small design changes in the original rotating mechanism, we were able to control the angle $\theta$ with the desired precision. It was much easier to achieve the same precision in the angle $\theta$ with a prototype design that replaced the spiral gear with a worm gear, but space constraints forced us to improve the spiral design.

### Laser Light and Setup

As described above, light of a certain frequency, ~812 nm in GaAs, is needed to excite the electrons from the valence band to the conduction band in order to hyperpolarize the nuclei. We used light from a Ti:Sapphire laser that was pumped by an Argon-Ion laser. Diode lasers that work in this frequency range can also be used (and are usually much cheaper), but they have a smaller range of frequencies that they can be tuned over (~12nm compared to ~150nm for the Ti:Sapphire). Hence, in our early experiments, we decided to use a Ti:Sapphire laser in order to have the larger range of laser frequencies. Once we determined the frequency range of interest, we also built a diode laser setup that could be used with our samples. The original experiments at Bell Labs did not use optical fiber to deliver light to the sample, instead they used an optical window on the $^4$He cryostat. In our experiments, we decided that the benefits of attaining much lower base temperatures (~300mK compared to ~500mK) made the use of an optical fiber (hence, no optical window and smaller radiation losses) worth the trouble. There are several issues that one needs

to worry about when using optical fiber to supply polarized light in a low temperature environment. There are very few polarizers and quarter wave plates that still work at low temperature. The polarizer that we used was made by Corning and was suggested to us by Prof. Don Heiman at MIT[57]. They also told us about a Polaroid quarter wave plate that works at low temperature. One also needs to break the connection from the fiber that goes down the length of the probe to one that comes from the optical table. Originally, we decided to go with a older style of fiber connectors, the TC connector, which turned out to be unreliable. A newer design which employs a ceramic end, the FC connector proved to be more reliable in making and breaking joints. The FC connector was also less lossy, allowing about 85-90% of the light through the fiber. In order to get light from the laser into the fiber, we decided to use a joint fiber connector-lens assembly made by Thorlabs. This assembly was placed on a stage that could be moved in two directions perpendicular to the beam. Since we only needed about 10-50 mW of light from the laser, we operated the laser at the optimal power setting suggested by the manufacturer, about 1.5W, and then used a quarter wave plate and beam splitter to dump away the rest of the energy into a beam dump. The rest of the beam was then send down the fiber. Inside the probe, there was an assembly that contained the polarizer and the quarter wave plate. This assembly was strategically placed close to the 1K pot, which meant that the light had to travel a long distance, about 22cm from the assembly to the sample. Hence, it was important for us to check that the light was hitting the sample at room temperature. The assembly was designed symmetrically so that changing the temperature would change all the lengths in the same way and the light would then still hit the target.

### NMR Magnet, Spectrometer and Tank Circuits

Magnets for NMR purposes are designed to meet several stringent requirements imposed by the physics of magnetic resonance. Usually spectral features are the narrowest in liquid state NMR, where one might be interested in resolving two frequencies that are only 0.01 ppm apart. In solid state NMR, however, the requirements are less severe, due to the large linewidths ($\sim$ 3.5 kHz) of the individual lines caused by the nuclear spin-spin coupling. Still, we have measured shifts in our data with an error bar as small as 150 hz, or 1 ppm. The magnetic field has to be very homogenous in order for us to resolve such small differences. In the NMR magnet used to make these measurements, the magnetic field did not deviate by more than 0.2 ppm in the cubic cm of interest (the region containing the largest magnetic field). This deviation turned out to be much smaller than the 1 ppm specification guaranteed by the manufacturer. The sample size was small enough to fit comfortably inside this cubic cm. We can create and characterize this homogeneous region ourselves, by measuring the NMR resonance frequency of a small $D_2O$ droplet, and using the droplet to map the magnetic field. The magnet is equipped with 6 shim coils surrounding the main solenoid that we can use to cancel the magnetic field gradients. When we made our measurements, we found to our surprise that the 1.5K $^4$He bucket dewar didnt distort the field inside it, but the 0.3K $^3$He cryostat modified the field sufficiently enough($\sim$ 1ppm) that we had to correct for it. NMR superconducting magnets usually have extremely small drifts of the magnetic field with time. The magnetic field drift rate in our magnet has a value of 0.1 ppm per hour after one hour of closing the switch that completes the superconducting loop. Typically, the magnetic field drift rate approaches 5 ppb/hour after about a week of keeping the magnet in the superconducting mode. Using deuterium NMR, we can measure drift rates which are as small as 0.1 ppb per hour in a day. In order to get the magnet to settle into a low magnetic field drift rate mode as soon as possible after closing the superconducting switch, it is best

Table 2.2: NMR parameters for nuclei of interest in GaAs.

| | $^{71}Ga$ | $^{69}Ga$ | $^{75}As$ |
|---|---|---|---|
| Nuclear Spin $I$ | $\frac{3}{2}$ | $\frac{3}{2}$ | $\frac{3}{2}$ |
| Natural abundance (%) | 39.9 | 60.1 | 100 |
| Gyromagnetic ratio $\frac{\gamma}{2\pi}$, $(\frac{MHz}{T})$ | 13.00 | 10.23 | 7.30 |
| Electric Quadrupole Moment $Q$, $(10^{-8}\text{Å}^2)$ | 0.11 | 0.17 | 0.31 |

to following the "exact" instructions as provided by the manufacturer for our magnet, i.e., to let the magnet overshoot the final magnetic field value by 0.017T and then bring it back to final field value after 15mins. Small deviations from this procedure can cause the magnetic field drift rate to behave very erratically, and one is required to redo the entire procedure.

Shown in Table 2.2 are NMR parameters for nuclei of interest in GaAs. From this table, we find that the NMR resonance frequency for $^{71}Ga$ in the maximum field that we could generate (12 T) is 155.9 MHz. Hence, using parts supplied from different vendors, we built a NMR spectrometer that could work up to 200MHz. This spectrometer includes a very high quality low noise preamplifier from MITEQ, several mixers and couplers from Mini-Circuits, a frequency synthesizer from PTS and a high power amplifier from Kalmus. The noise temperature of our preamps is about 80-90 K (noise figure $\sim$ 1.2 db). It is possible to to achieve better noise figures using cooled preamps, but in frequency ranges that are not of interest (> 1GHz) to us. We usually crimped our own 50$\Omega$ BNC cables, since we often needed one of a specific length. In order to detect the NMR signal from nuclei inside the sample, one first needs to excite the resonance by irradiating the nuclei with short, high power radio frequency pulses that are tuned to the Larmor frequency. The effect of this short pulse (typically 10$\mu$s) is to tilt the direction of nuclear polarization with respect to $B_{tot}$, and can be described by an angle $\theta$. 90° pulses leave the residual nuclear polarization in the $x-y$ plane and generate the largest NMR signal. We found to our dismay that the high

voltages needed for a short $\sim 90°$ pulse induced arcing inside the low temperature, low pressure $^3$He environment, in addition to heating the electron spins under certain low temperature conditions. After working hard to alleviate some of the problems that aggravated the arcing[58], we resorted to lower voltage tipping pulses in order to make equilibrium measurements, with a subsequent small loss in signal to noise. This aspect, including our non-equilibrium measurements will be described in more detail in chapter 3.

All of our instruments were controlled via the computer with IGOR programs that we wrote ourselves. IGOR is a multi-purpose programming language/graphing program for the Macintosh (and recently PC) that allows the user to control laboratory GPIB programmable instruments. Igor proved to be quite versatile, as we were also able to use IGOR to perform some of complex simulations to be described in chapter 3.

Finally, lets try to understand how an NMR tank circuit works. An NMR tank circuit (consisting of an inductor L, 2 capacitors $C_t$ and $C_m$, and a resistance r) is used to irradiate the nuclei with radio frequency pulses and subsequently detect the NMR signal. The sample to be studied is placed inside the inductor L, and the resistance r is usually the small resistance of the coil that is used to make the inductor. It is simpler to first consider just part of the NMR tank circuit (full circuit shown in Fig. 2.10), the LCR circuit[59, 60] in Fig. 2.9, which does not contain $C_m$. Here, L and r are in series, and the tuning capacitor $C_t$ is in parallel to these two components. The impedance, ie. the resistance and reactance of such a combination is shown in the figure. Note that the resistance has a peak value of $(wl)^2/r$ (when $wl >> r$), when the reactance drops to zero. The NMR signal is generated by the sample inside the inductor when it is irradiated with a short radio frequency pulse tuned to the larmor frequency of the nuclei. In order for the complete NMR signal to be transmitted from

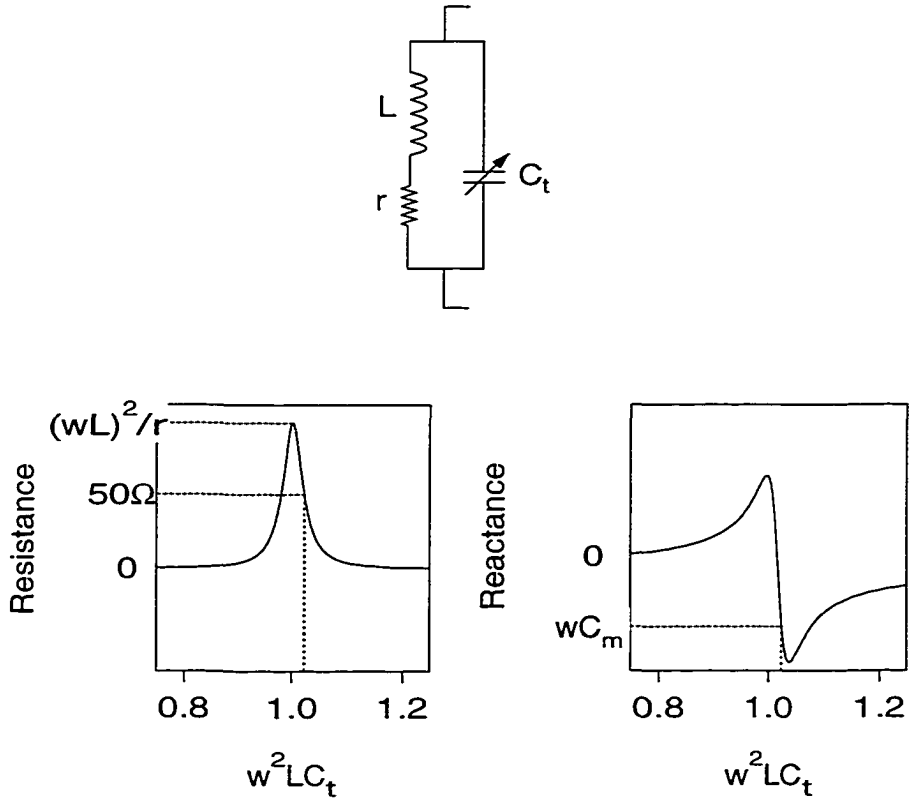


Figure 2.9: Resistance and Reactance as a function of $C_t$ in an LCR circuit.

the sample to the preamplifier without getting reflected, however, the impedance of the complete tank circuit has to match the impedance of the preamplifier, i.e., the resistance has to be 50Ω and the reactance has to be 0. In order to achieve this combination, we have to add another component to the LCR circuit. The two ways to do so are shown in Fig. 2.10.

(a) The tuning capacitor $C_t$ of the LCR is biased so that the resistance of the LCR circuit is 50Ω, and then a matching capacitor $C_m$ is added in series to the LCR circuit to cancel the remaining reactance.

(b) Here, the matching capacitor $C_m$ is added in series to the inductor to decrease the maximum of the resistance of the LCR circuit $(\omega L - 1/\omega C)^2/r$ to 50Ω, while the tuning capacitor is biased so that the reactance of the LCR circuit is 0.

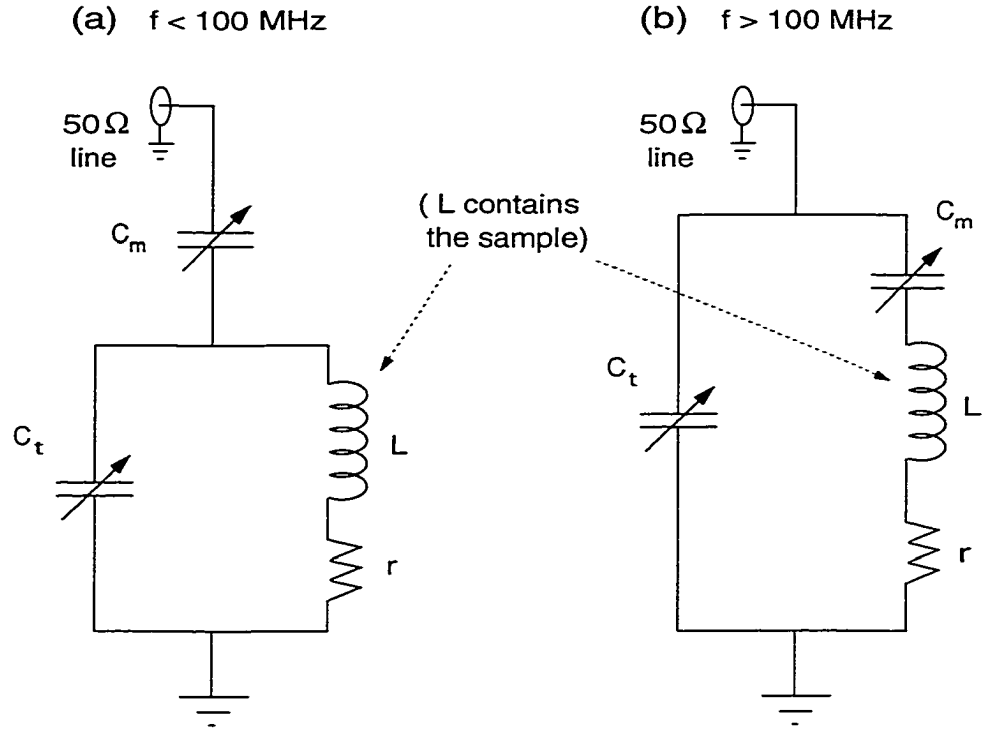


Figure 2.10: Series-parallel (a) and parallel-series (b) resonant tank circuits used in our NMR probe. For (a) $C_t \approx 1/[\omega^2 L(1+\sqrt{r/50\Omega})]$; $C_m \approx \sqrt{r/50\Omega}/(\omega^2 L)$. For (b) $C_t \approx 1/(\omega\sqrt{r \times 50\Omega})$; $C_m \approx 1/(\omega^2 L - \omega\sqrt{r \times 50\Omega})$.

The variable capacitors usually had to be supplemented by fixed capacitors in the 1–120 pF range. For a typical 6-turn copper coil and the 2–25 pF variable capacitors that could fit into our limited probe space, it was advantageous to use "b" as opposed to "a" above $\sim$100 MHz.

# Chapter 3

# $\nu$=1/3: Tiny Spin Flips and Ultraslow Motion!

As we have seen before, the filling factor $\nu$=1 turns out to have interesting features due to the electron-electron interactions, that can be probed by NMR. It was only natural to expect that these effects might be far stronger for the $\nu$=1/3 state, since the existance of the $\nu$=1/3 state is entirely due to interactions. The NMR apparatus was designed to allow us to reach lower temperatures, higher magnetic fields, and have a more precise rotation mechanism than before. All the new features of this experiment would turn out to be crucial to see most of the physics that will be described in the next few chapters.

In this chapter we will present $\mathcal{P}(T)$ data at $\nu=\frac{1}{3}$ that probe the neutral spin-flip excitations of a fractional quantum Hall ferromagnet. In addition, away from $\nu$=1/3, we find evidence for ultraslow electron spin dynamics below 0.5 K, with characteristic time scales exceeding $\sim 40\mu$s. At low temperatures ($T\sim$0.5 K), a dramatic change in the NMR linewidth is observed whenever spin-reversed electrons are present. This striking behavior is due to the localization of spin-reversed electrons over the NMR time scale. At higher temperatures, where the spin-reversed electrons are no longer

localized, the saturated $\mathcal{P}(\nu)$ drops on either side of $\nu=\frac{1}{3}$, even in a $B_{\rm tot}$=12 Tesla field. The observed depolarization is quite small, consistent with an average of $\sim$ 0.1 spin-flips per quasihole (or quasiparticle), a value which does not appear to be explicable by the current theoretical understanding of the FQHE near $\nu=\frac{1}{3}$. Finally, by varing NMR pulse parameters (by increasing the voltage used for the tipping pulse), we can drive the electron spin temperature (as measured by the Knight shift) above the lattice temperature $T$ (for $T < 0.5$K). These non-equilibrium measurements imply that the electron spin-lattice relaxation time is 100 $\mu$s$<\tau_{1s}<$ 500 ms, at $\nu$=1/3, which appears to exceed all electronic time scales previously measured in semiconductors by at least a factor of 1000.

### 3.0.11 Temperature Dependence at 1/3

Fig. 3.1 shows OPNMR spectra (solid lines) over a range of temperatures at $\nu=\frac{1}{3}$. At $\nu$=1/3, the OPNMR spectra are well described by the dashed line fits generated by our model for the lineshape described in detail in Chapter II. The central assumption of this model is that the electron spins are delocalized along the well, such that $\langle S_z(\nu,T)\rangle$ appears spatially homogeneous, when averaged over the NMR time scale ($\sim$40 $\mu$s). For nuclei in the center of the well, $\mathcal{P}$ can fluctuate between $\pm$1, resulting in local frequency variations of $\pm K_{S\rm int}$. Thus the NMR time scale separating fast and slow fluctuations is $\sim (2K_{S\rm int})^{-1} \approx 40$ $\mu$s. In this limit, the delocalization of the low density 2DES (there are $\sim 10^6$ nuclei per electron in the well) produces a "motional narrowing" of $I_{\rm W}^{\rm int}$.

Each sample was tilted by the angle $\theta$ necessary to achieve $\nu=\frac{1}{3}$ in $B_{\rm tot}=12$ Tesla (where $\theta_{40\rm W}$=46.4°, $\theta_{10\rm W}$=36.8°). Fig. 3.2(a) shows $K_S$ as a function of temperature at $\nu=\frac{1}{3}$. Two different symbols are used for the 40W data, corresponding to independent

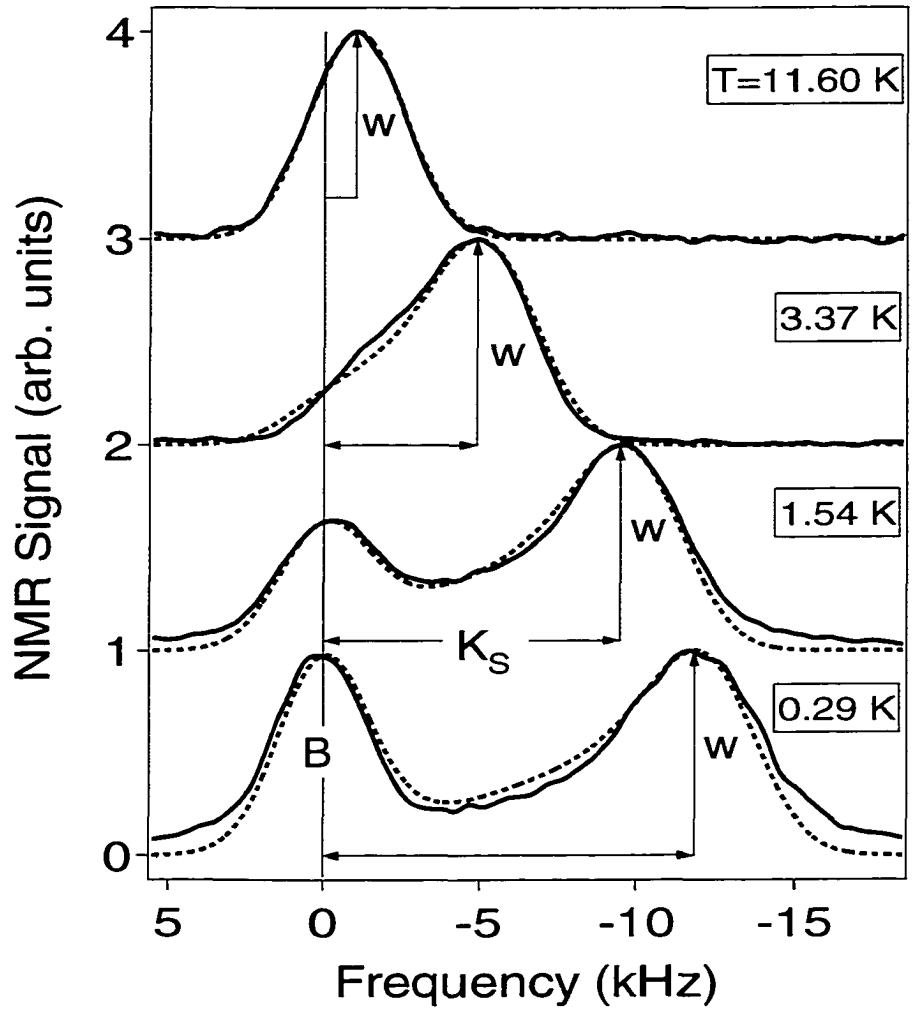


Figure 3.1: Solid lines: $^{71}$Ga OPNMR spectra of sample 10W at $\nu=\frac{1}{3}$, taken at $\theta = 36.8°$ in $B_{\rm tot} = 12\,{\rm T}$ ($f_o$=155.93 MHz). The dashed lines are fits, described in the text.

cool-downs from room temperature, which demonstrates the reproducibility of the data. The inset shows that $K_S$ saturates for both samples at low temperatures, as previously seen at $\nu$=1[22]. Note that it was very important to have a base cryostat temperature as low as $T_{base}$=0.3K in order to see the saturation clearly. In Fig. 3.2(b) we plot the corresponding temperature dependence of the electron spin polarization, using $\mathcal{P}(\nu=\frac{1}{3},T) = \frac{K_{S\rm int}(T)}{K_{S\rm int}(T\to 0)}$. The resulting curves are almost identical for the two

samples. The subtle differences that remain might be due to a slightly higher spin stiffness[61] for sample 10W.

The $\mathcal{P}(\nu=\frac{1}{3},T)$ data in Fig. 3.2(b) probe the neutral spin-flip excitations of a fractional quantum Hall ferromagnet. For comparison, the solid line is the polarization for *non-interacting* electrons for $\nu$=1/3. In this picture, the electrons occupy 1/3 of all the states in the lowest spin-up Landau level at $T$=0, and only start occupying the lowest spin-down Landau level as the temperature is raised above zero. The energies of these spin-split levels differ by the Zeeman energy, $E_Z$. The chemical potential and the polarization can be calculated using the following formulas (assuming that the energy of the spin-up level is zero):

$$\frac{1}{1+exp(-\mu/kT)}+\frac{1}{1+exp((E_Z-\mu)/kT)}=\frac{1}{3} \tag{3.1}$$

$$\mathcal{P}=3[\frac{1}{1+exp(-\mu/kT)}-\frac{1}{1+exp((E_Z-\mu)/kT)}] \tag{3.2}$$

It is suprising that the non-interacting picture does a better job of describing the polarization at $\nu$=1/3 then it does at $\nu$=1. Also shown (dashed line) is the polarization $\mathcal{P}^*(T)$ calculated for *non-interacting* electrons at $\nu$=1, where $\mathcal{P}^*(T)$=tanh($E_Z/4k_BT$), $B_{\rm tot}$=12 T, and $g^*=-0.44$. Both $\mathcal{P}(\nu=1,T)$[22, 62] and $\mathcal{P}(\nu=\frac{1}{3},T)$ saturate at higher temperatures than $\mathcal{P}^*(T)$, however, the data at $\nu=\frac{1}{3}$ lie much closer to this $\mathcal{P}^*(T)$ limit. Fitting tanh($\Delta/4k_BT$) to the saturation region of the data, we find $\Delta\approx 2E_Z$ at $\nu=\frac{1}{3}$, as opposed to $\Delta\approx 10E_Z$ at $\nu$=1[22]. We also note that the 40W data set is very well described by $\Delta = 1.82\,E_Z$ over the *entire* temperature range, in sharp contrast to the behavior at $\nu$=1. These results are consistent with the spin stiffness being much less at $\nu=\frac{1}{3}$ than at $\nu$=1[61]. While a recent numerical result[63] is in qualitative agreement with the data in Fig. 3.2(b), it remains to be seen whether other theoretical approaches, such as those used at $\nu$=1[64, 65, 66], can be modified to explain

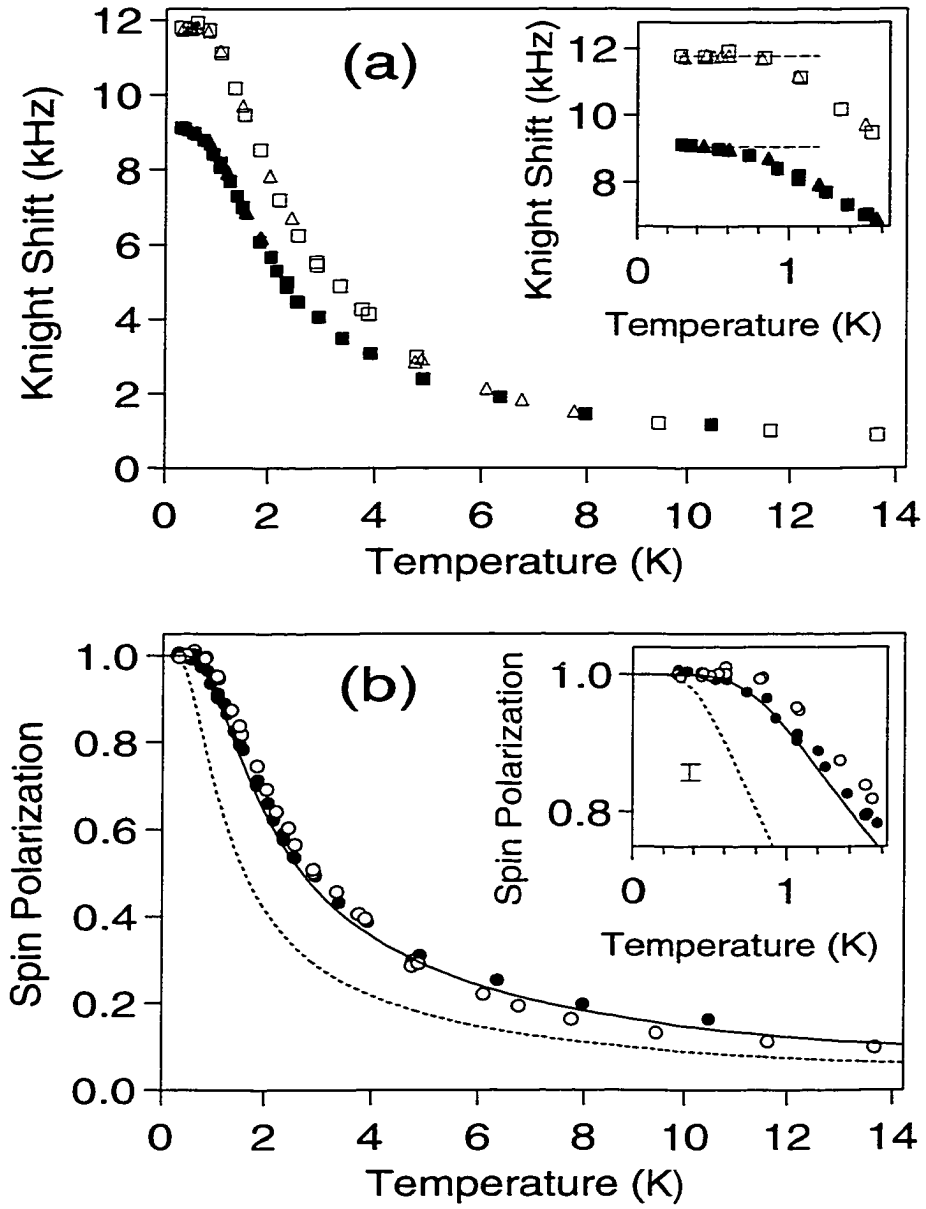


Figure 3.2: Temperature dependence of (a) $K_S$ and (b) $\mathcal{P}$ for samples 10W (open symbols) and 40W (filled symbols) at $\nu$=$\frac{1}{3}$ (with $B_{\rm tot}$ = 12 Tesla, $\theta_{40W}$=46.4°, and $\theta_{10W}$=36.8°). Dashed line is $\mathcal{P}^*(T)$, defined in the text. Insets show the saturation region (note the error bar). The solid line is the polarization for non-interacting electrons at $\nu$=1/3 as described in the text.

these data.

### 3.0.12 Wide Linewidth Spectra

Most of the data shown below were first analyzed without considering the width of the spectrum. The unusual lineshape made it hard for us to "see" changes in the linewidth without a fixed reference, and initially, we were under the impression that the width of the well resonance was identical for all the spectra that we measured. After a while, we realized that some of the spectra had very different linewidths, which could not be attributed to the different Knight shifts (for very small Knight shifts, the width of the well resonance is expected to decrease). This was an important discovery, since the width is another very important parameter that can be used to study the electronic system.

As Fig.3.3b demonstrates, low-temperature measurements at $\nu$=0.267 show a crossover to more complicated line shapes. Although the spectra are in reasonable agreement with our model above 1 K, the width of the "w" peak increases dramatically as the temperature is lowered to $T$=0.45 K and then decreases upon further lowering to $T$=0.31 K. This non-monotonic temperature dependence is reminiscent of the behavior seen in NMR studies of systems in which spectra are sensitive to dynamical processes[67], variously referred to as "motional narrowing," "dynamical averaging," or "chemical exchange"[43, 68, 69]. In our experiment, the nuclei are rigidly fixed in the lattice of a single crystal, so the variation in the line shape shown in Fig. 1B is a signature of electron spin localization, which turns off the "motional narrowing" of the well resonance as the temperature is lowered.

Figure 3.4 shows that the extra broadening of the well resonance disappears as the sample is tilted from $\theta_{10W}$=0° ($\nu$=0.267) to 36.8° ($\nu$ = 1/3), despite a 10% increase

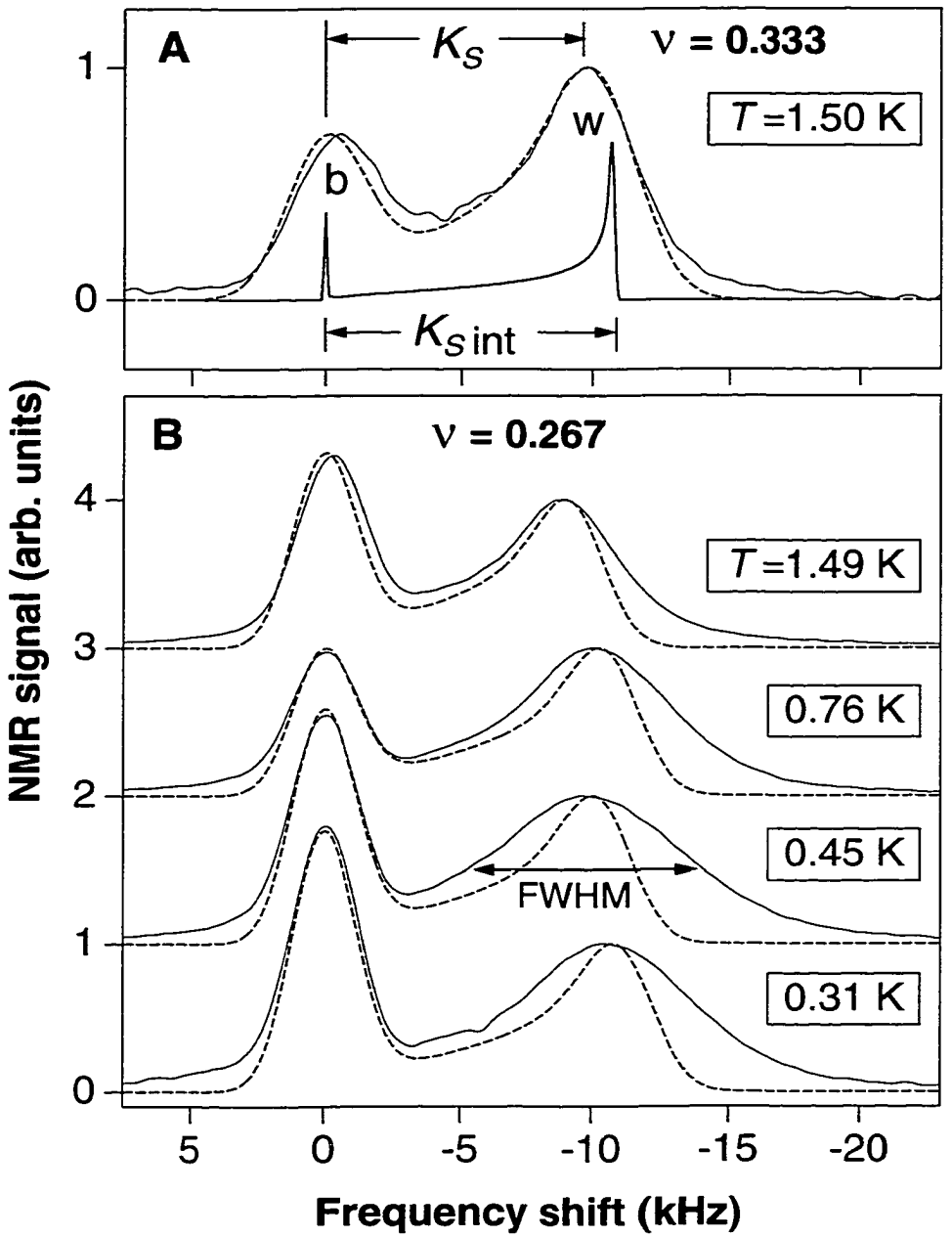


Figure 3.3: (**A**) $^{71}$Ga OPNMR spectrum (solid line) of sample 10W at $\nu=\frac{1}{3}$, taken at $\theta$=36.8° in $B_{tot}$=12 T. Frequency shift relative to $f_o$=155.93 MHz. The dashed line fit is obtained by broadening the intrinsic line shape (shaded region) as explained in the text. Empirically, $K_{Sint}=K_S+1.1\times(1-\exp(-K_S/2.0))$ (in kilohertz). (**B**) Temperature dependence of the spectra at $\nu$=0.267 ($\theta$=0°). The full width half maximum of the well resonance "w" is shown.

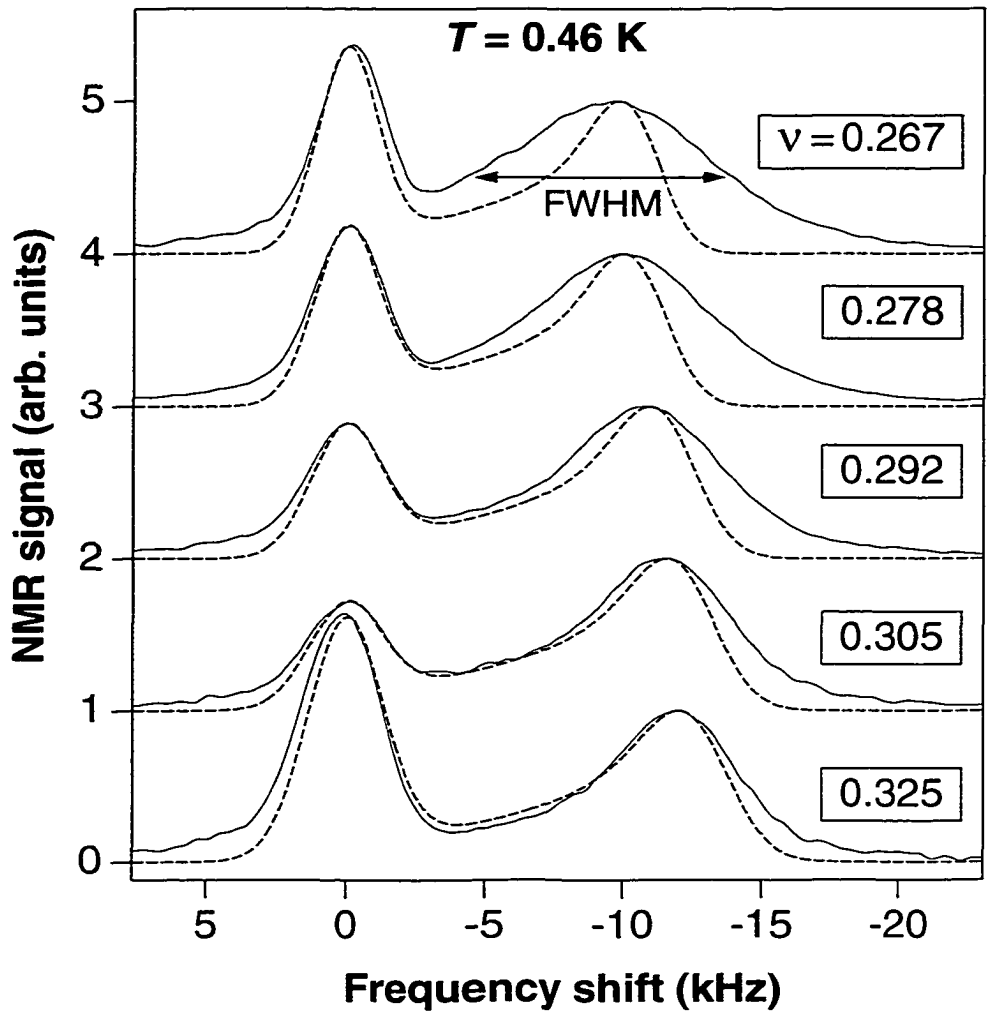


Figure 3.4: $^{71}$Ga OPNMR spectra (solid lines) of sample 10W at $T$=0.46 K, for $0.267 \leq \nu < 1/3$ ($0° \leq \theta < 36.8°$)

in the dipolar broadening (the $^{75}$As nearest-neighbors of the $^{71}$Ga nuclei are at the "magic angle"[69] when $\theta_{10W}$=0°). Furthermore, there is a striking correspondence between the decrease in the linewidth (Fig. 3.5, open symbols) and the increase in $K_S$ (filled symbols) as $\nu \rightarrow 1/3$. This anticorrelation strongly suggests that the behavior in Figs. 1 to 3 is due to electron spin dynamics.

### 3.0.13 Ultraslow Motion

Let us recall the specific assumptions that lead to $I_w^{int}(K_{Sint}, f)=[f/(K_{Sint}-f)]^{1/2}$. Nuclei within the well couple to the spins of the 2DES through the isotropic Fermi contact interaction[22, 33, 55, 56, 43], thus a nucleus at site $\vec{R}'$ experiences a hyperfine magnetic field

$$\vec{B}^e(\vec{R}') = (-16\pi\mu_B/3)\sum_j \vec{S}_j\delta(\vec{r}_j - \vec{R}'), \tag{3.3}$$

where $\mu_B$ is the Bohr magneton, $\vec{S}_j$ is the spin of electron j, the summation is over all of the conduction electrons within the well, and the delta function picks out those electrons that overlap with the nucleus at $\vec{R}'$. The average projection of $\vec{B}^e$ along the applied field $\vec{B}_{tot}$ is then:

$$\begin{aligned}\langle B_z^e(\vec{R}', \nu, T)\rangle = (|^{71}u(0)|^2|\chi(Z')|^2|\phi(X', Y')|^2) \\ \times(\frac{-8\pi\mu_B}{3})\mathcal{P}(\vec{R}', \nu, T)(\frac{n}{w}).\end{aligned} \tag{3.4}$$

Here, the probability density of finding electrons at a $^{71}$Ga site has been factored into a term with the periodicity of the lattice $|^{71}u(0)|^2$ and terms which vary slowly within a unit cell $|\chi(Z')|^2|\phi(X',Y')|^2$[50]. $\mathcal{P}(\vec{R}',\nu,T)$ is the local spin-polarization ($-1<\mathcal{P}<1$) of the electrons at $\vec{R}'$. If we assume that electrons are delocalized along the well, then the time-averaged values of $|\phi|^2$ and $\mathcal{P}$ are spatially homogeneous.

However, the observed broadening of the well line shape beyond the "motionally narrowed" limit implies that the time-averaged value of $|\phi|^2\mathcal{P}$ becomes spatially inhomogeneous as the temperature is lowered. Although the $|\phi(X',Y')|^2$ term could become inhomogeneous if a pinned Wigner crystal were to form, the corresponding

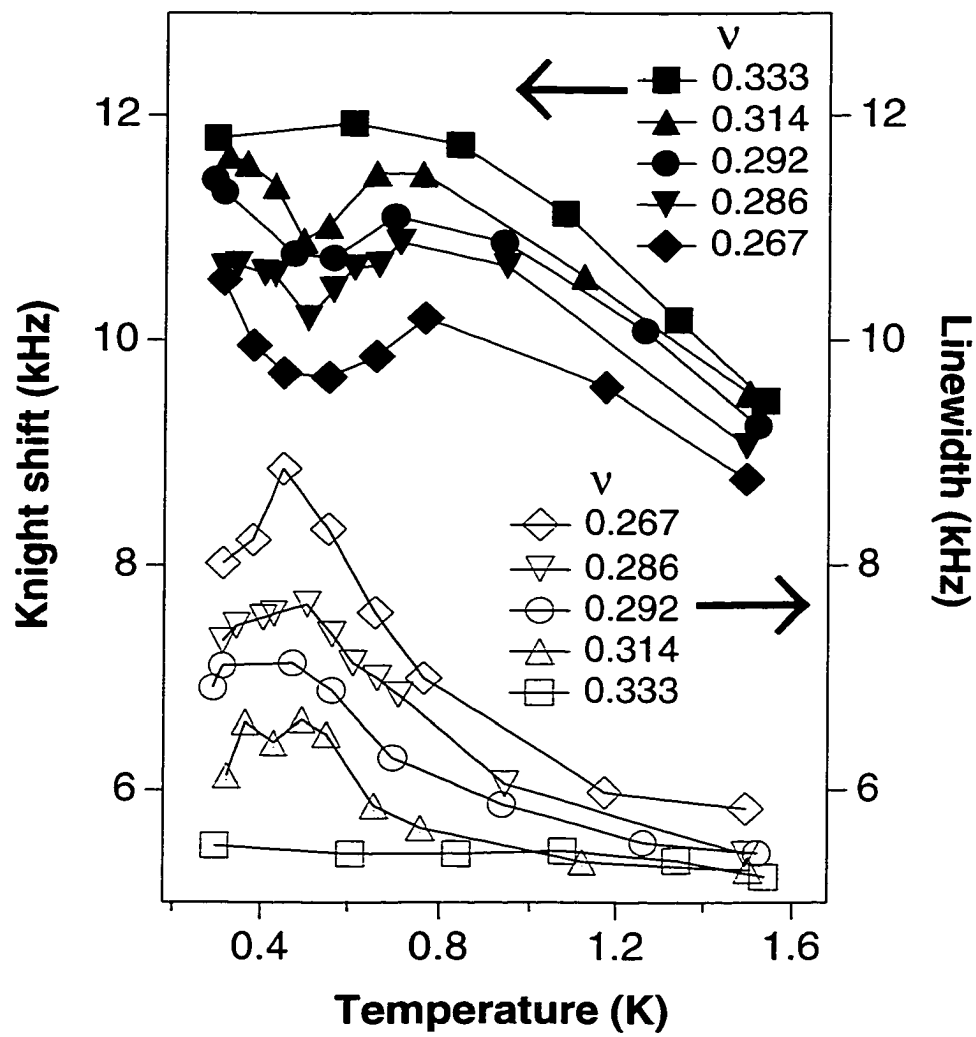


Figure 3.5: The temperature dependence of the Knight shift (filled symbols) and the linewidth (open symbols) for several filling factors $0.267 \leq \nu \leq 1/3$ in sample 10W. Lines are to guide the eye.

increase in the linewidth (by orders of magnitude) and the concomitant drop in the peak intensity are not observed. Furthermore, variations in charge density along the well (for example, arising from fluctuations in the dopant layer) do not appear to explain either the magnitude of the effect or the non-monotonic temperature dependence. In simulations, we found that an unreasonably large FWHM of 35% is required for a gaussian distribution of electron densities along the well to explain the maximum NMR linewidth observed at $\nu$=0.267. In contrast, the Knight shift data show that the total spin polarization drops monotonically below $\nu=\frac{1}{3}$, allowing the local spin polarization $\mathcal{P}(\vec{R}')$ to be spatially inhomogeneous. Thus we conclude that localization of spin-reversed regions is responsible for the behavior shown in Figs.3.3 to 3.5.

The time scale of the spin localization may be inferred by simulating the observed line shapes. In our model, for every point $(x', y')$ along the plane of the well, the local polarization is either "up" ($\mathcal{P}$=1) or "down" ($\mathcal{P}$=-0.15). After every jump time $\tau_J$, the local polarization instantaneously assumes either the "up" or "down" value with probability $p_+$ or (1-$p_+$), respectively. At all times, the ratio of "up" to "down" sites is $p_+/(1-p_+)$. Figure 3.6 shows how the simulated OPNMR spectra depend upon the value of $\tau_J$, for the case $p_+$=0.85. The simulation is in reasonable agreement with the corresponding data from sample 10W. When $\tau_J$ is very fast, all nuclei see the same time-averaged local polarization, equal to the total polarization ($\mathcal{P}_{\text{total}}$=0.828 at $\nu$=0.275 for our assumptions). At the other extreme ($\tau_J \to \infty$), the motion is frozen out, and the single resonance is split into "up" and "down" lines, with areas proportional to $p_+$ and (1-$p_+$), respectively. Even within this simple model, the inhomogeneous breadth of the frozen line shape (due to the quantum confinement) leads to a non-trivial evolution of the spectrum in the intermediate motion regime (for example, a given value of $\tau_J$ might be simultaneously "fast" for nuclei at the

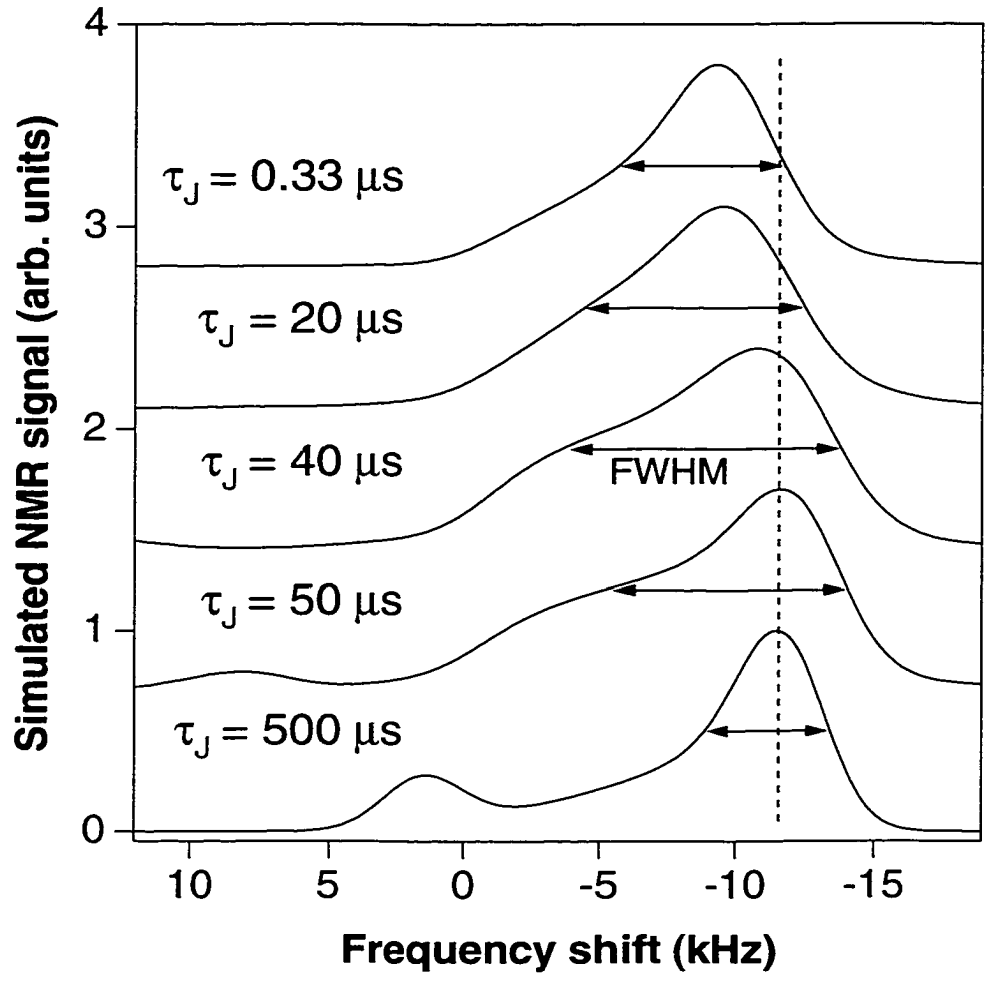


Figure 3.6: Simulated OPNMR spectra using the model described in the text. $K_{S\text{int}}$ is set to 12 kHz for $\mathcal{P}$=1. The barrier is suppressed ($a_b$=0) for clarity.

edge of the well and "slow" for nuclei in the center of the well). In the intermediate motion regime, the FWHM of the "w" peak goes through a maximum when $\tau_J$=40 $\mu$s. Although varying the parameters $p_+$ and $K_{S\text{int}}$ (over the range relevant for samples 10W and 40W) does affect the extreme value of the FWHM, the characteristic $\tau_J$ remains ~40 $\mu$s.

Based upon this simple model, the peaks in the FWHM at $T_{loc}$ ≈0.5 K (Fig.3.5) reflect the localization of reversed spins, such that they fail to cover the sample

uniformly over $\sim 40\,\mu$s. The self-similar curves in Fig.3.5 suggest that $T_{loc}$ is not a strong function of the filling factor (or the density of reversed spins) for $\nu<1/3$. Note also that below 0.5 K, the measured $K_S(\nu<\frac{1}{3})$ increases toward $K_S(\nu=\frac{1}{3})$, as seen in the model. However, even down to $T$=0.3 K, the spectra do not appear to match the frozen limit of our simulation. Suprisingly, as $\nu$ is varied below 1/3, the trends in the $K_S$ and FWHM data (Fig. 3) continue smoothly through $\nu$=2/7 without interruption, even though high-field magnetotransport measurements on samples taken from the same wafer as 10W show much more structure, with well-developed minima in $\rho_{xx}$ at $\nu=\frac{1}{3}$, $\frac{2}{5}$, $\frac{2}{7}$, and $\frac{1}{5}$ at $T=0.3$ K[40, 70].

Additional measurements of the linewidth for $\nu>1/3$ in sample 10W are consistent with the above picture. Measurements in sample 40W for $\nu\leq 1/3$ are also in qualitative agreement, with one important quantitative difference: $T_{loc}$ appears to be shifted lower, so that only the high temperature side of the peak in the FWHM is observed down to $T\approx$0.3 K. There is a similar sample variation in the saturation temperature of $\mathcal{P}(\nu=\frac{1}{3})$, with $T^{sat}_{10W}\approx$0.77 K and $T^{sat}_{40W}\approx$0.46 K. The observed spectra contain more information than our simple simulation has revealed. A more sophisticated model might include: (i) a detailed structure for the reversed spin regions present below $\nu$=1/3, (ii) the 2D dynamics of these reversed spins, and (iii) the effects of thermally excited spin flips, because $T_{sat}$ is not that much greater than the $T_{loc}$. We will return to this topic in our later discussion of new $\nu$=1 data.

### 3.0.14 Tiny Spin Flips

In order to use $\mathcal{P}(\nu)$ to measure the spin flip associated with a quasiparticle, the quasiparticles must be delocalized (moving fast on the NMR time scale), such that $\mathcal{P}(\nu)$ is a global quantity (doesnt vary from one location to another). From the

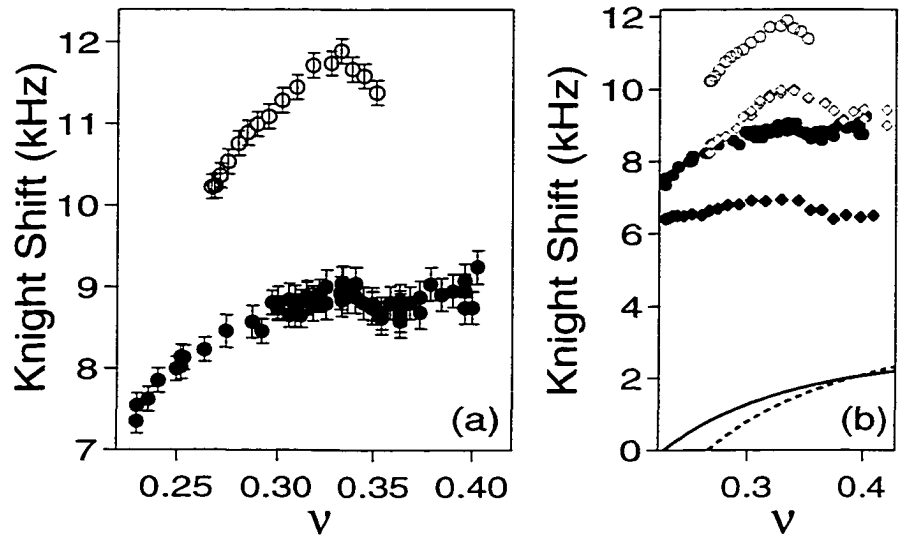


Figure 3.7: Dependence of $K_S$ on filling factor at fixed temperature. Open circles: sample 10W at $T$=0.77 K, filled circles: sample 40W at $T$=0.46 K; open and filled diamonds: 10W and 40W at $T$=1.5 K, respectively. Solid and dashed lines are described in the text.

above discussion, we see that the quasiparticles tend to localize at low temperatures at filling factors away from $\nu$=1/3. Hence, in order to avoid the complication of a spatially inhomogeneous $\langle S_z \rangle$, the data presented in Fig. 3.7 and 3.8 were taken at temperatures that were low enough to saturate $K_S(T)$ at $\nu=\frac{1}{3}$, and hopefully just high enough so that the quasiparticles were still delocalized. The linewidth, is of course, always motionally narrowed right at $\nu$=1/3, where there are no quasiparticles. The Knight shift was then measured at fixed temperature as a function of $\nu$ (by varying the sample tilt angle), with $B_{\rm tot}$=12 T. Fig. 3.7(a) shows $K_S(\nu)$ near $\nu=\frac{1}{3}$ for sample 10W at $T$=0.77 K, and for sample 40W at $T$=0.46 K.

The data in Fig. 3.7(a) show that $K_S(\nu)$ drops on either side of $\nu=\frac{1}{3}$, a result that is reminiscent of earlier measurements near $\nu$=1[22]. The $K_S(\nu\sim\frac{1}{3})$ feature is distinctly "sharper" for sample 10W as opposed to sample 40W. This difference between the samples is not an artifact of the temperatures plotted, as Fig. 3.7(b)

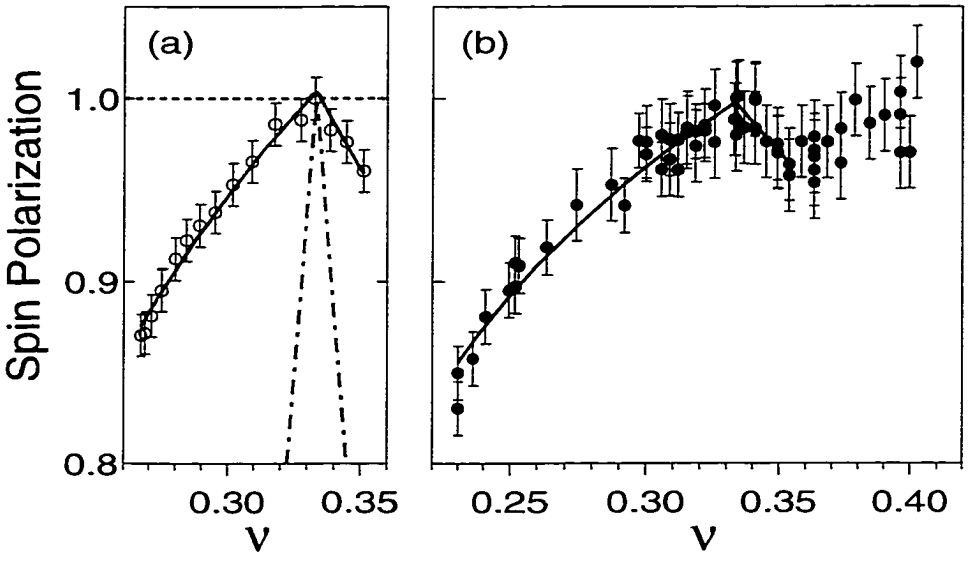


Figure 3.8: Dependence of $\mathcal{P}$ on filling factor at fixed temperature. (a) 10W at $T$=0.77 K (open circles); Eq. (1) with $\nu_o=\frac{1}{3}$ for: $\tilde{\mathcal{A}}=\tilde{\mathcal{S}}=0$ (dashed line), $\tilde{\mathcal{A}}$=0.085 and $\tilde{\mathcal{S}}$=0.15 (solid line), and $\tilde{\mathcal{A}}=\tilde{\mathcal{S}}=1$ (dash-dotted line). (b) 40W at $T$=0.46 K (filled circles); Eq. (1) with $\nu_o=\frac{1}{3}$, $\tilde{\mathcal{A}}$=0.053 and $\tilde{\mathcal{S}}$=0.10 (solid line).

shows that the distinction is already present by $T$=1.5 K. In order to measure $K_S(\nu)$ this accurately, we took into account the *extrinsic* tilt-angle dependence of the barrier frequency (Fig. 3.7(b), solid and dashed curves) caused by a paramagnetic rotation stage.

The $K_S(\nu)$ data shown in Fig. 3.7(a) are converted to the corresponding electron spin polarization $\mathcal{P}(\nu) \equiv \frac{K_{S\mathrm{int}}(\nu)}{K_{S\mathrm{int}}(\nu=1/3)}$, and are plotted in Fig. 3.8. The polarization of both samples decreases as $\nu$ is varied away from $\frac{1}{3}$, *despite the presence of the 12 T field!* Perhaps even more remarkably, $\mathcal{P}(\nu)$ decreases monotonically as $\nu$ is lowered below $\frac{1}{3}$ over the observed range ($\frac{\delta\nu}{1/3} \sim -30\%$). This strongly suggests that the charged quasiparticles and quasiholes of the $\nu=\frac{1}{3}$ ground state involve electron spin flips.

The disappearance of "motional-narrowing" at low temperatures is further evi-

dence for the presence of reversed spins below $\nu=\frac{1}{3}$. As we saw before, the high temperature spectra are "motionally narrowed", while Fig. 3.5 shows that the well lineshape broadens dramatically at low temperatures below $\nu=\frac{1}{3}$, indicating that the time-averaged $\langle S_z \rangle$ is no longer spatially homogeneous. The inhomogeneity *requires* the existence of spin-reversed regions, that become localized over the NMR time scale as the temperature is lowered below $\sim$0.5 K ($\sim$0.3 K) for sample 10W (40W)[56].

To quantify the rate of depolarization in Fig. 3.8, we extend a simple model previously used near $\nu$=1[22]. Our model parametrizes the effect of interactions in the neighborhood of a ferromagnetic filling factor $\nu_o<1$. We assume that adding a quasiparticle (or quasihole) to the ground state causes $\tilde{\mathcal{S}}$ (or $\tilde{\mathcal{A}}$) electron spins to flip. Within this model, the electron spin polarization is:

$$\mathcal{P}(\nu) = 1 + 2\Big(\frac{1}{\nu} - \frac{1}{\nu_o}\Big)\Big(\tilde{\mathcal{S}}\,\Theta(\nu-\nu_o) - \tilde{\mathcal{A}}\,\Theta(\nu_o-\nu)\Big), \tag{3.5}$$

where $\Theta(x) \equiv \{\,1,\ x\geq 0;$ and $0,\ x<0\,\}$. Using Eq. (3.5) to fit the data near $\nu_o=\frac{1}{3}$ (solid lines), we find:

10W : $\quad \tilde{\mathcal{A}} = 0.085 \pm 0.005, \quad \tilde{\mathcal{S}} = 0.15 \pm 0.04$

40W : $\quad \tilde{\mathcal{A}} = 0.053 \pm 0.008, \quad \tilde{\mathcal{S}} = 0.10 \pm 0.03.$

For comparison, the earliest theory[9, 3] of the $\nu=\frac{1}{3}$ ground state assumed spin-polarized quasiparticles and quasiholes, i.e., $\tilde{\mathcal{S}}=\tilde{\mathcal{A}}=0$ (Fig. 3.8, dashed line). Subsequent calculations [4] considered the possibility of spin-reversed quasiparticles and quasiholes, i.e., $\tilde{\mathcal{S}}=\tilde{\mathcal{A}}=1$ (Fig. 3.8, dash-dotted line). However, both the early calculations and the more recent studies of skyrmion excitations near $\nu=\frac{1}{3}$[71, 72] suggest $\tilde{\mathcal{S}}=\tilde{\mathcal{A}}=0$ for strong magnetic fields. On the other hand, our small, *non-zero* values are within the bounds set by transport measurements at ambient[73] and high[41] pressures.

A much more difficult feature to understand is the fact that our measured values are fractional ($\tilde{\mathcal{S}} \sim \tilde{\mathcal{A}} \sim 0.1$), since the magnetic field should make $\langle S_z \rangle$ a good quan-

tum number for the N particle system[4]. Of course, our experiment does not have the resolution to see the effect of adding a single quasiparticle to the $\nu=\frac{1}{3}$ ground state, thus these values for $\tilde{\mathcal{S}}$ and $\tilde{\mathcal{A}}$ are the *average* numbers of flipped spins per quasiparticle and quasihole. Nevertheless, Eq. (3.5), which assumes that all quasiholes (or quasiparticles) behave in exactly the same way, does a remarkably good job fitting our data over the range ($0.23<\nu<0.36$). This model is expected to break down outside the "dilute" quasiparticle limit (i.e., when $\nu$ gets "too far" from $\frac{1}{3}$), since $\tilde{\mathcal{S}}$ and $\tilde{\mathcal{A}}$ are independent of $\nu$. Note that fits to the earlier $\nu$=1 data considered dilute quasiparticle limits of $\pm$10% around $\nu$=1, but here our fit works over a wider range, perhaps due to the smaller size of the quasiparticle. Once again, surprisingly, the above fit passes through $\nu=\frac{2}{7}$ without modification.

The possible explanations of these values ($\tilde{\mathcal{S}}\sim\tilde{\mathcal{A}}\sim 0.1$) are constrained by many different aspects of the data. For example, the values of $\tilde{\mathcal{S}}$ and $\tilde{\mathcal{A}}$ do not appear to change up to $T$=1.5 K. Furthermore, the motional narrowing of the NMR line requires that the time-averaged electron spin polarization is spatially uniform for all $\nu$.

### 3.0.15 RF Heating

When we first started doing our experiments, we had trouble reproducing spectra at very low temperatures. We were able to track down this problem to a bad attentuator that was being used to attentuate the RF signal needed to flip the nuclear spins. It turned out that this attenuation was fluctuating by a factor of 2 or 3 during out experiments. Ordinarily, this should not have been a problem, since the attentuator would remain stable for a long time before it switched states. However, it turned out that the electron spin temperature also depended strongly on the amount of rf

power that was used to tip the nuclear NMR spins to generate a signal. These two effects were conspiring to frustrate our attempts to measure reproducible sprectra. We eventually located the flaky attentuator, but still didn't suspect that the electron spins were being heated by our strong rf pulses. We felt a sense of relief when we finally started measuring data that did not vary from hour to hour, however, we were still suspicious of our initial Knight shift data at $\nu$=1/3, since it would increase up to a certain temperature $T$ ~500mK, but then continue to drop as we lowered the temperature below that. We knew that the $\nu$=1/3 state was predicted to be ferromagnetic, and so we expected the Knight shift to continue rising till our lowest temperatures. Eventually, we varied the last thing on our list, the rf pulse power, and found that the Knight was very sensitive to this quantity at temperatures below $T$ ~500mK, and that it was therefore necessary to use low pulse powers in order to make equilibrium measurements. Shown in Fig.3.9 is a situation where we use a lot of rf power in (a) and less in (b).

This effect is very interesting, since we can now use the equilibrium Knight shift as a thermometer, to measure the increase of the electron spin temperature above the lattice temperature when rf pulses are used to drive the system out of equilibrium.

### 3.0.16 Electron Spin-Lattice Relaxation Time

All of the results described thus far were acquired by applying a weak rf tipping pulse long after optical pumping to probe the equilibrium properties of the 2DES. Non-equilibrium properties of the electron spin system can be studied by varying these parameters at low temperatures, with a number of remarkable results at $\nu$=1/3.

The rf tipping pulse for the NMR experiment is produced by a coil wrapped around the sample (Fig. 3.10C, inset), which generates a linearly polarized (perpendicular to

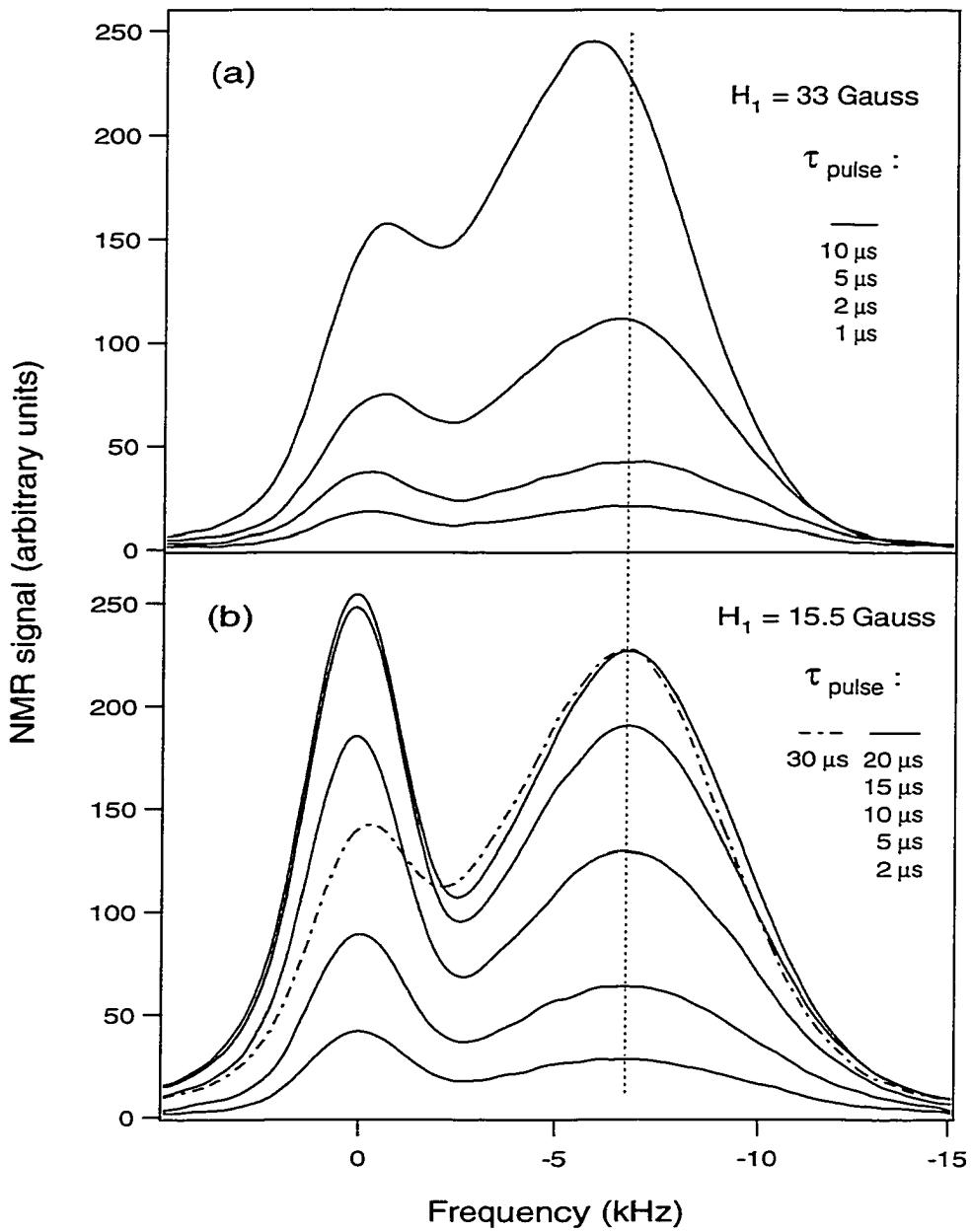


Figure 3.9: $^{71}$Ga OPNMR spectra of sample 40W, acquired at $\nu = 0.230$ ($\theta = 0$) with a single rf tipping pulse of amplitude (a) $H_1 = 33$ Gauss and (b) $H_1 = 15.5$ Gauss at $T = 0.45$ K. The duration of the pulse $\tau_{\text{pulse}}$ is shown for each spectrum. Note that the spectra with similar values of tipping angle $\theta = \frac{1}{2}\gamma H_1 \tau_{\text{pulse}}$ have very different Knight shift in cases (a) and (b). A vertical dashed line marks the frequency of the well peak in the limit of no rf heating.

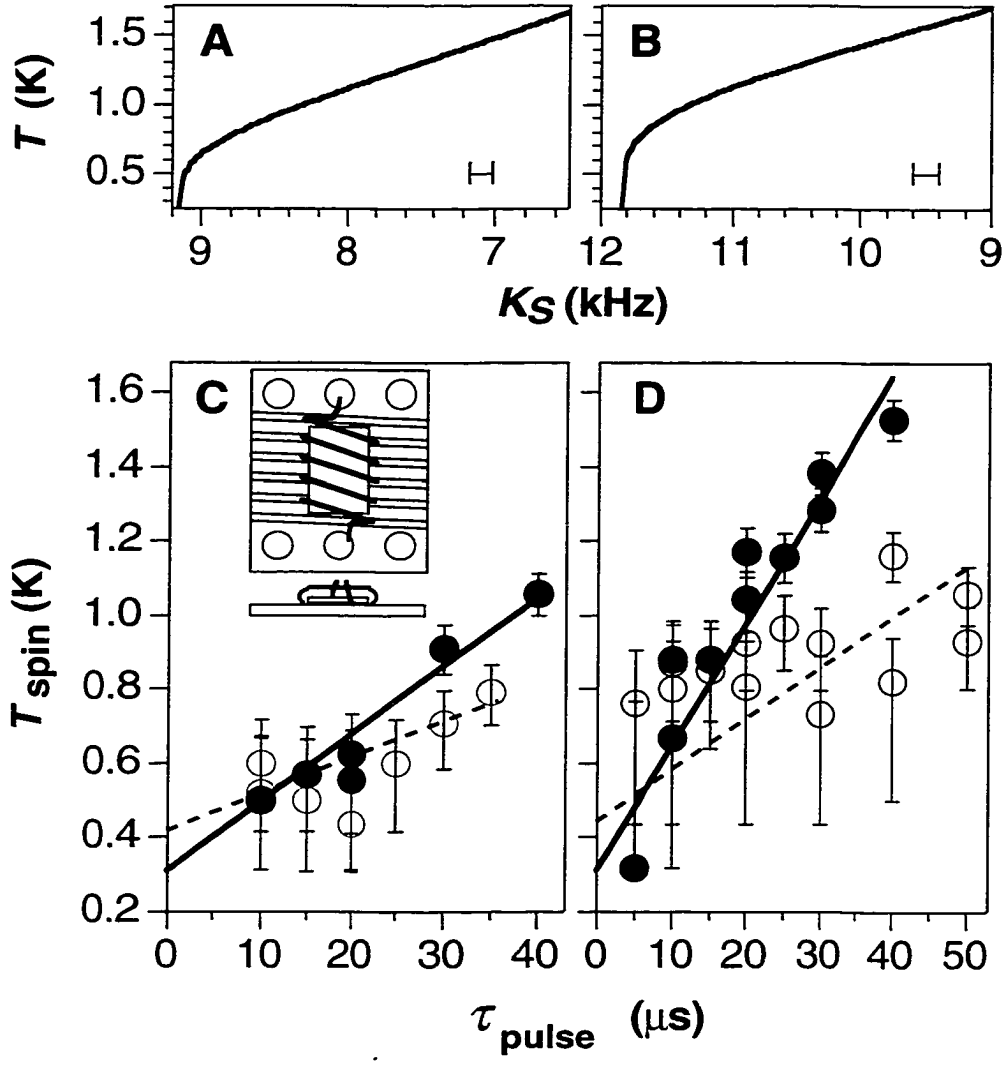


Figure 3.10: Top: T($K_S$) calibration curves based on the equilibrium $K_S$(T) data for (**A**) sample 40W and (**B**) sample 10W. Error bars for $K_S$ are shown. Bottom: The dependence of the effective spin temperature on the rf pulse length ($H_1$~7 Gauss) for (**C**) sample 40W and (**D**) sample 10W. The intercept of the straight line fit was constrained to be the lattice temperature: $T = 0.31\,K$ (filled circles 10W and 40W), $T = 0.42\,K$ (open circles 40W), and $T = 0.44\,K$ (open circles 10W). The inset shows the top (along $z'$) and the front (along the rotation axis) views of the grooved sapphire platform holding a sample in a 5-turn rf coil.

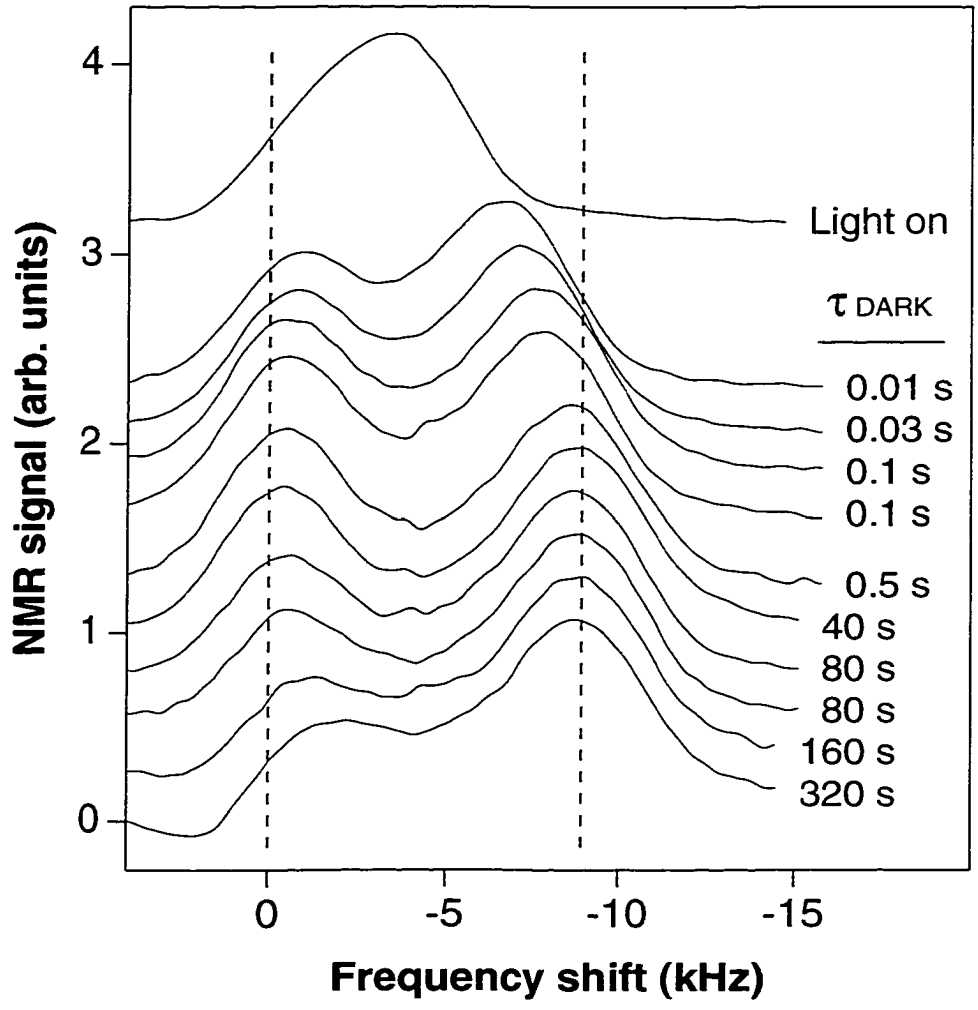


Figure 3.11: Spectra acquired using sample 40W at $T_{bath}$=0.45 K, which show the evolution of the line shape as a function of dark time $\tau_D$.

$\vec{z'}$) magnetic field of amplitude $2\times H_1$ at $f_o$=155.93 MHz. The equilibrium value of $K_S$(T) is independent of the tipping pulse parameters for weak $H_1$ (that is, $H_1 \approx$ 5 Gauss, $\tau_{\text{pulse}}$=20 $\mu$s). However, if stronger pulses are used for T<0.5 K, the measured $K_S$ drops sharply below the equilibrium value, even though the lattice temperature is unaffected by the pulses. The equilibrium measurements[55] of $K_S$(T) (Fig. 3.10, A and B), can be used to convert the measured Knight shift into an effective electron

spin temperature $T_{\rm spin}$; $T_{\rm spin}$ rises linearly above the lattice temperature T as the duration of the tipping pulse $\tau_{\rm pulse}$ increases, for $H_1 \sim 7$ G (Fig. 3.10, C and D). The increase of $T_{\rm spin}$ drops off sharply with increasing lattice temperature and is not observable for T>0.5 K. Furthermore, the apparent heating depends strongly on the alternating field strength and scales as $H_1^\eta$ ($2<\eta<5$), which rules out nuclear spins as the heat source, because their tipping angle scales with $H_1 \times \tau_{\rm pulse}$. Another possible mechanism, ohmic heating by eddy currents, appears inconsistent with the strong $T$ and $H_1$ dependence of the effect. Rather, these data provide evidence for a direct coupling between the rf pulse and the spins in the 2DES. The mechanism for this interaction in a clean system is not known, because the applied rf photon energy is well below the electron spin resonance at ~74 GHz. Impurities in the bulk or edge states may be playing a role in this process.

The non-equilibrium spectra remain motionally narrowed, and appear indistinguishable from the corresponding equilibrium spectra measured at a higher lattice temperature. Thus, the electron spin system achieves internal equilibrium prior to our measurement, justifying our use of $T_{\rm spin}$[43]. However, our measurement also shows that $T_{\rm spin}$ remains greater than T long after the rf pulse is turned off, which implies that the electron spin-lattice relaxation time $\tau_{1s} > 100\,\mu$s, for T<0.5 K at $\nu=\frac{1}{3}$.

The evolution of the spectra as the dark time $\tau_D$ is increased provides an upper bound on $\tau_{1s}$ (Fig. 3.11). The measured spectra are essentially independent of $\tau_D$ after the first 0.5 s, consistent with the equilibration time of the the laser-heated sample with the helium bath at 0.45 K. Combining these results, we find $100\,\mu s<\tau_{1s}<500$ ms, for $T$ <0.5 K at $\nu$=1/3. While this value of $\tau_{1s}$ is at least a factor of 1000 longer than recent measurements of the transverse relaxation time $\tau_2^*$ in bulk GaAs[74], it is consistent with a previous theoretical prediction[75] which assumed conditions rather

similar to our experiment.

Thus, we have shown that the $^{71}$Ga OPNMR spectra can be used to reveal the local, time-averaged value of the electron spin magnetization, $\langle S_z(\vec{R})\rangle$, which can be quite different from the global average of the spin polarization. As the temperature is lowered, the evolution of the NMR spectra from the "motionally narrowed" limit to the "frozen" limit is consistent with the localization of quasiparticles, which are present only when $\nu \neq 1/3$. At temperatures where the quasiparticles are still delocalized, we can measure the amount of spin flip ($\sim$0.1) associated with each quasiparticle, which turns out to be quite small. Finally, we have stumbled upon a technique that can be used to measure the electron spin-lattice relaxation time in GaAs under certain conditions (100 $\mu$s$<\tau_{1s}<$ 500 ms, for $T$ <0.5 K at $\nu$=1/3).

# Chapter 4

# $\nu$=1: Freezing out the skyrmion liquid

In this chapter, we report optically pumped nuclear magnetic resonance (OPNMR) measurements of the Knight Shift $K_S(\nu, T)$ and full-width half-maximum linewidth $\Gamma_w(\nu, T)$ of $^{71}$Ga nuclei in an electron-doped multiple quantum well (MQW) sample. These measurements provide the first evidence for the localization of skyrmions near $\nu = 1$ as $T \to 0$. In this limit, the apparent skyrmion "shape" may be compared to theoretical expectations. The measurements near $\nu$=1 described below are some of the last measurements performed during the course of this thesis. The MQW sample used in this work, PRL95, was previously studied at higher temperatures[22, 33].

### 4.0.17 The Tilted Plateau

Fig. 4.1 shows the $K_S(\nu)$ and the $\Gamma_w(\nu)$ (FWHM) of the 'W" resonance near $\nu = 1$, for three different temperatures. All spectra at $\nu$=1 are well-described by the same two-parameter fit that was previously used for all spectra at $\nu$=$\frac{1}{3}$ (eqn. 2.1). On

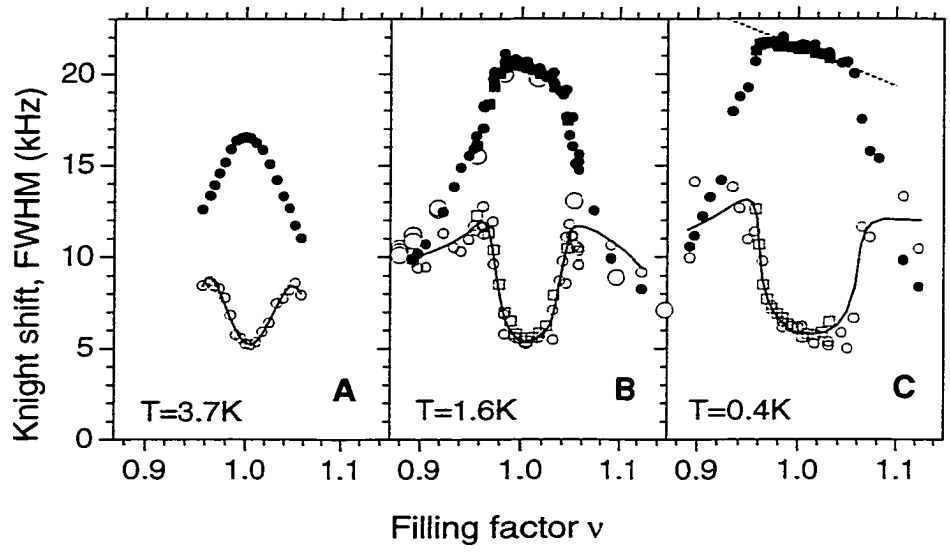


Figure 4.1: The filling factor dependence of both $K_S$ (solid symbols) and $\Gamma_w$ (small open symbols) at (**A**) $T$=3.7 K, (**B**) $T$=1.6 K, and (**C**) $T$=0.4 K. Here, $\Gamma_w$ is the full width at half maximum (FWHM) for the "W" resonance, and $0° \leq \theta \leq 37°$. Earlier $K_S(\nu)$ measurements in the same sample [(**B**) large open symbols] are consistent with these results. Solid lines are to guide the eye, and the dashed line is described in the text.

the other hand, for $\nu \neq 1$ and low T, the width of the well resonance (Fig. 4.1A, 4.1B, 4.1C) can also be much broader than this same fit. At T=3.7 K, there is a sharp peak in $K_S(\nu)$ (Fig. 4.1(A)). We infer the sample density $n$ from this feature assuming that the maximum $K_S(\nu)$ occurs at $\nu = 1$, obtaining $n = 1.52 \times 10^{11} cm^{-2}$, a value consistent with transport characterization of the sample. The $\nu(\theta)$ dependence is thus completely determined, and used throughout this chapter ($0° < \theta < 37°$ in Fig. 4.1).

As the temperature is lowered (Fig. 4.1A-4.1C), the sharp peak in $K_S(\nu)$ evolves into a "tilted plateau". Figure 4.1B also contains the $K_S(\nu)$ data points reported previously[22]. While the new data are consistent with the earlier measurements, probing $K_S(\nu)$ on this finer scale reveals a small region on both sides of $\nu$=1 where $K_S(\nu) \approx K_S(\nu=1)/\nu$ (dashed line in Fig. 4.1C). This tilted plateau is incompatible

with the expression for $K_S(\nu)$ derived previously[22], which had assumed *delocalized quasiparticles*[76]. The existence of the tilted plateau is a natural consequence of the localization of the quasiparticles along the plane of the quantum well, such that the nuclei responsible for the well resonance see fully polarized electrons ($\mathcal{P}$=1), as if $\nu$=1 "locally", even though $\nu\neq$1 "globally". More precisely, for nuclei at $\mathbf{R_i}$=($X'$, $Y'$, $Z'$=0) in the center of the quantum well, the local $K_{S\mathrm{int}}(\mathbf{R_i})$ is directly proportional to the $z$-component of the local electron spin magnetization density, $M_z(\mathbf{R_i})$[43], which is in turn proportional to the product of the electron number density and the spin polarization, i.e., $M_z(\mathbf{R_i})\propto |\phi(\mathbf{R_i})|^2\ \mathcal{P}(\mathbf{R_i})$[56]. If the quasiholes (or quasiparticles) introduced into the system by going to $\nu = 1-\epsilon$ (or $\nu = 1+\epsilon$) are localized, then, in order to keep the total number of electrons fixed, $|\phi(\mathbf{R_i})|^2$ *must* increase (or decrease) far from these charged excitations, which produces the observed tilt in the plateau near $\nu$=1. This is just the same effect as the rise (or fall) of the water level in a pool induced by placing solid dipsticks (or hollow capillary tubes) into it to create localized density minima (or maxima), which correspond to quasiholes (or quasiparticles). In this analogy, changing the filling factor by adjusting $B_{\mathrm{tot}}\cos\theta$ varies the number of dipsticks or capillary tubes in the pool and the Knight shift is given by the water level. Clearly, the fact that NMR is a local probe has become important.

### 4.0.18 Localization of Quasiparticles

Taking different slices through the ($\nu$, $T$) plane provides additional insights. Figure 4.2 shows $K_S(T)$ and $\Gamma_w(T)$ for several filling factors near $\nu$=1. For $\nu\neq$1, lowering the temperature causes $\Gamma_w(T)$ first to increase and then to drop, in stark contrast to the temperature independence of the well linewidth at $\nu$=1. The non-monotonic

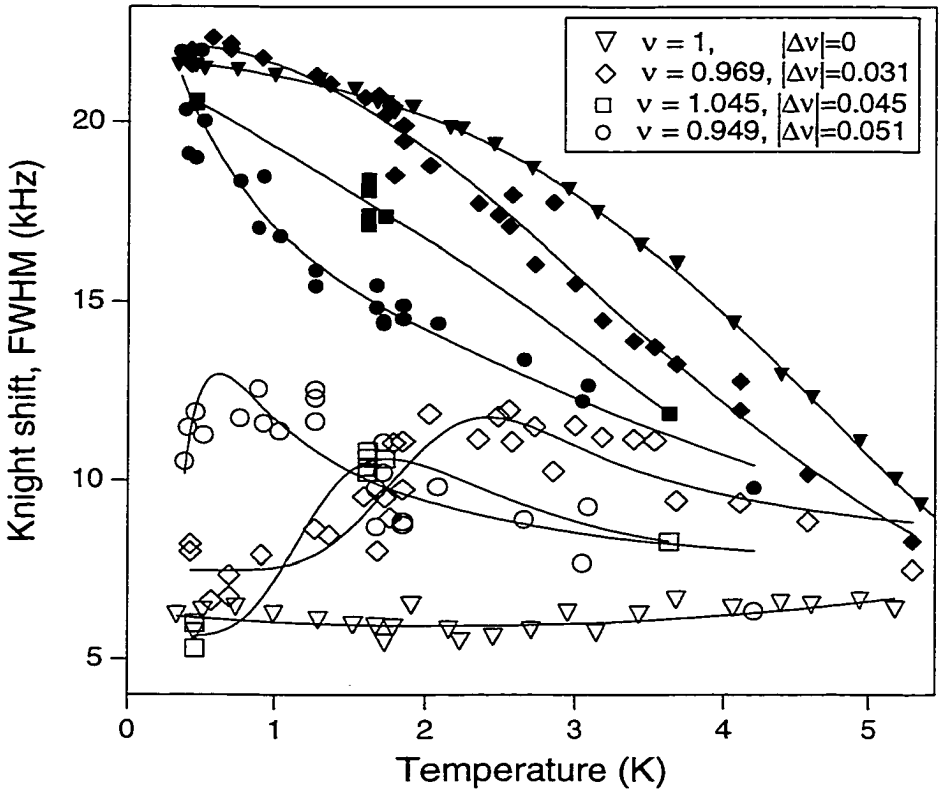


Figure 4.2: The temperature dependence of the Knight shift (filled symbols) and the linewidth (open symbols) for several filling factors $0.949 \leq \nu \leq 1.045$. Lines through $K_S(T)$ are to guide the eye. Curves through $\Gamma_w(T)$ are fits described in the text.

temperature dependence (Figure 4.2) is consistent with the evolution of the "W" resonance from motionally-narrowed to frozen as the temperature is lowered. Qualitatively similar trends were uncovered in earlier measurements at $\nu < 1/3$[56]. Both cases are rather unusual examples of motional narrowing phenomena in NMR, since the nuclei are fixed in the lattice at such low $T$. Instead, the motion is that of delocalized spin-reversed quasiparticles, that results in fluctuations of the local hyperfine field $\delta B_z^e(\mathbf{R_i})$ at each nuclear site $\mathbf{R_i}$. The shape of the resonance is sensitive to $\Theta(\mathbf{R_i}) \equiv \tau(\mathbf{R_i})\delta B_z^e(\mathbf{R_i})^i\gamma$, where $\tau(\mathbf{R_i})$ is the characteristic time scale of the fluctuations, and $^i\gamma$ is the nuclear gyromagnetic ratio[43]. As $T$ is lowered, the "W" resonance goes from the "motionally-narrowed limit" (at high $T$, $\Theta(\mathbf{R_i}) << 1$) to the "intermediate

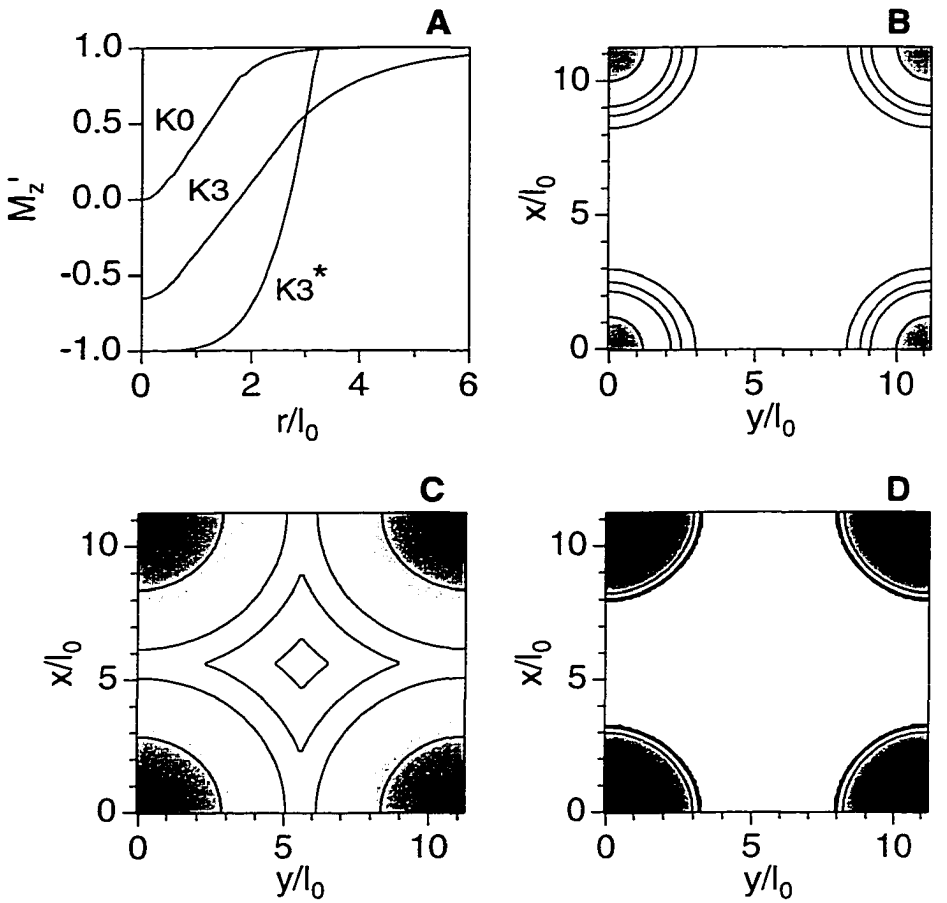


Figure 4.3: (**A**) Expected radial dependence (in units of the magnetic length $l_o$) of $M_z'(r)$, for the K0, K3, and K3* skyrmions described in the text. For $|\delta\nu|$=0.05, gray scale images of $M_z^{Sim}(\mathbf{R_i})$ (Black=−1; White=+1) are shown within the unit cell of a square lattice of either (**B**) K0, (**C**) K3, or (**D**) K3* skyrmions. Also shown (in **B-D**) are black contour lines at $M_z^{Sim}$= 0.5, 0.9, 0.95, and 0.98.

limit" (at $T$ near $T_{max}$, where $\Gamma_w(T_{max})$=$\Gamma_w^{max}$, $\Theta(\mathbf{R_i}) \sim 1$) and then to the "frozen limit" (at low $T$, $\Theta(\mathbf{R_i}) >> 1$). Figures 4.1 and 4.2 show that all three limits are experimentally accessible near $\nu$=1.

The frozen limit spectrum can provide information about the shape of individual quasiparticles and their spatial arrangement along the plane of the quantum well, through its dependence on $M_z(\mathbf{R_i})$. In this limit, Equation (2.1) should be replaced by a more general expression for the OPNMR spectra:

$$I(f) = a_b\, g(f) + \sum_{\mathbf{R_i}}^{Area} \int_0^{K_{Sint}(\mathbf{R_i})} df' g(f-f')\, I_w^{int}(K_{Sint}(\mathbf{R_i}), f') \quad (4.1)$$

where the sum runs over all nuclei in the center of the quantum well.

Several theoretical approaches have been used to calculate $M_z(\mathbf{R_i})$ for a *single* skyrmion excitation of the $\nu = 1$ ground state, which is a charged quasiparticle carrying "$K$" reversed spins. Figure 4.3A shows the typical radial dependence of the dimensionless $M_z'(r)$ expected[26, 27] for skyrmions with $K$=0 ("K0") and $K$=3 ("K3"). The K0 skyrmion corresponds to the ordinary Laughlin quasiparticle, while both theory and experiment suggest that the K3 skyrmion is energetically preferred for typical experimental conditions. Also shown in Fig. 4.3A is an ad hoc hybrid between the two ("K3*"), that has both the tail of K0 and the three reversed spins of K3.

As $|\delta\nu|$ increases, it becomes much more difficult to calculate $M_z'(\mathbf{R_i})$, since the average distance between the quasiparticles approaches their size. As a first approximation to the actual function, we simply use $M_z^{Sim}(\mathbf{R_i})$≡Min[$M_z'(|\mathbf{R_i}-\mathbf{r_1}|)$, $M_z'(|\mathbf{R_i}-\mathbf{r_2}|)$, ..., $M_z'(|\mathbf{R_i}-\mathbf{r_N}|)$], where N skyrmions are localized at positions ($\mathbf{r_j}$), and $M_z'(r)$ is given by the *isolated* skyrmion calculations (see Fig. 4.3A). Figure 4.3B-4.3D are grey scale images of $M_z^{Sim}(\mathbf{R_i})$ within the unit cell of a square skyrmion lattice at $|\delta\nu| = 0.05$, for the three skyrmions shown in Fig. 4.3A: K0 (B), K3 (C), and K3* (D). Thus, through $M_z^{Sim}(\mathbf{R_i})$, the frozen limit spectrum can provide information about the shape of individual quasiparticles and their spatial arrangement along the plane of the quantum well.

We may now simulate the frozen limit OPNMR spectrum at $\nu$=1 + $\delta\nu$, by using $K_{Sint}(\mathbf{R_i},\delta\nu)$= $(\frac{K_{Sint}^{\nu=1}(T\to 0)}{1+\delta\nu})$ $M_z^{Sim}(\mathbf{R_i},|\delta\nu|)$ in Eqn. (4.1). Figure 4.4 shows [$K_S^{Sim}(\nu)$, $\Gamma_w^{Sim}(\nu)$] extracted from these simulations, which may be quantitatively compared to the low temperature data of Fig. 4.1C. Each curve corresponds to a square lattice

of skyrmions with a particular shape $M_z(r)$ (i.e., both conventional K0, K1, K2, K3 and ad hoc K3* skyrmions). In this model, both the K0 and the K3* skyrmions are in good agreement with the data on the plateau (Fig. 4.4A and 4.4B), while the other conventional skyrmions are not. This conclusion is not very sensitive to either the skyrmion lattice type (e.g., triangular, face-centered rectangular) or to weak disorder in the skyrmion locations, over the range of the observed plateau (i.e., $|\delta\nu| \leq 0.05$). As Figures 4.3B and 4.3D show, the existence of the tilted plateau indicates that $M_z^{Sim}(\mathbf{R_i})$ needs to be $\sim 1$ over a large fraction of the area between the quasiparticles. In principle, this condition could also be met by conventional K3 skyrmions, if, instead of forming a lattice, the quasiparticles are localized in skyrmion-rich regions separated by skyrmion-free regions. For example, at $|\delta\nu| = 0.05$, localized 1D "stripes" of K3 skyrmions could be consistent with the data, provided that the inter-skyrmion spacing along the stripe is $\sim 2l_o$, and the inter-stripe spacing is $\sim 60l_o$. However, the large Coulomb energy cost of this arrangement would seem to make such an extreme anisotropy unlikely, and so we limit our consideration to a square lattice of either K0 or K3* skyrmions. Of course, either localized state must be consistent with the earlier measurements of $\mathcal{P}(\nu)$ near $\nu$=1[22, 77, 30, 31], which provided evidence for *delocalized* $K \approx 3$ skyrmions at higher temperatures.

### 4.0.19 Two Different Scenarios

The K0 case is qualitatively consistent with the recent suggestion that strong pinning of individual, conventional K3 skyrmions might convert them into K0 quasiparticles as $T \rightarrow 0$[78]. However, the $|\delta\nu|$-dependence of $\Gamma_w(T)$ (Fig. 4.2) appears to be inconsistent with this scenario, if we assume a distribution in the strength of the pinning centers. In this case, as $\delta\nu$ increases, we would expect the localization

of quasiparticles to "start" at the same temperature, but "finish" at lower and lower temperatures. However, Fig. 4.2 shows distinctly different behavior, since the whole $\Gamma_w(T)$ peak appears to shift to lower T as $\delta\nu$ increases. For example, at $T \approx 1.5K$, depending upon the quasiparticle density, all skyrmions can appear to be either localized (at $|\delta\nu| = 0.031$) or delocalized (at $|\delta\nu| = 0.051$). The localization of K3* skyrmions does not require a strong pinning mechanism, so we consider it further.

The sensitivity of the data (Figs. 4.1 and 4.2) to $|\delta\nu|$ suggests that skyrmion delocalization is a collective phenomenon. However, the observed $|\delta\nu|$-dependence appears to rule out an obvious candidate mechanism, namely the "melting" of a pinned skyrmion crystal, since the classical melting temperature should increase as the crystal density (and the bond energy) increases. Instead, the data appear to be qualitatively consistent with the "depinning" of a skyrmion crystal, since the soft (stiff) bonds of the crystal at low (high) $|\delta\nu|$ may easily (not easily) stretch to match the disorder potential, resulting in a high (low) depinning temperature[79]. The nature of pinning phenomena has been studied theoretically in a wide variety of condensed matter systems, e.g., charge density waves[80], Wigner crystals[81], and superconducting vortex lattices[82], moreover, Nuclear Magnetic Resonance has proven to be a powerful local probe of pinning/depinning physics[83, 84, 85]. In the present case, the data appear to be consistent with the "weak pinning" limit[80].

This picture can be made more quantitative by comparing the data in Fig. 4.2 to simulated OPNMR spectra that consider the effect of skyrmion dynamics. Recently, in order to simulate spectra obtained near $\nu$=1/3, we proposed a simple, bipolar model for the effect of spin-reversed quasiparticle dynamics on the OPNMR lineshape[56]. In this simulation, the OPNMR linewidth increases substantially as the time scale, $\tau$, for local field fluctuations due to the motion of quasiparticles, passes through $\frac{1}{2K_{Sint}^{\nu=1}(T\to 0)}$ (i.e., $\Theta \sim 1$). A more realistic model, which considered the effects of two-dimensional

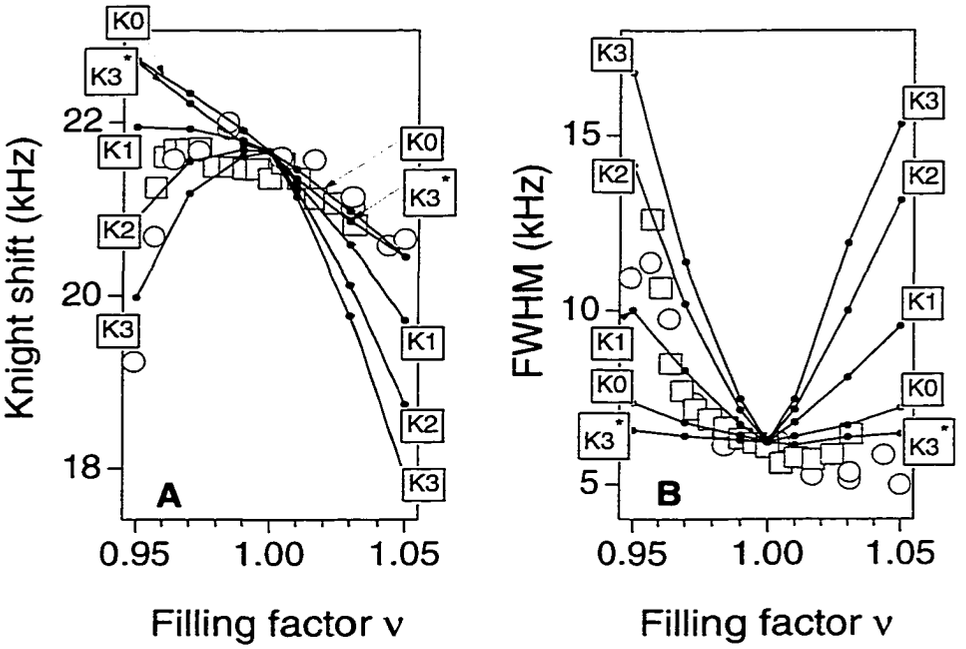


Figure 4.4: Open symbols are $[K_S(\nu), \Gamma_w(\nu)]$ data from Fig. 2C. Filled points are $[K_S^{Sim}(\nu), \Gamma_w^{Sim}(\nu)]$ extracted from simulations described in the text. The points for each skyrmion type are joined by lines.

diffusional motion of a square lattice of conventional K3 skyrmions past fixed nuclei, was introduced recently by J. Sinova *et al.*[86] to explain the spectra near $\nu = 1$. The maximum NMR linewidth within this model also occurs at $\tau \approx \frac{1}{2K_{Sint}^{\nu=1}(T\to 0)}$.

Motivated by this improved model for skyrmion dynamics in real space, we have simulated the "motional narrowing" of the lineshape for each of the skyrmion shapes considered in Fig. 4.4[87]. In this simplified model, a nuclear spin "jumps" from a point inside a skyrmion unit cell to another point randomly and spends a time $\tau$ at each position. The NMR signal is calculated by averaging the signal from 500 such nuclei that start at arbitrary positions within the Skyrmion unit cell. By varying $\tau$, we can control the characteristic fluctuation time of the local field felt by the nuclei. We find that the maximum value of the linewidth is insensitive to the skyrmion shape, but is very sensitive to the number of reversed spins [e.g., $\Gamma_w^{max}(\mathrm{K3}) \approx \Gamma_w^{max}(\mathrm{K3^*})$].

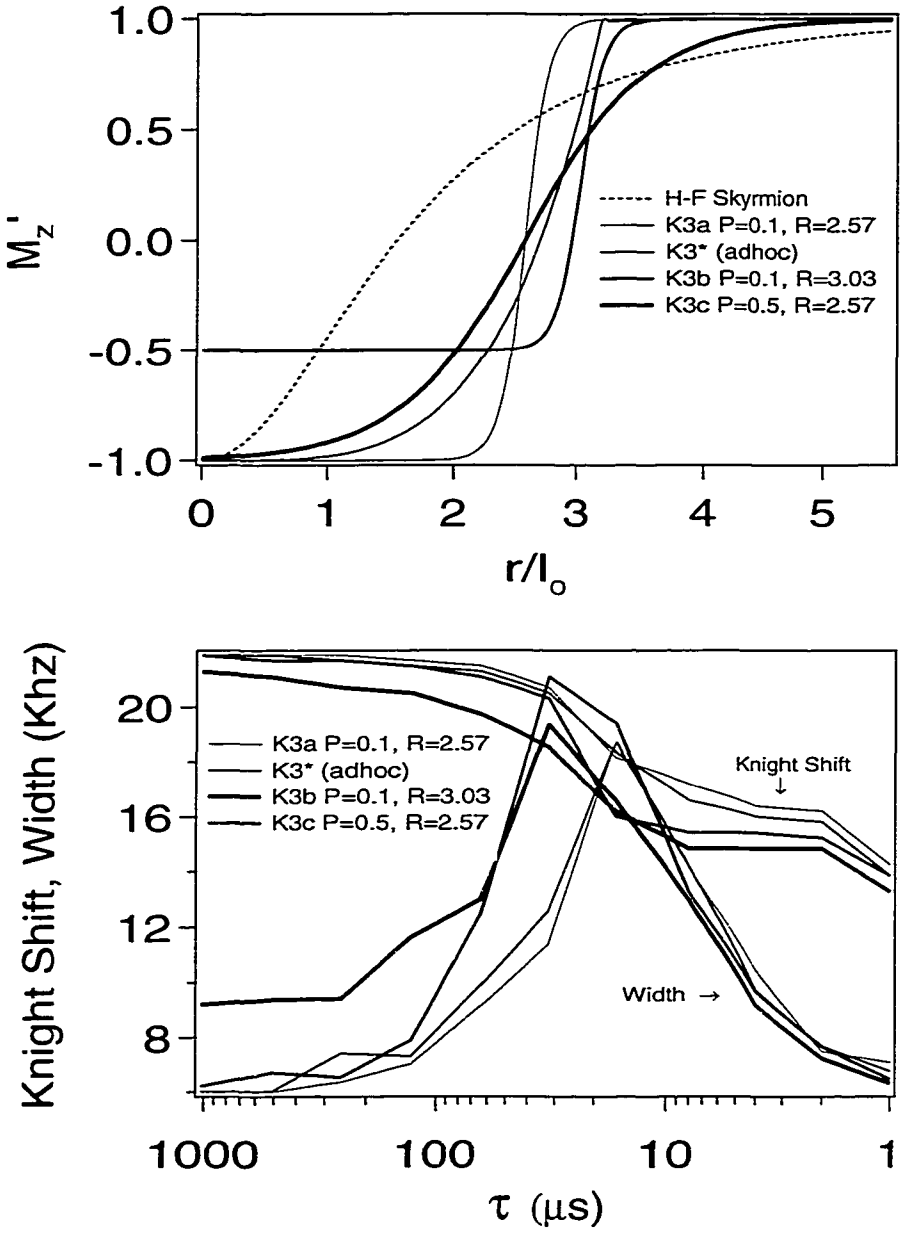


Figure 4.5: Knight shift and well width for $K3a$, $K3b$, $K3c$ and $K3*$ at $\nu$=0.95 as a function of the characteristic fluctuation time of the local field, $\tau$. Also shown is a solution that closely resembles the Hartree-Fock solution for the Skyrmion shape (dashed line[86]).

For example, shown in Fig. 4.5 are five curves curves for $M_z'(r)$ with K=3, including four adhoc curves and a solution that closely resembles the Hartree-Fock solution for the Skyrmion shape (dashed line[86]). Their corresponding Knight shifts and widths are plotted as a function of $\tau$ for $\nu$=0.95. Here $K3a$ and $K3c$ are given by $1-2/(1+exp((x-R)/P))$ and $K3b$ is given by $1-1.5/(1+exp((x-R)/P))$.

Moreover, the simulated linewidth for the K0 skyrmion hardly changes in going from the "frozen" to the "motionally-narrowed" limit, in sharp contrast to the data. Finally, at $|\delta\nu| = 0.031$, the measured $\Gamma_w^{max} \approx \Gamma_w^{max}(\mathrm{K3}^*)$. Therefore, the simulations also show that the data require $K \approx 3$, even for $\Theta \rightarrow 1$, where a skyrmion takes $\sim 20\mu$s to travel over the inter-skyrmion spacing.

In our earlier measurements of $\Gamma_w(T)$ near $\nu = 1/3$, $\Gamma_w^{max}$ increased monotonically as $|\delta\nu|$ increased, while $T_{max}$ was roughly independent of $|\delta\nu|$[56]. However, $\Gamma_w(T)$ near $\nu = 1$ is quite different (Figure 4.2), since $T_{max}$ decreases monotonically as $|\delta\nu|$ increases, while $\Gamma_w^{max}$ is roughly independent of $|\delta\nu|$. In order to compare our simulated $\Gamma_w^{Sim}(\tau)$ to *both* data sets, we must first determine the mapping between $\tau$ and $T$.

Recent simulations of the motion of a superconducting vortex lattice past fixed nuclei suggested a simple dependence of the resulting NMR $T_2$ on the characteristic fluctuation time of the local field, $\tau$[85]. In our simulations of the motion of a skyrmion lattice past fixed nuclei, we found that the NMR linewidth is well-described by a similar expression: $\Gamma_w^{Sim}(\tau) = \Gamma_w^{min} + (\Gamma_w^{max} - \Gamma_w^{min})\frac{2\tau\tau_{max}}{\tau^2+\tau_{max}^2}$, where $\Gamma_w^{min} \sim 6$ kHz, $\tau_{max} \approx \frac{1}{2K_{Sint}} \sim 20\mu s$, and $\Gamma_w^{max}$ depends upon $\delta\nu$. If we assume that $\tau$ follows an Arrhennius law [i.e., $\tau$=$\tau_o exp(U/T)$, where $\tau_o$=$\tau_{max}/exp(U/T_{max})$], we arrive at an expression for $\Gamma_w^{Sim}(T)$ that is a good fit (solid lines) to the $\Gamma_w(T)$ data in Fig. 4.2. The best-fit values of the activation energy $U$ and the uncertainty $\Delta U$ may be extracted at each $|\delta\nu|$:

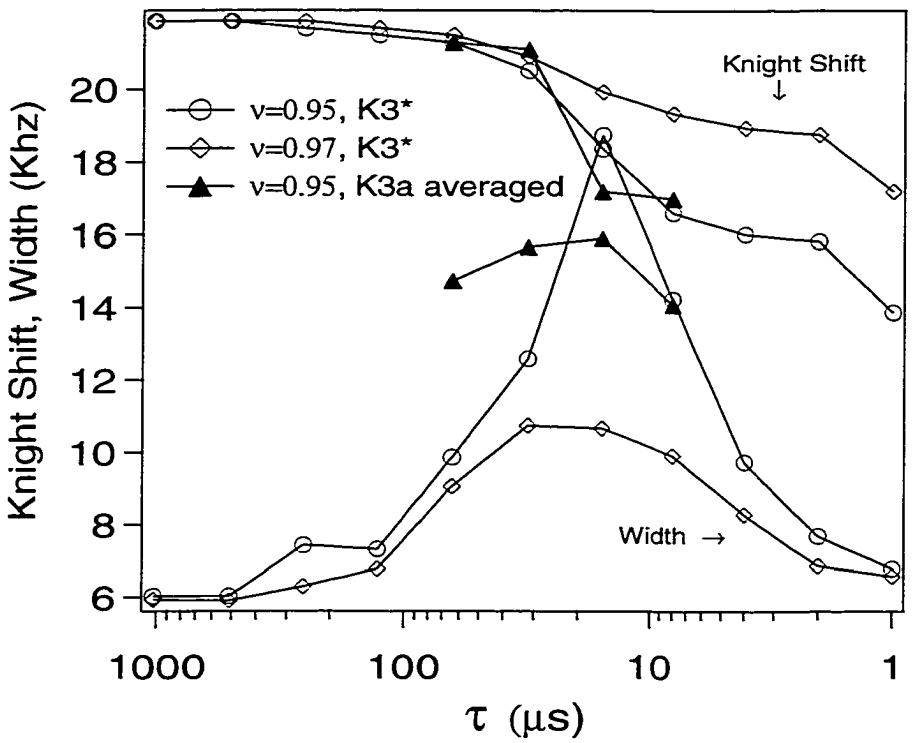


Figure 4.6: Knight shift and well width for K3* at $\nu$=0.95 and $\nu$=0.97 as a function of $\tau$. Also shown is the Knight shift and well width for $K3a$ for $\nu$=0.95 averaged over different values of $U$ as described in the text.

| $\nu$ | $\lvert\delta\nu\rvert$ | $U$ [K] | $\Delta U$ [K] | $T_{max}$ | $\tau_o[\mu s]$ |
|---|---|---|---|---|---|
| 0.969 | 0.031 | 8.0 | ±1.1 | 2.4 | 0.7 |
| 1.045 | 0.045 | 4.2 | ±1.6 | 1.7 | 1.7 |
| 0.949 | 0.051 | 0.6 | ±0.8 | 0.6 | 7.4 |

As $|\delta\nu|$ increases, $\Delta U/U$ grows from ~1/8 to ~1. This trend is additional evidence that the localization is caused by the weak pinning of a skyrmion crystal. In such a picture, each domain "j" of the crystal has a local activation energy $U_j$, which has a gaussian distribution $g(U_j)$ across the sample, consistent with the measured ($U$, $\Delta U$) for each $|\delta\nu|$. As a consequence, domains throughout the sample share a common $T_{max}$ for small $\Delta U/U$[88], but at large $\Delta U/U$, $T_{max}$ *varies from domain to domain.*

As a consistency check, we find that the measured $\Gamma_w(T,|\delta\nu|)$ are in good agreement with the $< \Gamma_w^{Sim}(T,|\delta\nu|) >_{g(U_j)}$ extracted from simulated spectra that assume a spread in the local $T_{max}$ across the sample (Fig. 4.6).

In summary, the weak pinning of a crystal of adhoc K3* skyrmions is in good quantitative agreement with our data. This skyrmion shape is surprising, since the energetic considerations of a *single skyrmion* state would favor the conventional K3 over the shorter tailed K3*. However, this preference may not be the same in a *many skyrmion* state, where the energetics are more complicated.

# Chapter 5

# $\nu$=1/2: Landau Levels vs. Fermi Circles

Despite the overall agreement between theory and experiment to date, several fundamental issues about CF at $\nu=\frac{1}{2}$ have yet to be resolved experimentally. For example, do CF form a Fermi gas, a "normal" Fermi liquid, or some kind of "unusual" Fermi liquid? Also, does the picture change when the ground state is only partially spin-polarized[89, 90, 91]? Experiments which directly probe the electron spin degree of freedom *right at* $\nu=\frac{1}{2}$, especially near the transition between partially and fully spin-polarized ground states, will help to answer these central questions. We will present $K_S$ data[92], which reveal the spin polarization $\mathcal{P}(T) \equiv \frac{\langle S_z(T)\rangle}{\max\langle S_z\rangle}$, and $1/T_1$ data, which probe the spin dynamics of the 2DES. Taken together, these thermodynamic measurements can provide unique insights into the physics of CF at $\nu=\frac{1}{2}$.

### 5.0.20 Three Different Cases with Half Filling

Since the maximum Knight shift for a fully polarized 2DES is known for each

sample, $K_{Sint}^{\mathcal{P}=1} = K_{Sint}(\nu=\frac{1}{3},T\to 0)$, the electron spin polarization at $\nu$=1/2 is obtained using:

$$\mathcal{P}(\nu=\frac{1}{2},T) = \frac{K_{Sint}(\nu=\frac{1}{2},T)f(\nu=\frac{1}{2})}{K_{Sint}^{\mathcal{P}=1}f(\nu=\frac{1}{3})}, \tag{5.1}$$

where $f = 2n/[wn_{3D}(0)]$ accounts for the small change in the 3D electron density at the center of the quantum well, $n_{3D}$, for different $B_{tot}$ and $\theta$. Note that the $f$ factors were not needed when measuring the polarization for $\nu$=1/3 or 1, because the ground state at $\nu$=1/3 or 1 is fully polarized, and we were able to measure the maximum Knight shift at those filling factors. The use of the $f$ factor is necessary when comparing Knight shifts that were measured at different filling factors (even though the polarization might be unity at $\nu$=1/2 and 1/3 under certain low temperature conditions, the Knight shifts will not be equal because of the different 3D electron densities at the center of the quantum well).

Using the rotator assembly, we could set the angle $\theta$ between the sample's growth axis and the applied field $B_{tot}$ so that the filling factor $\nu=nhc/eB_{\perp}$ (with $B_{\perp}\equiv B_{tot}\cos\theta$) equalled $\frac{1}{2}$. In this section, we describe results obtained for the first three of the following six cases:

| | | $\nu$ | $B_{tot}$ [T] | $\theta$ | $n$ [cm$^{-2}$] | $w$ [Å] | $f$ |
|---|---|---|---|---|---|---|---|
| I | 40W | 1/2 | 7.03 | 38.3° | $6.69\times 10^{10}$ | 300 | 1.17 |
| II | 40W | 1/2 | 5.52 | 0.0° | $6.69\times 10^{10}$ | 300 | 1.19 |
| III | 10W | 1/2 | 7.03 | 24.5° | $7.75\times 10^{10}$ | 260 | 1.20 |
| IV | 10W | 1/2 | 6.40 | 0.0° | $7.75\times 10^{10}$ | 260 | 1.21 |
| V | 40W | 1/3 | 12.0 | 46.4° | $6.69\times 10^{10}$ | 300 | 1.14 |
| VI | 10W | 1/3 | 12.0 | 36.8° | $7.75\times 10^{10}$ | 260 | 1.18 |

V and VI are simply the $\nu$=1/3 cases described before.

Figure 5.1 shows OPNMR spectra at $\nu=\frac{1}{2}$ and $T\approx 0.5$ K, for Cases I–III (a-c, solid

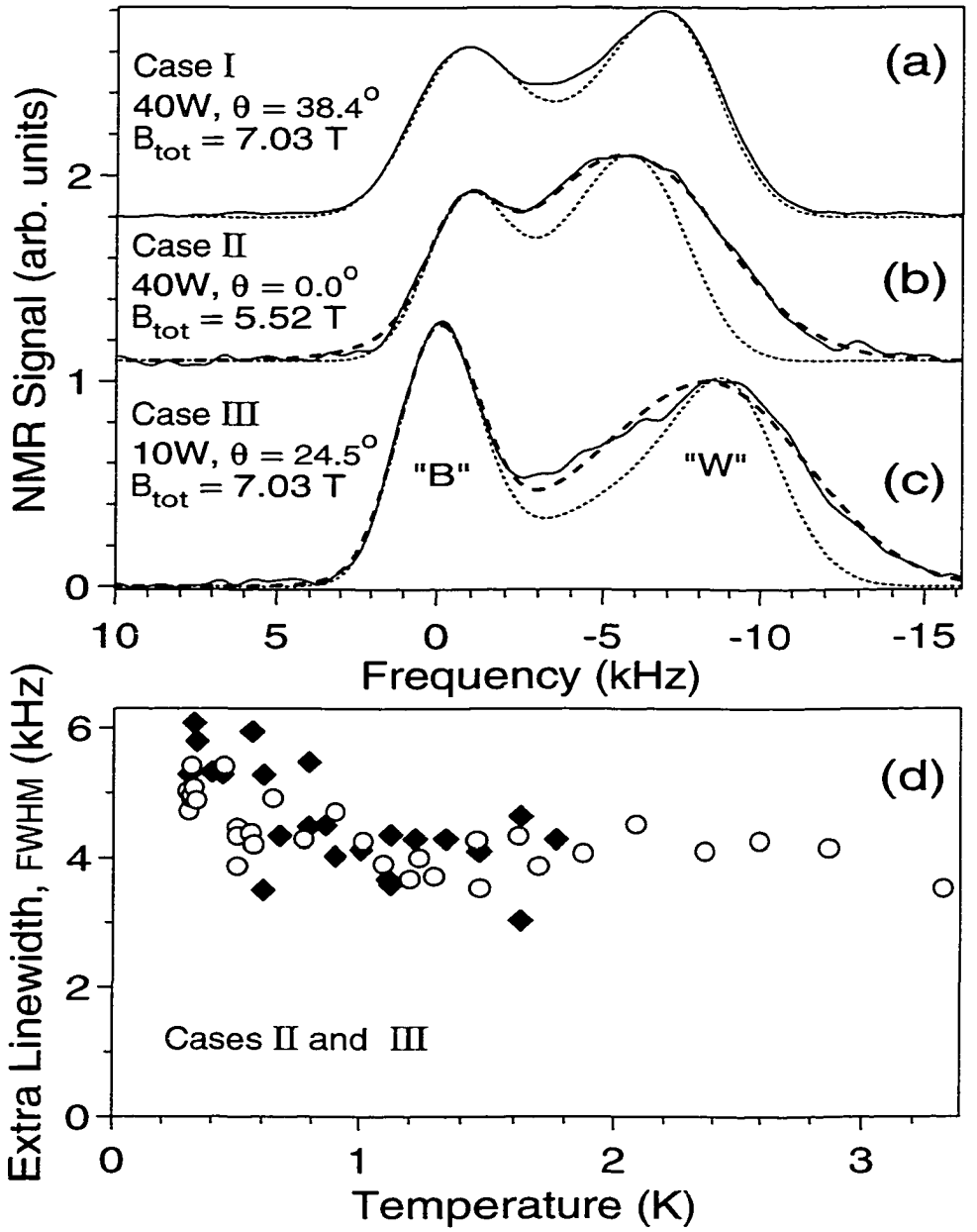


Figure 5.1: $^{71}$Ga OPNMR spectra (a-c, solid lines) at $\nu$=$\frac{1}{2}$, $T \approx 0.5$ K. The dotted line fits (a)-(c) use a 3.5 Khz FWHM Gaussian broadening (due to nuclear spin-spin coupling) of the intrinsic well and barrier lines. The dashed line fits (b) and (c) require an extra Gaussian broadening of "W" with the FWHM shown in (d) for samples 40W (open circles) and 10W (filled diamonds).

lines). For Case I, all spectra (e.g., Fig. 5.1(a)) are well-described by the same two-parameter fit (dotted lines)[55, 56] that was used before for all spectra at $\nu=\frac{1}{3}$. This fit is generated under the assumption that all spins are delocalized, so that $\langle S_z(\nu,T)\rangle$, averaged over the NMR time scale ($\sim 40\,\mu$sec), appears spatially homogeneous along the plane of the wells, and thus the resulting lineshape is "motionally-narrowed" [43].

In contrast, for Cases II and III, the well resonance [Fig. 5.1(b) and 5.1(c)] is much broader than the same fit (dotted lines). An additional gaussian broadening of just the well resonance leads to a better fit (dashed lines). The full width at half maximum (FWHM) of the additional broadening extracted from these fits is plotted in Fig. 5.1(d) for Cases II and III. Earlier measurements at $\nu < \frac{1}{3}$ were also poorly described by the "motionally-narrowed" lineshape, but in that case the extra well width was sharply temperature-dependent. The extra broadening of the well lineshape for Cases II and III (Fig. 5.1(b,c,d)) seems to be homogeneous. In simulations, we found that an unreasonably large FWHM of 70% or more is required for a gaussian distribution of electron densities along the well to explain the large temperature independent linewidth observed at $\nu=\frac{1}{2}$ for Cases II and III. If this extra broadening is homogeneous, the corresponding transverse relaxation time $T_2$ [43] is quite short. The origin of this effect is not understood as it is very hard to explain simultaneously the temperature-independence of the extra broadening and the lack of a similar effect in Case I.

Figure 5.2(a) shows $K_S(T)$ at $\nu=\frac{1}{2}$ for Cases I–III. The larger scatter in the $K_S(T)$ data for Cases II and III is a consequence of the large linewidth. Using the empirical relation (all in kHz) $K_{S\mathrm{int}} = K_S + 1.1\times(1-\exp(-K_S/2.0))$ discussed before, we can convert $K_S$ into $K_{S\mathrm{int}}$, which is the intrinsic hyperfine shift for the nuclei in the center of each well, and is a direct measure of the electron spin polarization $\mathcal{P}$. For Cases II and III, the same values of $K_{S\mathrm{int}}(T)$ are also obtained directly from the

dashed line fits [e.g., Fig. 5.1(b) and 5.1(c)].

### 5.0.21 Partially and Fully Polarized Ground States

Figure 5.2(b) and 5.2(c) shows that $\mathcal{P}(\nu{=}\frac{1}{2},T)$ does not saturate down to our base temperature of 0.29 K, in contrast to earlier measurements at $\nu$=1 and $\frac{1}{3}$ [55, 22]. Moreover, as the temperature is increased, $\mathcal{P}(\nu,T)$ falls off much faster at $\nu{=}\frac{1}{2}$ than at $\nu$=1 or $\frac{1}{3}$ (e.g., at $T_Z{=}|g^*\mu_e B_{\rm tot}/k_B|$, $\mathcal{P}(\nu{=}1,T_Z)\approx 93\%$, while $\mathcal{P}(\nu{=}\frac{1}{2},T_Z)\approx 40\%$. Here $g^*{=}{-}0.44$, $\mu_e$ is the Bohr magneton and $k_B$ is the Boltzmann constant). Qualitatively, these results are consistent with a tiny (or vanishing) energy gap for spin-flip excitations at $\nu{=}\frac{1}{2}$ for Cases I–III. However, a quantitative understanding of the $\mathcal{P}(\nu{=}\frac{1}{2},T)$ data remains a challenge for theory {e.g., we cannot explain the crossing of the Case I and Case II data sets at $T{\approx}T_Z$ [Fig. 5.2(b)]}.

Even though saturation is not observed, the Knight shift data for Case II are evidence for a $\nu{=}\frac{1}{2}$ ground state in which the electrons are only *partially* spin-polarized [i.e., $\mathcal{P}(\nu{=}\frac{1}{2},T\rightarrow 0)\approx 75-85\%$]. This inference is consistent with data obtained from two other experiments in conditions similar to those of Case II. From their time-resolved photoluminescence measurements, Kukushkin et al.[90] estimate $\mathcal{P}(\nu{=}\frac{1}{2},T\rightarrow 0)\approx 87\%$ at 5.52 T. Surface acoustic wave measurements of Willett et al. obtained a Fermi wave vector which was $\sim$ 90% of the theoretical value for fully polarized CF, consistent with a polarization of at least $\mathcal{P}(\nu{=}\frac{1}{2},T\rightarrow 0)\approx 62\%$.[15]

### 5.0.22 WICFM

The solid curves in Figure 5.2(b) and 5.2(c) are two parameter fits to the $T{<}T_Z$ data using expressions for $\mathcal{P}(\nu{=}\frac{1}{2},T)$ derived within a weakly-interacting composite

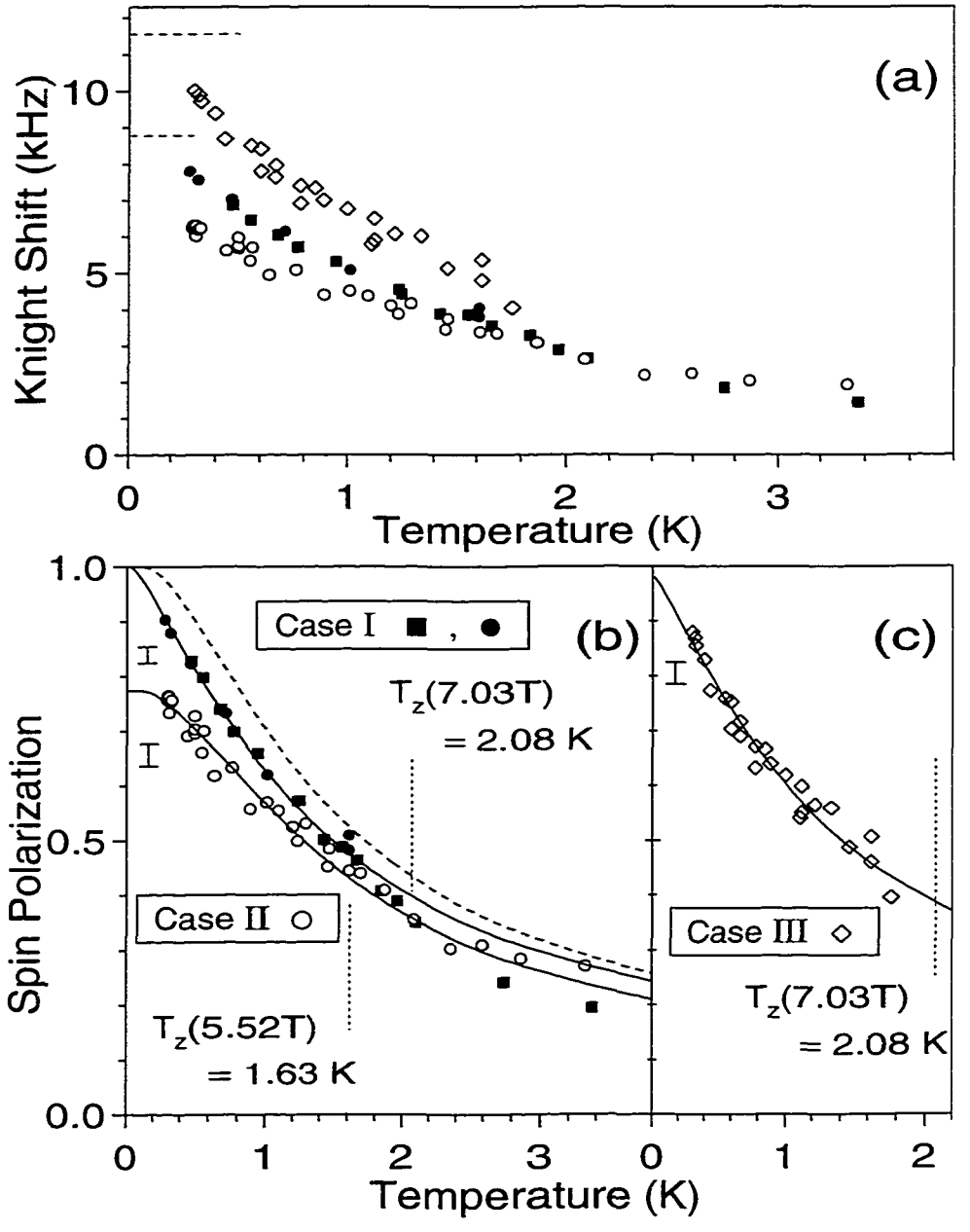


Figure 5.2: Temperature dependence at $\nu$=$\frac{1}{2}$ of (a) $K_S$ and (b, c) $\mathcal{P}$ for Case I (open diamonds), Case II (filled symbols), and Case III (open circles). Note the error bars in (b) and (c). The solid and dashed curves are described in the text.

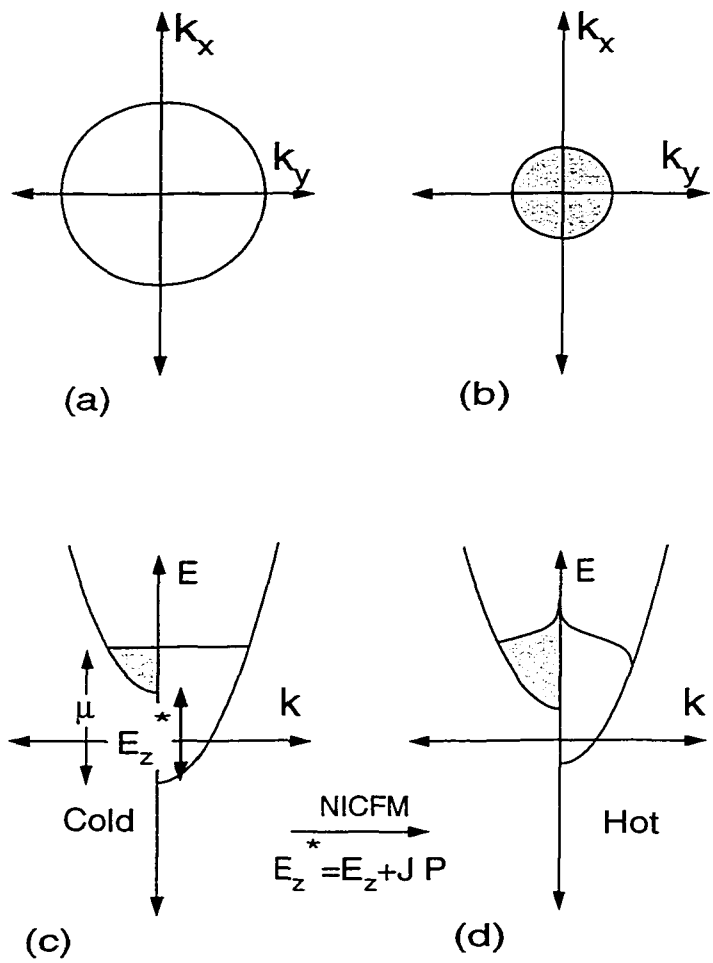


Figure 5.3: $k_x - k_y$ plot of the states which are occupied in the WICFM model for (a) spin up and (b) spin down electrons. Schematic of the dispersion relations and occupation numbers for the WICFM model shown for the spin up and spin down electrons under (c) cold and (d) hot temperature conditions. is varied. Note that in the WICFM model, the effective Zeeman energy drops as the temperature is increased.

fermion model (WICFM). In this model, the dispersion relations for spin-up and spin-down states are:

$$E_{\uparrow}(k) = \frac{\hbar^2 k^2}{2m^*}, \quad E_{\downarrow}(k) = \frac{\hbar^2 k^2}{2m^*} + E_Z^*(T)\,, \tag{5.2}$$

where an exchange interaction has been included in the model through the effective Zeeman energy:

$$E_Z^*(T) = |g^*\mu_e B_{\rm tot}| + E_{\rm Exch} = k_B T_Z + k_B J\mathcal{P}(T)\,. \tag{5.3}$$

When $J = 0$, this is just the non-interacting composite fermion model[90]. When $J > 0$, there is a Stoner enhancement of the spin susceptibility. Fig. 5.3 shows a rough schematic of the occupation numbers and the dispersion curves for the spin up and spin down electrons in the WICFM model. The electron occupy energy levels which are continously spaced, up to the Fermi energy. Here, the spin up band is occupied more than the spin down band because Zeeman energy tends to favor the occupation of the spin up band.

The chemical potential $\mu$ and the polarization $\mathcal{P}$ in this model can be written as:

$$\mu(T) = k_B T \ln\Big(-\gamma + \sqrt{\gamma^2 + \exp(\rho) - 1}\Big) + \frac{E_Z^*(T)}{2} \tag{5.4}$$

$$\mathcal{P}(T) = \frac{1}{\rho}\ln\Big(\frac{1 + \exp[\frac{\mu(T)}{k_B T}]}{1 + \exp[\frac{\mu(T)}{k_B T}(1 - \delta(T))]}\Big) \tag{5.5}$$

where

$$\gamma = \cosh(\frac{E_Z^*(T)}{2k_B T});\ \rho = \frac{2\pi\hbar^2 n}{m^* k_B T};\ and\, \delta(T) = \frac{E_Z^*(T)}{\mu(T)}.$$

Equations 5.3–5.5 are solved self-consistently for $\mathcal{P}(T)$ at each $m^*$ and $J$. Within this WICFM, the behavior of $\mathcal{P}(T)$ as $T\to 0$ is quite sensitive to the parameter $\delta(0)$. The ground state is only fully polarized ($\mathcal{P}(0)$=1) when $\delta(0)\geq 1$. We find $\delta(0)<1$ for Cases II and III, $\delta(0)>1$ for Case I, and the dashed curve illustrates an even larger

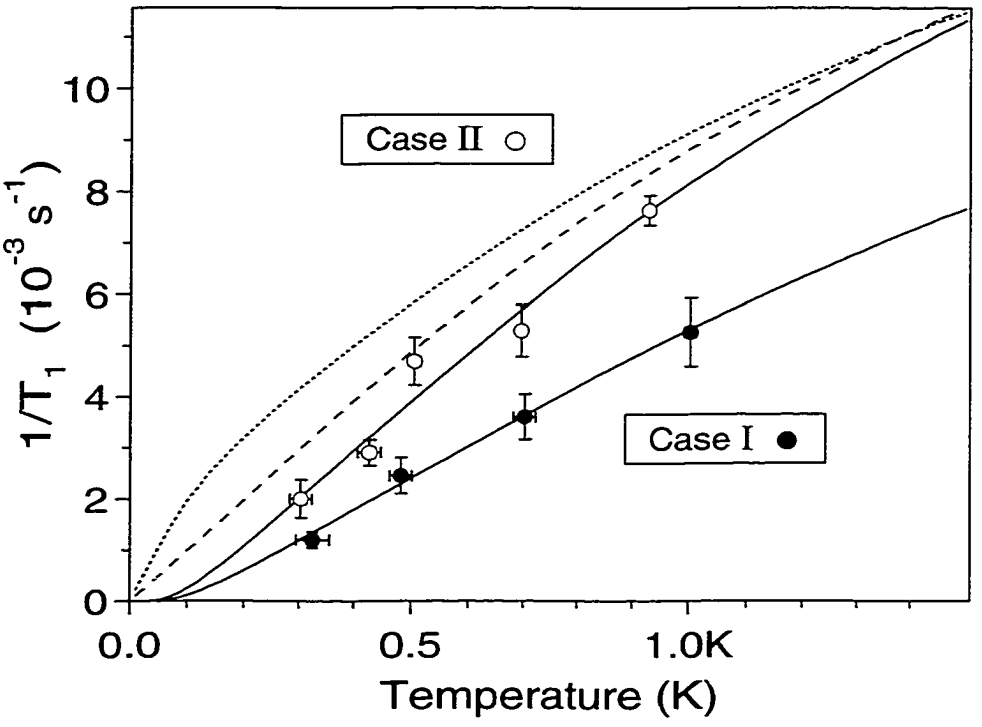


Figure 5.4: Temperature dependence of the $^{71}$Ga spin-lattice relaxation rate $1/T_1$ at $\nu=\frac{1}{2}$ for Case I (filled symbols) and Case II (open symbols). The solid and dashed curves are described in the text.

$\delta(0)$ [Fig. 5.2(b) and 5.2(c)]. Thus, within this model, the best-fit curves for Cases II and III yield partially-polarized ground states, while Case I is fully-polarized. As described earlier, Cases II and III also have extra linewidth, while Case I does not Fig. 5.1).

Figure 5.4 shows the temperature dependence of the $^{71}$Ga nuclear spin-lattice relaxation rate $1/T_1$ at $\nu=\frac{1}{2}$ for Cases I and II. At each temperature, OPNMR spectra were acquired using a series of dark times $10\,\mathrm{s} \leq \tau_D \leq 2560\,\mathrm{s}$ (i.e., the longest $\tau_D \geq 4T_1$). The value of $1/T_1$ was determined by fitting the signal intensity at the "W" peak frequency to the form $S(\tau_D) = S_0 \exp(-\tau_D/T_1) + S_1$. Note that these $T < T_Z$ relaxation rates are faster than the rate at $T \approx T_Z$ for $\nu$=1 [33]. Qualitatively, this shows that there is a greater overlap of the density of states for electrons with

opposite spins at $\nu=\frac{1}{2}$ than at $\nu$=1.

The isotropic Fermi contact hyperfine coupling between the electron spins and the nuclear spins is responsible for both $K_S$ and $1/T_1$ [55, 56, 22, 33], as is the case for some metals[43, 50]. Within the WICFM, $1/T_1(\nu=\frac{1}{2},T)$ for $^{71}$Ga nuclei in the center of the quantum well is:

$$\frac{1}{T_1} = \frac{\pi(m^*)^2}{\hbar^3}\left(\frac{fK_{Sint}^{P=1}}{n}\right)^2 \frac{k_B T}{1+\exp\left[\frac{\mu(T)}{k_B T}(\delta(T)-1)\right]}. \quad (5.6)$$

This expression is used as a two-parameter fit to the $1/T_1(T)$ data (Fig. 5.4, solid lines), where $\mu(T)$ and $\delta(T)$ are obtained from Eqns.5.3–5.5 for each $m^*$ and $J$. The behavior of $1/T_1(T)$ as $T \rightarrow 0$ is also quite sensitive to the parameter $\delta(0)$. In Fig. 5.4, we illustrate $\delta(0) < 1$ with the dotted curve, $\delta(0) = 1$ with the dashed curve, and we find $\delta(0) > 1$ for Cases I and II (solid curves). In contrast to normal metals, here $k_B T$ can be greater than $\mu(0)$.

### 5.0.23 If it doesn't fit, You must acquit

Figure 5.5 shows the best values of $J$ and $m^*$ obtained for each data set in Figs. 5.2(b) and 5.2(c) and 5.4. The correlation between $J$ and $m^*$ is shown by $\Delta\chi^2$=1 and $\Delta\chi^2$=4 contours. These ($J$,$m^*$) values lie quite close to the curves which mark the transition between fully and partially polarized ground states (i.e., where $\delta(0)$=1). There is negligible overlap between the contours and the line $J$=0, so the non-interacting composite fermion model used by Kukushkin et al. [90] does not work here. Moreover, there is no ($J$,$m^*$) pair which can simultaneously describe the four data sets measured using the same sample and $B_\perp$ (Fig. 5.5 (main)), so we conclude that even the weakly-interacting composite fermion model is a poor description of the $\nu=\frac{1}{2}$ state for these Cases. The most glaring inconsistency is that of Case II,

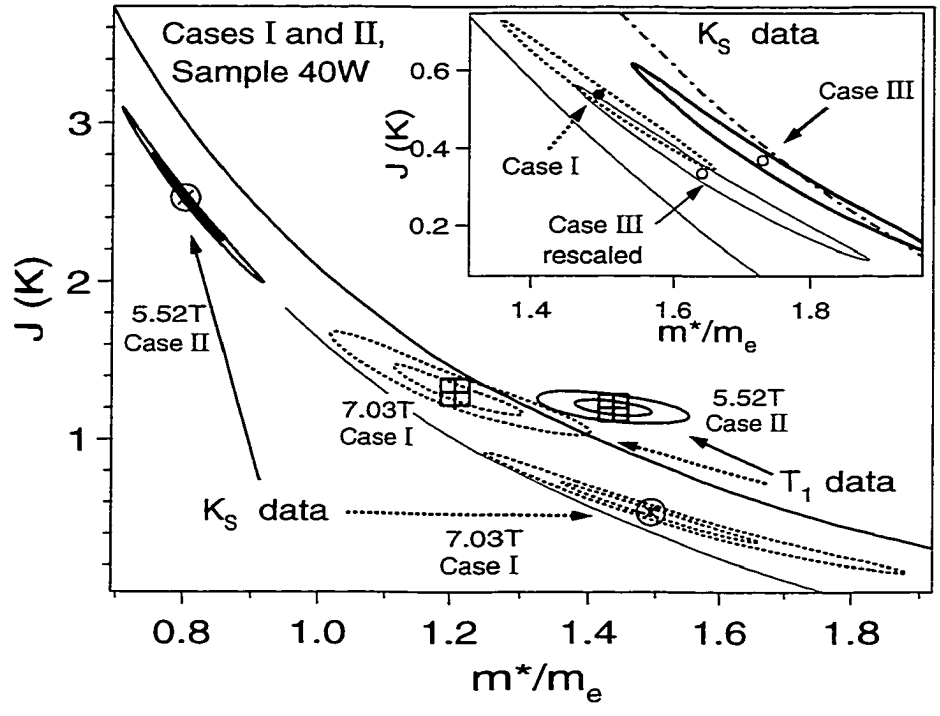


Figure 5.5: Values of $J$ (in Kelvin) and $m^*$ (in units of the electron mass in vacuum, $m_e$), obtained using a $\chi^2$ analysis of : (main) $\mathcal{P}(T)$ (circles) and $1/T_1(T)$ (squares) for Case I (dashed contours) and Case II (solid contours), and (inset) $\mathcal{P}(T)$ for Case I (dashed contour) and Case III (thick solid contour). The thin solid contour in the inset shows the rescaled Case III values described in the text. Within the WICFM, the ground state is fully spin-polarized for ($J$,$m^*$) values that lie above the thin solid curve (Case I), thick solid curve (Case II), or dashed-dotted curve (Case III, inset).

where $\delta(0)<1$ (i.e., partially-spin polarized at $T$=0) is inferred from $\mathcal{P}(T)$, which is *incompatible* with the result $\delta(0)>1$ (i.e., fully-spin polarized at $T$=0) that is inferred from $1/T_1(T)$.

Figure 5.5 (inset) shows the ($J$,$m^*$) values obtained from the $\mathcal{P}(T)$ data for Cases I and III. These values do not agree, however, sample 10W and 40W also have slightly different electron densities and well widths ($n$,$w$). This would affect our results, since we expect $k_B J \propto eB_\perp/m^* \propto E_C(\lambda) \equiv e^2/(\epsilon\sqrt{l_0^2+\lambda^2})$, where $l_0=\sqrt{\hbar c/eB_\perp}$ is the magnetic length, $\epsilon$=13, and the parameter $\lambda \approx \frac{1}{4}w$ modifies the Coulomb energy scale due to the non-zero thickness $w$ of the quantum well [93]. To correct for this,

the Case III ($J$,$m^*$) values are rescaled using:

$$\frac{J(n_{\rm I}, w_{\rm I})}{J(n_{\rm III}, w_{\rm III})} = \sqrt{\frac{n_{\rm I}}{n_{\rm III}}\left(\frac{4+\pi n_{\rm III} w_{\rm III}^2}{4+\pi n_{\rm I} w_{\rm I}^2}\right)},$$
$$\frac{m^*(n_{\rm I}, w_{\rm I})}{m^*(n_{\rm III}, w_{\rm III})} = \sqrt{\frac{n_{\rm I}}{n_{\rm III}}\left(\frac{4+\pi n_{\rm I} w_{\rm I}^2}{4+\pi n_{\rm III} w_{\rm III}^2}\right)}. \quad (5.7)$$

The rescaled contour has a good overlap with the ($J$,$m^*$) values for Case I (Fig. 5.5 (inset)). This rescaling is irrelevant for Fig. 5.5 (main), where the results on a single sample are shown.

Neither a non-interacting nor a weakly-interacting composite fermion model is sufficient to explain our experiments, which probe the electron spin degree of freedom *right at* $\nu=\frac{1}{2}$. However, a recent theoretical approach by R. Shankar[94] that uses the hamiltonian theory of Composite Fermions is in good agreement with our data. Shown in Fig. 5.6 is a plot of our data shown before (Figs. 5.2, 5.4) compared to the predictions of this theory using a single parameter $\lambda$. Also shown in Fig. 5.7 are dispersion relations generated by this theory for particles at $\nu$=1/2 at $T$=0.01K with $B_{tot}$=$B_\perp$=5.52T. Note that the lower dispersion curve is more flat at small $k$ than the upper dispersion curve and cannot be fit with just a quadratic form.

Knight shift and $1/T_1$ data, taken together, provide important new constraints on the theoretical description of the $\nu = \frac{1}{2}$ state. Finally, in addition to fully polarized ground states (Case I, $\frac{k_B T_Z}{E_C(\lambda)}$=0.021), partially spin-polarized ground states (Cases II and III, $\frac{k_B T_Z}{E_C(\lambda)}$=0.017 and 0.019) are experimentally accessible, and exhibit unexpected features (e.g., the extra linewidth).

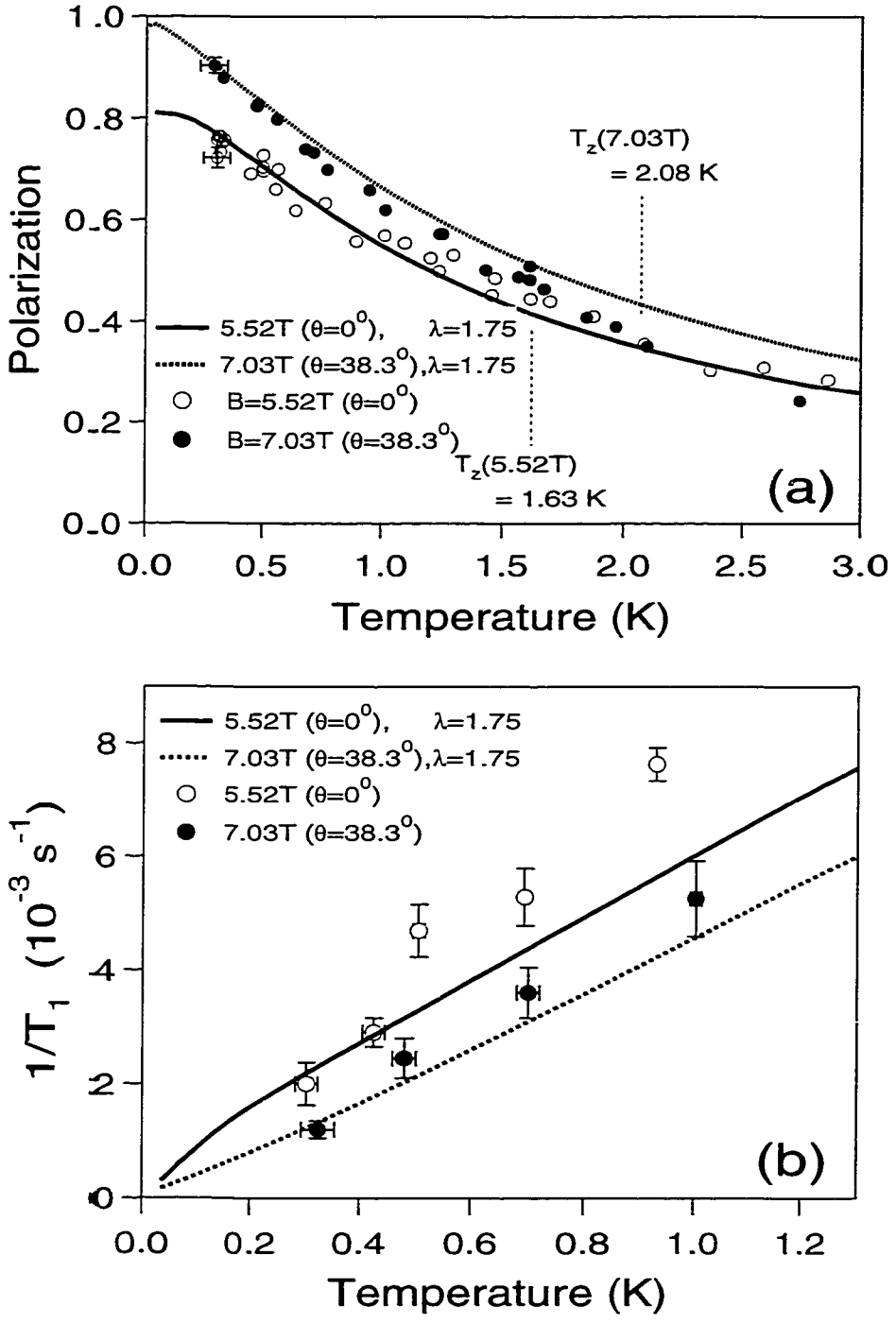


Figure 5.6: Comparison of our data to a recent theory by R. Shankar[94] that uses the hamilonian theory of Composite Fermions with one fitting parameter $\lambda$ to describe the $\nu$=1/2 state.

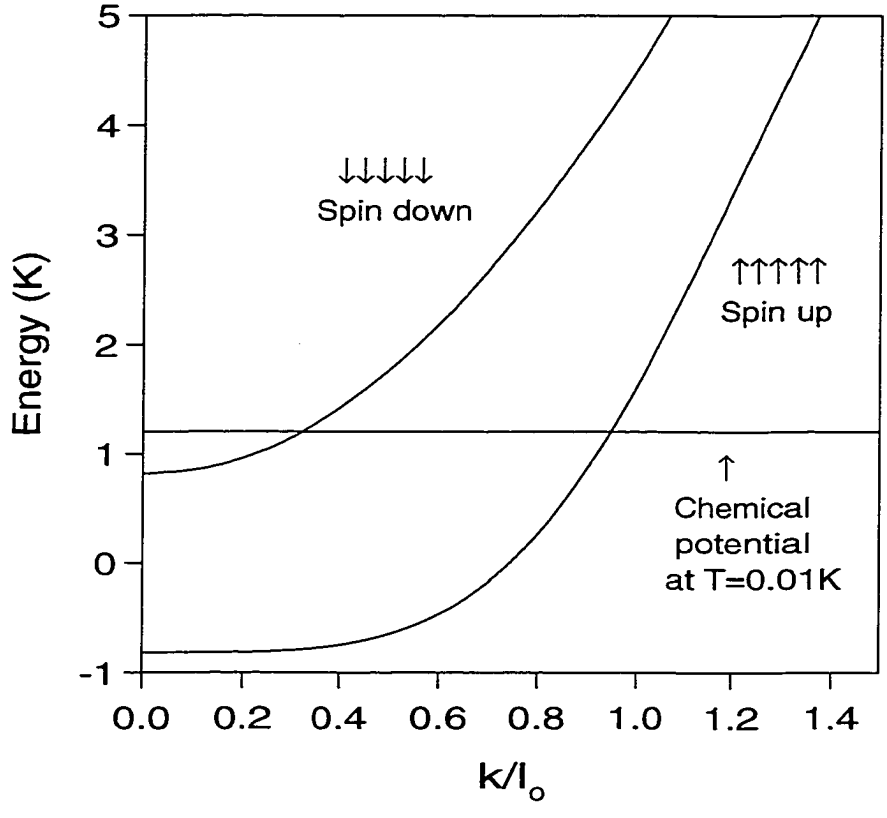


Figure 5.7: Dispersion relations using the theory by R. Shankar[94] for particles at $\nu$=1/2 at $T$=0.01K with $B_{tot}$=$B_{\perp}$=5.52T. The chemical potential is also shown. Note that the lower dispersion curve is more flat at small $k$ than the upper dispersion curve and cannot be fit with just a quadratic form.

# Chapter 6

# GaN: GaN't See the Satellites?

### 6.0.24 Introduction

Red and yellow semiconductor diode lasers and LED's have found several useful applications in industry, e.g. in telecommunications (optical fiber networks), data storage (compact-disk technology), document production (laser printers), and traffic lights. However, the light from these diodes is only able to span only a small portion of the complete color spectrum that can be achieved by combining red, blue and green light. In order to make full color displays, one needs to have a blue and a green light emitting device in addition to a red one. Several recent advances in GaN device technology have led to new blue green bright light sources. Although not as advanced as their red and yellow counterparts, green LED's have already been used to make traffic lights, where they are more efficient and last longer. And recently developed blue lasers could be used to increase data storage capacities by a factor of 4 (over red lasers), and perhaps even increase the resolution for laser printing.

Typical red and yellow LED's have light efficiencies greater than those of incandescent lamps. However, this is not the case for LED's operating in the blue and

ultra-violet portion of the sprectrum. Weak blue LED's make from semiconducting SiC have been fabricated, but they are orders of magnitude less efficient than their red and yellow counterparts. The II-VI semiconducting compounds (especially those based on ZnSe[95]) have shown promise as blue and green light sources, but the ready formation of structural defects tends to dimish their lifetime. In the past three decades, much research has been done on the group III nitrides, alloys of Al-Ga-In-N, which have the bandgap neccessary for blue and UV light emission. However, only recently has much progress in the doping of materials and the processing of these devices been made, culminating in the demonstration by Nakamura et al.[96] of the first extremely bright blue LED in 1994. In early 1997, they were also able to develop the first CW diode laser in the blue-violet range. Blue laser pointers are now commercially available.

Making a LED or a laser diode requires both n- and p- type doped materials. Fabricating hole-doped GaN proved to be especially tricky. Unintentionally doped GaN always turned out to be n type. The first p-type material was grown using low energy electron beam irradiation (LEEBI) activated magnesium-doped GaN films, converting them from a highly resistive state to one having $\sim 10^{16}$ holes[97]. Since then, superior hole concentrations have been achieved by thermal annealing after growth[98]. Despite these significant milestones in the development of GaN based devices, there are still many unresolved questions about the nitrides[99, 100], which are of both fundamental and technological interest.

For example, there is not currently a substate (with lattice parameters matched to the nitrides) for film growth. Due to the strong chemical bonding in these materials, the temperatures required for chemical vapor deposition (CVD) are very high. This tends to limit the choice of substrates to those that are stable at these high temperatures [i.e. Sapphire ($\alpha$-$Al_2O_3$) and SiC]. The materials grown on such mismatched

substrates often contain about $10^{10}$ dislocations per $cm^2$[101], about six orders of magnitude more than what is typical for other materials used for optoelectronic devices. The details of this microstructure and the mechanisms that allow it to be compatible with efficient light emission are not yet understood, so there is the potential for further improvement in these devices (e.g., by lowering the high threshold currents needed in these devices). These materials are very robust light emitters even in the presence of high current densities.

As another example of the unique characteristics of the nitrides, the wurtzite crystal structure is believed to lead to large spontaneous and strain induced macroscopic polarization fields, which are often neglected in studies of these materials. However, these can lead to interesting modifications of the band structure near interfaces in multi-layer compounds[102].

As a final example, the mechanism by which optical gain is produced in the nitrides is also not well understood. InGaN segragation might play an important role in this process. The InGaN alloy is usually unstable and tends to seperate in regions of different compositions. As a result, the injected carriers are then confined in the regions of high Indium content because of their lower bandgap energy. Thus, the optical gain in the nitrides may also be excitonic (involving bound electron hole pairs rather than free charge carriers). Even slight InGaN composition variations could then be significant as they would induce weak potential fluctuations in the quantum well plane leading to excitonic localization.

An understanding of these effects is crucial for the further development of these devices. Hence, it is important to develop new probes of the local structure (e.g., NMR, OPNMR) in these novel materials that can reveal more information about these effects.[103].

Table 6.1: Dimensions and composition data for the GaN samples.

| | Sample B874 | Sample B870 |
|---|---|---|
| 2D Area ($mm^2$) | $8 \times 5$ | $6 \times 4$ |
| x in $In_xGa_{1-x}N$ | 0.07 | 0.21 |
| Mg Doping | yes | no |
| # of $^{71}Ga$ | $2.9 \times 10^{18}$ (0.34 mg) | $1.8 \times 10^{18}$ (0.21 mg) |
| # of $^{69}Ga$ | $4.3 \times 10^{18}$ (0.50 mg) | $2.7 \times 10^{18}$ (0.30 mg) |
| # of $^{115}In$ | $2.3 \times 10^{16}$ (4.4 $\mu$g) | $4.3 \times 10^{16}$ (8.1 $\mu$g) |

### 6.0.25 GaN Samples

Previous NMR work in semiconductors has been able to resolve some of the above issues, e.g., the degree of cation ordering in $In_{0.5}Ga_{0.5}P$ thin films[104]. However, the limited sensitivity of regular NMR techniques has required the use of large samples. Aware of these limitations, we still tried to detect an regular NMR signal from a very thin film of GaN. The samples were provided to us by Dr. Noble Johnson and Dr. Dave Bour of Xerox PARC, along with x-ray and TEM data. The two GaN samples are shown in Fig. 6.1 and the sample parameters are described in Table 6.1. Using MOCVD on a (0001)-sapphire substrate, a quantum well of InGaN is grown on top of a thin film of GaN. Sample B874 is Mg doped while the other is nominally undoped.

### 6.0.26 NMR of GaN Thin Films

Because of the small sample size, detecting the regular NMR signal from these thin ($4\mu$m) films proved to be a difficult task. In order to detect the small signal, we had to combat acoustical resonances in the NMR coil. We were able to separate the acoustical resonance signal from the NMR signal by averaging them with very short repetition rates. This procedure tends to supress the NMR signal, since the nuclear spin-lattice relaxation times are very long. Acoustical resonances were not a problem

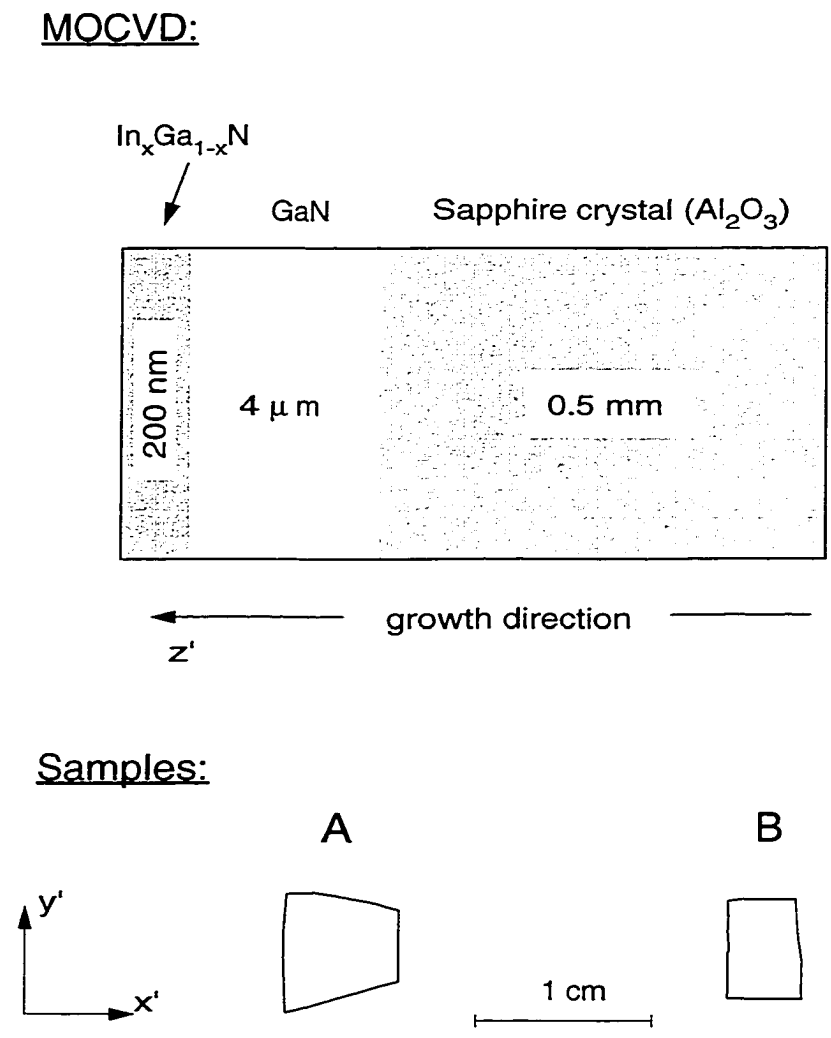


Figure 6.1: Schematic diagram of the MOCVD layer structure (top) and their planar dimensions (bottom).

while studying GaAs since the OPNMR signals there were relatively big. Fig. 6.2 shows the $^{69}$Ga and $^{71}$Ga central transitions ($m = -1/2 \rightarrow m = +1/2$) in sample B874 for two different temperatures. The lower temperature spectrum was extracted by averaging the free induction decay for 5 hours at T=1.5K. For this spectrum, the Mg doped sample was tilted by 54.5° from the crystalline c-axis in a 7 Tesla field. The $^{71}$Ga and $^{69}$Ga chemical shifts in these two samples are in good agreement with previously published values[105].

$^{69}$Ga is a spin 3/2 nucleus and possesses two satellite transitions in addition to the above central transition. Fig. 6.3 shows the upper $^{69}$Ga satellite transition ($m = -3/2 \rightarrow m = -1/2$) in sample B874 for different values of $\theta$. Note that the linewidth of the satellite transition at any angle is considerably larger than the linewidth of the central transition. For the perfect wurtzite crystal, we would expect this linewidth to be the same for both transitions, in sharp contrast to Figs. 6.2 and 6.3. Furthermore, the linewidth of the satellite transition increases dramatically as the angle is increased, and the satellite transition is no longer observable beyond $\theta$=12°.

In order to explain this phenomenon, let us consider the form of the quadrupolar interaction in the nucleus[43, 67]:

$$\mathcal{H}_{\mathrm{Q}} = \frac{eQ}{4I(2I-1)}\Big[V_{z'z'}(3I_{z'}^2 - I^2) + (V_{x'x'} - V_{y'y'})(I_{x'}^2 - I_{y'}^2)\Big]. \tag{6.1}$$

Here $\nabla_\alpha E_\beta = V_{\alpha\beta}$ is the electric field gradient (EFG) tensor present at the site of the nucleus and $x', y', z'$ are the principal axes of this tensor. The second term in the above expression exists only if $V_{\alpha\beta}$ is not axially symmetric, which is not the case in GaN. The total nuclear hamiltonian is then

$$\mathcal{H}_{\mathrm{n}} = -\gamma_n \hbar B_{\mathrm{tot}} I_z + \frac{eQV_{z'z'}}{4I(2I-1)}(3I_{z'}^2 - I^2)\ . \tag{6.2}$$

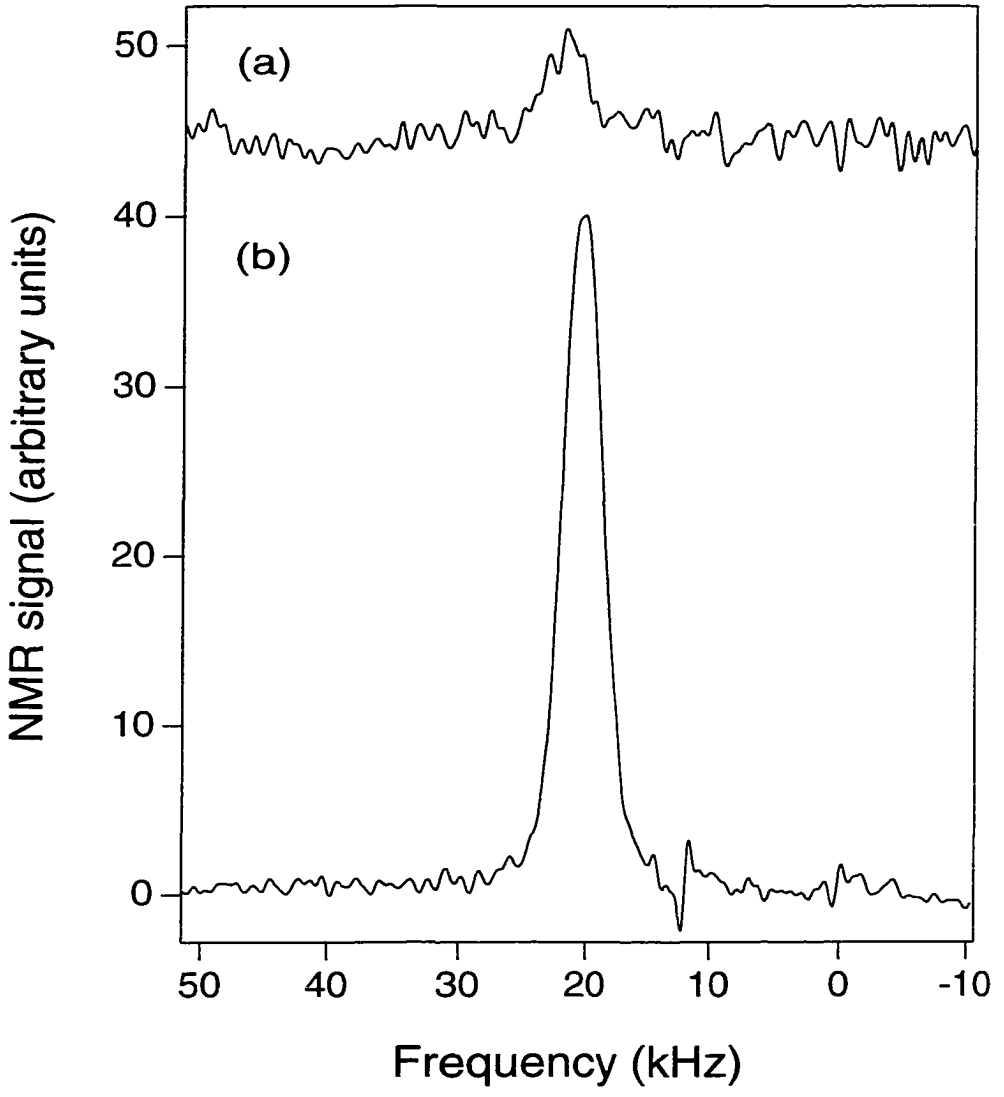


Figure 6.2: Shown for sample B874, the central transition at $B_{tot}$=7.03 T for (a) $^{71}$Ga at room temperature with $\theta$=53.2°, and $f_o$=91.34 MHz. (b) $^{69}$Ga at $T$=1.5 K with $\theta$=54.5°, and $f_o$=71.88 MHz.

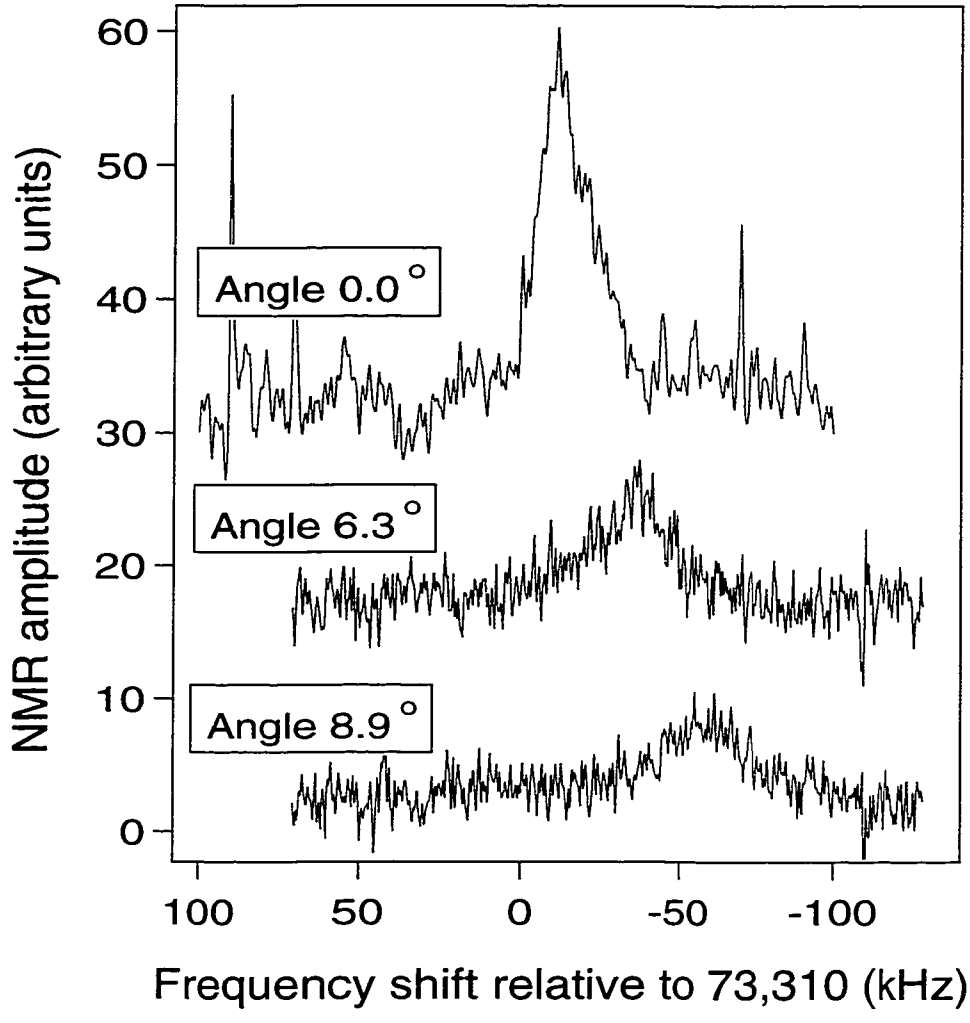


Figure 6.3: The upper $^{69}$Ga satellite transition ($m = -\frac{3}{2} \rightarrow -\frac{1}{2}$) for several different tilt angles $\theta$. Each spectrum was obtained by averaging for 5 hours at $T = 1.5$ K.

Without loss of generality, $I_{z'}$ can be substituted by $I_z\cos(\theta) + I_x\sin(\theta)$. Here, $\theta$ is also the angle between the sample growth axis and the magnetic field direction ($z$ axis). Note that for $\theta$=0, this hamiltonian can be solved exactly. The first order change in the energy is given by

$$E_m = E_m^{(0)} + E_m^{(1)} = -\gamma_n \hbar B_{\text{tot}} m +$$

$$\frac{eQV_{z'z'}}{4I(2I-1)}\left(\frac{3\cos^2\theta-1}{2}\right)\left[3m^2-I(I+1)\right]. \quad (6.3)$$

Variations in the frequency of the upper satellite transition due to "local" fluctuations in $V_{z'z'}$ and $\theta$ can explain the large satellite linewidth and it's dependence on the angle $\theta$. The frequency of the upper satellite transition is $f^{(1)}_{-3/2\rightarrow-1/2} \propto QV_{z'z'}(1-3\cos^2\theta)$. The large linewidth at $\theta = 0$ can then only be due to fluctuations in $V_{z'z'}$ {since the derivative of [1-3cos$^2$($\theta$)] with respect to $\theta$ is zero}. We deduce that $V_{z'z'}$ has a 1% FWHM gaussian distribution throughout the sample. The increase in the linewidth with increasing $\theta$ is due to a spread in the local values of $\theta$ or the $z'$ axis (symmetry axis of the EFG tensor). We find that this spread is as large as $\pm 2°$. This spread might be attributed to small angle tilts of grains, however, x-ray and TEM measurements indicate that such spreads should be 20 times smaller. Thus it appears likely that our observed variation in the local values of $\theta$ is due to something else... maybe local unit cell changes caused by internal electric fields.

An independent measurement of the spread in $\theta$ can be made by analyzing the linewidth of the $^{69}$Ga central transition. Fig. 6.4 shows that this linewidth varies dramatically as the angle $\theta$ is changed. This is in sharp contrast to the smooth behavior seen for the central and satellite $^{27}$Al transitions (Fig.6.4) in a perfect single crystal of Sapphire (in a perfect crystal, these two transitions will also have the same linewidths). In analogy to the above consideration for the satellites, we can explain the extra linewidth of the central transition by assuming a spread in the frequencies of the central transition (due to a variation in the local values of $\theta$).

For nuclei with half integer spin, the frequency of the central transition ($m = -1/2 \rightarrow m = +1/2$) is not shifted in first order. Using second order perturbation theory, this frequency is

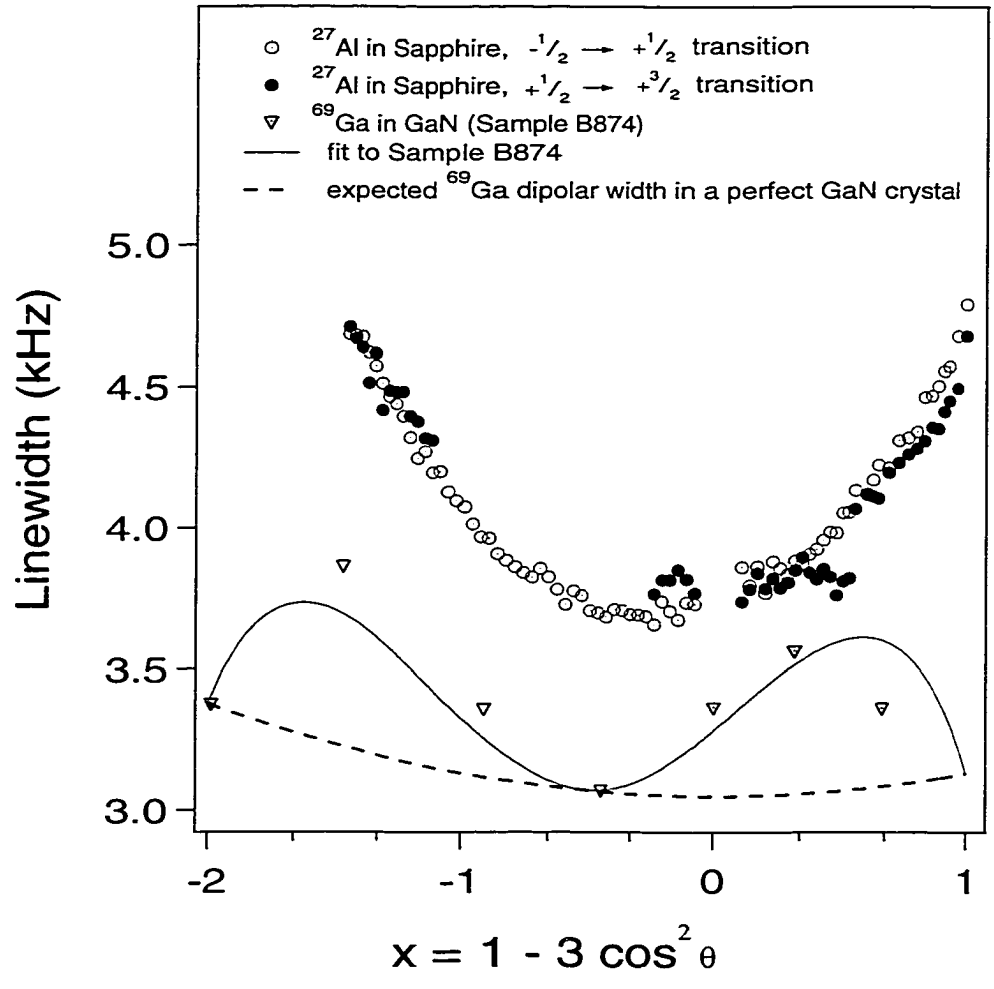


Figure 6.4: The linewidth for the $^{69}$Ga central transition (open triangles) is compared to the expected linewidth in a perfect GaN crystal (dashed line) and the $^{27}$Al linewidth for central and satellite transitions in sapphire (open and filled circles). The solid line represents a fit where the angular scatter in the local electric field gradients is $\pm 2°$.

$$f^{(2)}_{-1/2\to 1/2} = \frac{9}{256}\,\frac{2\pi e^2 Q^2 V^2_{z'z'}}{h^2 I^2(2I-1)^2\gamma_n B_{\rm tot}} \times\Big[4I(I+1)-3\Big]\Big[\Big(x+\frac{2}{3}\Big)^2-\Big(\frac{4}{3}\Big)^2\Big]\,. \tag{6.4}$$

The measured frequency of the $^{69}$Ga and $^{71}$Ga central transition in these thin films is shown in Fig. 6.5, and is in good agreement with the above expression. The observed variation in the linewidth of this transition with angle is consistent with our earlier value of a $\pm 2^\circ$ spread in the local direction of $V_{z'z'}$. It is remarkable that such a simple model (a gaussian spread in the distribution of $\theta$ and $V_{z'z'}$) can explain both of these phenomena so accurately. Fig. 6.5 can also be used to extract

$$\nu_{\rm Q} = \frac{3e\,Q V_{z'z'}}{2\,h\,I(2I-1)}\,, \tag{6.5}$$

which is the exact splitting between the different NMR transitions (central and satellite) at $\theta$=0. Our values of $\nu_{\rm Q}(^{71}Ga)$=890 kHz and $\nu_{\rm Q}(^{69}Ga)$=1400 kHz are in good agreement with published quadrupole splittings in GaN powder[105].

### 6.0.27 Nuclear Spin-Lattice Relaxation Time

The nuclear spin-lattice relaxation time in III-IV semiconductors is dominated by the interaction between the quadrupole moment of the nucleus and the crystalline lattice. The dominant mechanism for this effect is the Raman process where one quantum of lattice vibration is absorbed, another quantum is emitted and the nucleus can make either an $\Delta$m=$\pm$1 or $\pm$2 transition[106]. Measurements of the spin-lattice relaxation time for $^{69}$Ga and $^{71}$Ga are shown in Fig. 6.6. The ratio of the $^{69}$Ga and $^{71}$Ga relaxation time is in good agreement with the expected quadrupole moment ($\propto 1/Q^2$) scaling. The temperature dependence of the relaxation time in bulk GaN is expected

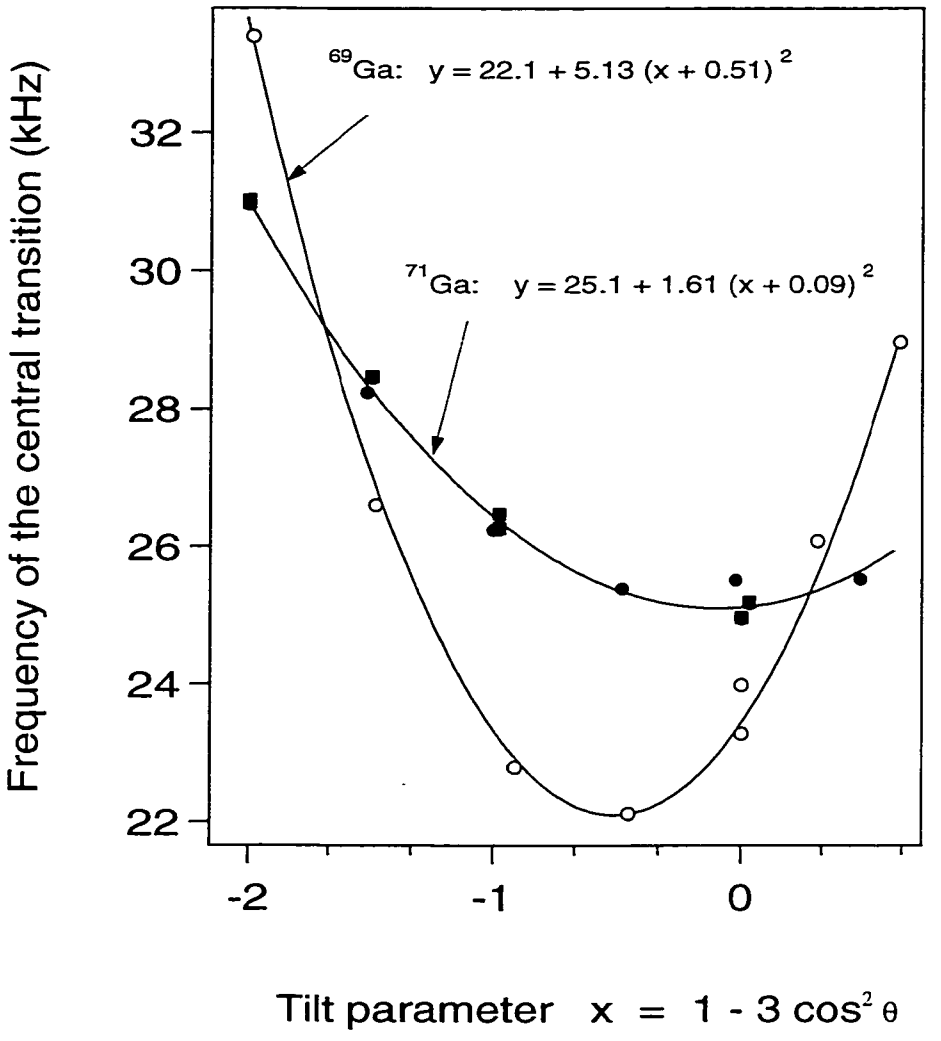


Figure 6.5: The frequency of the $^{71}$Ga and $^{69}$Ga central transition ($m = -\frac{1}{2} \rightarrow m = +\frac{1}{2}$) as a function of $x$. Solid lines are quadratic fits to the data.

to scale as $1/T^2$ at high $T$ and as $1/T^7$ at low $T$, where the Debye temperature ($\sim$ 100K) separates the high temperature regime from the low temperature regime. This seems inconsistent with the data shown in Fig. 6.6 for these thin films, which scale as $1/T^{4/3}$ (solid line) in the temperature range shown. The reason for this discrepency (which makes it much easier to make measurements at low $T$) is not yet understood.

In summary, NMR at the limit of conventional detection can still reveal valuable new information about the structural properties of epitaxial layers in GaN. However, due to the low sensitivity, one cannot use this technique to probe the properties of much smaller structures ($\sim$ 10nm, e.g. quantum wells). We can overcome this barrier by optical pumping. Based on our work in GaAs, we expect an amplification of the regular NMR signal by about 100. Further work in this direction is already underway.

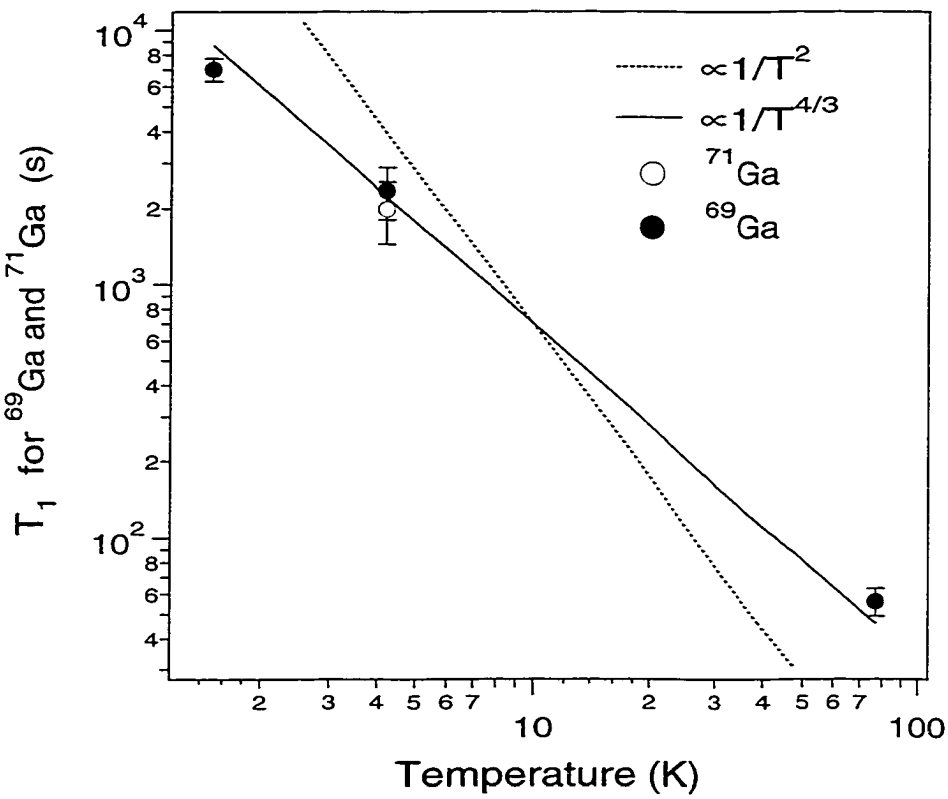


Figure 6.6: Nuclear spin-lattice relaxation time, $T_1$, for $^{69}$Ga and $^{71}$Ga in sample B874 for different temperatures, with $B$=7.03 T and $\theta$=54.5°.

# Chapter 7

# Conclusions

In summary, we have shown that optically pumped nuclear magnetic resonance (OP-NMR) can be an extremely useful tool to advance the understanding of spin physics in the quantum Hall regimes. At Yale, we have been able to push this technique down to lower temperatures ($T \sim 300\,\mathrm{mK}$) and upto higher magnetic fields ($B \sim 12\,\mathrm{T}$) than ever before. Data for the electron spin polarization $\mathcal{P}$ as a function of temperature and the Landau level filling factor $\nu$ around $\nu = 1/3$ in two different electron-doped multiple quantum well samples provide evidence that below $T \approx 500\,\mathrm{mK}$, the spin-reversed charged excitations of the $\nu = 1/3$ ground state become spatially localized over the NMR time scale of about 40 microseconds. We also found that the two-dimensional electron spin system at $\nu = 1/3$ could also be driven out of equilibrium by varying NMR pulse parameters. The establishment of an electron spin temperature that is different from the crystalline lattice temperature is an extremely unusual phenomenon. Observation of this effect implies that for $T < 500\,\mathrm{mK}$, the electron spin-lattice relaxation time $\tau_{1s}$ is between 100 microseconds and 500 milliseconds, at $\nu = 1/3$. We also report a preliminary attempt to use OPNMR as a probe of material properties in heterostructures made of GaN — a novel semiconductor with a band gap in the blue region of visible spectrum. Our first NMR measurements of the

quadrupole shift and the linewidth at $1.5\,\mathrm{K} < T < 300\,\mathrm{K}$ provide evidence that the local electric field gradients have an angular scatter of $\pm 2°$, exceeding the spread in the local crystalline lattice orientations by a factor of $\sim 20$.

# Bibliography


[1] K. von Klitzing, G. Dorda, and M. Pepper, Phys. Rev. Lett. **45**, 494 (1980).

[2] M. A. Paalanen, D. C. Tsui, and A. C. Gossard, Phys. Rev. B **25**, 5566 (1982).

[3] *The Quantum Hall Effect*, R. E. Prange and S. M. Girvin, Eds., Springer, N. Y., 2nd ed., 1990.

[4] T. Chakraborty and P. Pietiläinen, *The Quantum Hall Effects: Integral and Fractional*, Springer, Berlin, 2nd ed., 1990.

[5] For comprehensive reviews on $\nu$=1/2 and the FQHE, see: *Composite Fermions*, ed. by O. Heinonen (World Scientific, 1998); *Perspectives in Quantum Hall Effects*, ed. by S. Das Sarma and A. Pinczuk (Wiley, New York, 1997); J. K. Jain, Adv. Phys. **41**, 105 (1992); R. L. Willett, *ibid.* **46**, 447 (1997).

[6] The text of the 1998 Nobel Prize lecture: R. B. Laughlin, Revs. Mod. Phys. **71**, 863 (1999); H. L. Stormer, *ibid.* **71**, 875 (1999); D. C. Tsui, *ibid.* **71**, 891 (1999).

[7] A. H. MacDonald, *Quantum Hall Effect: A Perspective*, Kluwer Academic, Boston/Dordrecht.

[8] H. L. Stormer, Physica B **177**, 401 (1992); Phys. Scr. T **45**, 168 (1992).

[9] R. B. Laughlin, Phys. Rev. Lett. **50**, 1395 (1983).

[10] For recent theoretical developments, see: N. Read, Phys. Rev. B **58**, 16262 (1998); A. Stern, B. I. Halperin, F. v. Oppen, and S. H. Simon, *ibid.* **59**, 12547 (1999); R. Shankar, Phys. Rev. Lett. **83**, 2382 (1999).

[11] V. J. Goldman, B. Su, and J. K. Jain, Phys. Rev. Lett. **72**, 2065 (1994).

[12] V. J. Goldman and B. Su, Science **267**, 1010 (1995).

[13] A. Auerbach, Phys. Rev. Lett. **80**, 817 (1998).

[14] B. I. Halperin, P. A. Lee, and N. Read, Phys. Rev. B **47**, 7312 (1993).

[15] R. L. Willett, R. R. Ruel, K. W. West, and L. N. Pfeiffer, Phys. Rev. Lett. **71**, 3846 (1993).

[16] R. L. Willett, K. W. West, and L. N. Pfeiffer, Phys. Rev. Lett. **75**, 2988 (1995).

[17] W. Kang *et al.*, Phys. Rev. Lett. **71**, 3850 (1993).

[18] J. H. Smet *et al.*, Phys. Rev. Lett. **77**, 2272 (1996).

[19] B. I. Halperin, Helv. Phys. Acta **56**, 75 (1983).

[20] F. D. M. Haldane, and E. H. Rezayi, Phys. Rev. Lett. **54**, 237 (1985).

[21] R. Morf and B. I. Halperin, Phys. Rev. B **33**, 1133 (1986).

[22] S. E. Barrett *et al.*, Phys. Rev. Lett. **74**, 5112 (1995).

[23] A. Usher, R. J. Nicholas, J. J. Harris, and C. T. Foxon, Phys. Rev. B **41**, 1129 (1990).

[24] S. L. Sondhi, A. Karlhede, S. A. Kivelson, and E. H. Rezayi, Phys. Rev. B **47**, 16419 (1993).

[25] H. A. Fertig, L. Brey, R. Côté, and A. H. MacDonald, Phys. Rev. B **50**, 11018 (1994).

[26] M. Abolfath, J. J. Palacios, H. A. Fertig, S. M. Girvin, A. H. MacDonald, *Phys. Rev. B* **56**, 6795 (1997).

[27] H. A. Fertig et al., *Phys. Rev. B* **55**, 10671 (1997).

[28] K. Lejnell, A. Karlhede, S. L. Sondhi, *Phys. Rev. B* **59**, 10183 (1999).

[29] For a review, see the chapter by S. M. Girvin and A. H. MacDonald in *Perspectives in Quantum Hall Effects.*

[30] M. J. Manfra et al., *Phys. Rev. B* **54**, 17327 (1996).

[31] Y. Q. Song, B. M. Goodson, K. Maranowski, A. C. Gossard, *Phys. Rev. Lett.* **82**, 2768 (1999).

[32] A. Schmeller, J. P. Eisenstein, L. N. Pfeiffer, K. W. West, *Phys. Rev. Lett.* **75**, 4290 (1995).

[33] R. Tycko, S. E. Barrett, G. Dabbagh, L. N. Pfeiffer, K. W. West, *Science* **268**, 1460 (1995).

[34] V. Bayot, E. Grivei, S. Melinte, M. B. Santos, M. Shayegan, *Phys. Rev. Lett.* **76**, 4584 (1996); V. Bayot, E. Grivei, J.-M. Beuken, S. Melinte, M. Shayegan, *Phys. Rev. Lett.* **79**, 1718 (1997).

[35] D. K. Maude et al., *Phys. Rev. Lett.* **77**, 4604 (1996).

[36] S. Melinte, E. Grivei, V. Bayot, M. Shayegan, *Phys. Rev. Lett.* **82**, 2764 (1999).

[37] Y. A. Bychkov, S. V. Iordanskii, and G. M. Eliashberg, JETP Lett. **33**, 143 (1981).

[38] C. Kallin and B. I. Halperin, Phys. Rev. B **30**, 5655 (1984).

[39] D. C. Tsui, H. L. Stormer, A. C. Gossard, Phys. Rev. Lett. **48**, 1559 (1982).

[40] L. N. Pfeiffer *et al.*, Appl. Phys. Lett. **61**, 1211 (1992).

[41] D. R. Leadley *et al.*, Phys. Rev. Lett. **79**, 4246 (1997).

[42] L. N. Pfeiffer, private communication.

[43] C. P. Slichter, *Principles of Magnetic Resonance*, Springer, N. Y., 3rd ed., 1990.

[44] A. W. Overhauser, Phys. Rev. **91**, 476 (1953).

[45] T. R. Carver and C. P. Slichter, Phys. Rev. **92**, 212 (1953); *ibid.* **102**, 975 (1956).

[46] G. Lampel, Phys. Rev. Lett. **20**, 491 (1968).

[47] *Optical Orientation*, F. Meier and B. Zakharchenya, Eds., North-Holland, N. Y., 1984.

[48] R. Tycko and J. A. Reimer, J. Phys. Chem. **100**, 13240 (1996).

[49] S. E. Barrett, R. Tycko, L. N. Pfeiffer, and K. W. West, Phys. Rev. Lett. **72**, 1368 (1994).

[50] J. Winter, *Magnetic Resonance in Metals*, Oxford Univ. Press, London, 1971.

[51] W. D. Knight, Phys. Rev. **76**, 1259 (1949).

[52] C. Weisbuch and B. Vinter, *Quantum Semiconductor Structures*, (Academic Press, San Diego, 1991).

[53] G. Fishman, Phys. Rev. B **27**, 7611 (1983).

[54] T. S. Lay *et al.*, Phys. Rev. B **56**, 7092 (1997).

[55] P. Khandelwal, N. N. Kuzma, S. E. Barrett, L. N. Pfeiffer, and K. W. West, Phys. Rev. Lett. **81**, 673 (1998), preprint also available at cond-mat/9801199.

[56] N. N. Kuzma, P. Khandelwal, S. E. Barrett, L. N. Pfeiffer, and K. W. West, Science **281**, 686 (1998), preprint also available at cond-mat/9907279.

[57] D. Heiman, Chap. 1 in *The Spectroscopy of Semiconductors*, D. G. Seiler and C. L. Littler, Eds., Academic Press, San Diego, 1992.

[58] L. B. Loeb, *Fundamental Processes of Electrical Discharge in Gases*, Wiley, N. Y., 1939.

[59] R. C. Richardson and E. N. Smith, *Experimental Techniques in Condensed Matter Physics at Low Temperatures*, Addison-Wesley, Reading (Massachusetts), 1988.

[60] E. Fukushima and S. B. W. Roeder, *Experimental Pulse NMR: A Nuts and Bolts Approach*, Addison-Wesley, Reading (Massachusetts), 1981.

[61] K. Moon *et al.*, Phys. Rev. B **51**, 5138 (1995).

[62] M. J. Manfra *et al.*, Phys. Rev. B **54**, R 17 327 (1996).

[63] T. Chakraborty and P. Pietiläinen, Phys. Rev. Lett. **76**, 4018 (1996).

[64] N. Read and S. Sachdev, Phys. Rev. Lett. **75**, 3509 (1995).

[65] M. Kasner and A. H. MacDonald, Phys. Rev. Lett. **76**, 3204 (1996).

[66] R. Haussmann, Phys. Rev. B **56**, 9684 (1997); C. Timm, P. Henelius, A. W. Sandvik, and S. M. Girvin, cond-mat/9710220.

[67] A. Abragam, *Principles of Nuclear Magnetism*, Oxford Univ. Press, N. Y., 1961.

[68] J. I. Kaplan and G. Fraenkel, *NMR of Chemically Exchanging Systems*, Academic Press, N. Y., 1980.

[69] M. Mehring, *Principles of High Resolution NMR in Solids*, Springer-Verlag, Berlin, 2nd ed., 1983.

[70] R. L. Willett (private communication).

[71] R. K. Kamilla, X. G. Wu, and J. K. Jain, Solid State Commun. **99**, 283 (1996).

[72] K. H. Ahn and K. J. Chang, Phys. Rev. B **55**, 6735 (1997).

[73] R. J. Haug *et al.*, Phys. Rev. B **36**, 4528 (1987).

[74] J. Kikkawa and D. Awschalom, Phys. Rev. Lett. **80**, 4313 (1998).

[75] D. M. Frenkel, Phys. Rev. B **43**, 14228 (1991).

[76] In this limit, $\mathcal{P}(\nu) = 1 - 2(K+1)(1-\frac{1}{\nu})$ for $\nu \geq 1$ and $\mathcal{P}(\nu) = 1 - 2K(\frac{1}{\nu}-1)$ for $\nu \leq 1$. Experimentally, $K=2.6\pm0.3$[22].

[77] E. H. Aifer, B. B. Goldberg, and D. A. Broido, Phys. Rev. Lett. **76**, 680 (1996).

[78] A. J. Nederveen and Yu. V. Nazarov, *Phys. Rev. Lett.* **82**, 406 (1999).

[79] H. A. Fertig, Private communication.

[80] H. Fukuyama and P. A. Lee, *Phys. Rev. B* **17**, 535 (1978).

[81] M. C. Cha and H. A. Fertig, *Phys. Rev. Lett.* **73**, 870 (1994).

[82] A. I. Larkin and Yu. N. Ovchinnikov, *J. Low Temp. Phys.* **34**, 409 (1979).

[83] J. H. Ross Jr., Z. Wang, C. P. Slichter, *Phys. Rev. Lett.* **56**, 663 (1986).

[84] W. H. Wong, M. E. Hanson, B. Alavi, W. G. Clark, *Phys. Rev. Lett.* **70**, 1882 (1993).

[85] E. G. Nikolaev, J. Witteveen, M. de Kok, H. B. Brom, *Phys. Rev. B* **55**, 8717 (1997).

[86] J. Sinova, S. M. Girvin, T. Jungwirth, and K. Moon, preprint cond-mat/9908029.

[87] Details will be published elsewhere.

[88] In this picture, the earlier data at $\nu$=1/3[56] are in the $\Delta U/U \rightarrow 0$ limit.

[89] R. R. Du *et al.*, Phys. Rev. Lett. **75**, 3926 (1995).

[90] I. V. Kukushkin, K. v. Klitzing, and K. Eberl, Phys. Rev. Lett. **82**, 3665 (1999).

[91] K. Park and J. K. Jain, Phys. Rev. Lett. **80**, 4237 (1998).

[92] A. E. Dementyev, N. N. Kuzma, P. Khandelwal, S. E. Barrett, L. N. Pfeiffer, and K. W. West, submitted to Phys. Rev. Lett.; preprint also available at cond-mat/9907280.

[93] F. C. Zhang and S. Das Sarma, Phys. Rev. B **33**, 2903 (1986).

[94] R. Shankar, cond-mat/9911288.

[95] S. Taniguchi *et al.*, Electron. Lett. **32**, 552 (1996).

[96] S. Nakamura *et al.*, Appl. Phys. Lett. **70**, 1417 (1997).

[97] H. Amano, M. Kito, K. Hiramatsu, and I. Akasaki, Jpn. J. Apl. Phys. **28**, L2112 (1989).

[98] S. Nakamura, T. Mukai, M. Senoh, and N. Iwasa, Jpn. J. Apl. Phys. **31**, L139 (1992).

[99] F. Ponce and D. Bour, Nature **386**, 351 (1997).

[100] S. Strite and H. Morkoc, J. Vac. Sci. Technol. B **10**, 1237 (1992).

[101] S. D. Lester, F. A. Ponce, M. G. Craford, and D. A. Steigerwald, Appl. Phys. Lett. **66**, 1249 (1995).

[102] V. Fiorentini, F. Bernardini, F. Della Sala, A. Di Carlo, and P. Lugli, Phys. Rev. B **60**, 8849 (1999), preprint also available at cond-mat/9905186.

[103] For recent examples of experimental developments in this area, see: F. K. Koschnick *et al.*, Phys. Rev. B **54**, R11042 (1996); G. Denninger and D. Reiser, *ibid.* **55**, 5073 (1997); E. R. Glaser *et al.*, *ibid.* **57**, 8957 (1998).

[104] R. Tycko, G. Dabbagh, S. R. Kurtz, and J. P. Goral, Phys. Rev. B **45**, 13452 (1992).

[105] O. H. Han, H. K. C. Timken, and E. Oldfield, J. Chem. Phys. **89**, 6046 (1988).

[106] R. L. Meiher, Phys. Rev. **125**, 1537 (1962).